Design of a Torsion Measurement System of High Stiffness and Sensitivity to Study Yield in Low Carbon Steels.

Alison S Tuling

A dissertation submitted to the Faculty of Engineering, University of the Witwatersrand, Johannesburg, in fulfilment of the requirements for the degree of Master of Science in Engineering.

Johannesburg, August 2006

Declaration

I declare that this dissertation is my own, unaided work, except where otherwise acknowledged. It is being submitted for the degree of Master of Science in Engineering in the University of the Witwatersrand, Johannesburg. It has not been submitted before for any degree or examination in any other university.

Signed this ___ day of _____ 20___

_____

Alison S Tuling.

Abstract

Strain ageing anisotropy, a surprising property of iron, implies that interstitials, which are non-lattice obstacles, can give non-symmetrical opposition to glide. Although this has been investigated by others, it is shown that it is difficult to eliminate extraneous residual stresses during testing. An Avery torsion machine was adapted for the study of strain ageing anisotropy through the design of a torque and twist measurement system. This required the optimization of sensitivity, stiffness and mechanical stability criteria, while ensuring practicality. When a fine-grained sample with circumferential groove was tested a sharp yield point and lack of yield after ageing in the reverse direction was observed. Although more testing is required, it confirms the results of other researchers. In testing it was found that the quality of the sample machining was critical in achieving an accurate yield, and the groove design must be reviewed and improved. While the system measured to the required torque resolution, the strain measurement system could be improved by redesign and better calibration statistics.

Acknowledgements

The author would like to thank Fabrizio Dionisio, Peter Bidgood of the CSIR and Chris Pistorius of University of Pretoria for their unreserved good will - including equipment. Thanks to my supervisors, Professor Nabarro and Professor Cornish for their advice and direction and to Iscor for funding the project in part. Professor Jean-Luc Martin and Genie Atomiqué, EPFL kindly financed an opportunity to study in Lausanne Switzerland, and this was greatly appreciated. Lastly to my husband, Sean, for his patience and support to the very end.

Contents

List of Figures

List of Tables

List of Symbols

τ_{RSS}	Resolved shear stress on a crystal plane
P	Applied force
α	Angle between the slip plane normal and the applied force, P
β	Minimum angle between the slip plane and the applied force, P
δ	Angle between the slip direction and the applied force, P
σ_{ys}	Yield strength of a polycrystalline sample
σ_i	Overall resistance of lattice to dislocation movement
k_y	'Locking parameter' that measures the relative hardening contribution of the grain boundaries
d	Grain diameter
σ_0	Critical tensile stress
A'	Parameter of elastic constants ($3\text{x}10^{15} N.cm^{-2}$)
λ	Slip distance of the dislocation
ρ	Equilibrium distance that a line of solute atoms lies away from the dislocation
v	Drift velocity of a carbon atom
D	Diffusion coefficient of carbon in iron

κ	Boltzmann constant ($1.38 \times 10^{-23} J/K$)
U	Binding energy of a solute atom to a dislocation
r_c	The distance of a solute atom from the edge dislocation core
α_c	The angle co-ordinate of a solute atom with respect to an edge dislocation
σ_{uy}	Upper yield point
$\sigma_{0(u)}$	Friction stress if all grains are deforming
$\Delta\sigma_0$	Change in friction stress produced by a ten-fold increase in the strain rate
N_i	Number of grains per unit volume actually deforming at σ_{uy}
$kd^{-\frac{1}{2}}$	Resistance to the spread of a slip band associated with the presence of grain boundaries
Θ	Projected angle of a Burgers vector on a reflecting plane
$\mathbf{b}$	Burgers vector of a dislocation
$\mathbf{g}$	Reflecting plane
$\mathbf{z}$	Zone axis
R_{outer}	Sample outer radius
t_{sample}	Sample thickness
τ_{act}	Actual shear stress developed in a thin-walled tube
τ_{approx}	Approximate shear stress developed in a thin-walled tube using a thin-walled approximation
K_{rR}	Stress concentration factor for a shoulder fillet radius
r_{fillet}	Shoulder fillet radius

K_{ts}	Stress concentration factor for a groove in a bar in torsion
d_{groove}	Groove depth
r_{groove}	Groove radius
L	Sample length
S_y	Yield stress
τ_y	Torsional yield stress
T_y	Torque at yield
I_p	Polar moment of inertia
T	Torque
τ	Torsional shear stress
G	Shear modulus
ϕ	Torsional twist
Sensitivity	The number of measurable units of output (Signal) per unit torque (T)
V_{out}	Measured voltage across a Wheatstone bridge
$V_{excitation}$	Excitation voltage as applied to the strain gauge
k	Strain-gauge factor
ϵ	Surface strain
γ	Torsional strain
r_i	Inner radius of torque tube
r_o	Outer radius of torque tube
r	Mean radius of torque tube

t	Thickness of torque tube
f_{approx}	Fractional inaccuracy of the thin-walled approximation
$I_{p\ actual}$	Actual polar moment of inertia
$I_{p\ thin}$	Polar moment using the thin-wall cylinder approximation
V_{gauge}	Voltage across one gauge in a Wheatstone bridge
P_{gauge}	Power dissipated in each strain gauge
R	Electrical resistance
P'	Power dissipated per unit area
A_{gauge}	Strain gauge area
V_{noise}	The Johnson noise in an electrical system
T	Absolute temperature
Δf	Band width (Hz)
ϕ_{system}	Total twist in torsion system
$\phi_{machine}$	Elastic twist of machine
$\phi_{elastic}$	Elastic twist of sample
$\phi_{plastic}$	Plastic twist of sample
$K_{machine}$	Spring constant of torsion machine
Stiffness	Torsional stiffness of torque tube
l	Length of torque tube
T_{max}	Maximum torque that a tube can withstand
$T_{\substack{crit,\\short}}$	Critical torque for short-tube buckling

E	Young's modulus
ν	Poisson's ratio
s	Safety factor
R_{inner}	Sample inner radius
ϵ_f	Critical surface strain for fatigue limit
t_m	Minimum thickness for machining
l_{gauge}	Length of a strain gauge
$D_{sample\ grip\ end}$	Torque tube diameter on the sample grip end
$D_{jaw\ grip}$	Torque tube diameter at jaw grip end
$l_{sample\ grip\ end}$	Length of the tube at the sample grip end
$d_{torque\ tube}$	Torque tube diameter
SEE	Standard error of estimate for a linear or polynomial regression
N	Number of points
y_i	y values of points 1...N
x_i	x values of points 1...N
a_0	Constant in polynomial regression
a_1	x coefficient in polynomial regression
a_2	x^2 coefficient in polynomial regression
a_3	x^3 coefficient in polynomial regression
θ_{cal}	Angle at which the calibration bar is inclined
L_{cal}	Length of the calibration bar

M	Mass of the weight pans and weights
g	Acceleration due to gravity
$\dot{\gamma}$	Torsional strain rate
$\tau_{y\ forward}$	Torsional shear stress in the forward direction
$\tau_{y\ reverse}$	Torsional shear stress in the reverse direction
$\Delta\tau_y$	The difference between the lower yield stress (or 0.1% proof stress) after ageing and the flow stress observed at the end of first (forward)straining
$\overline{d}$	Average grain size
L_i	Line length in the line intercept method
N_{gb}	Number of grain boundaries crossed by line L_i in the line intercept method
dR/R	Fractional change in resistance of a strain gauge
dL/L	Fractional change in length of a strain gauge
π_i	Longitudinal piezoresistance coefficient
$\frac{\Delta R}{R}$	The ratio of the change in resistance to the original resistance in a strain gauge
SNR	Signal to noise ratio
V_s	Signal voltage
V_n	Noise voltage
$V_{rms\ noise}$	Voltage from thermal noise
P'_{packed}	Heat dissipation of packed gauges
$P'_{isolated}$	Heat dissipation of isolated gauges

$R_{\text{effective}}$	Effective gauge radius, the average distance that close-packed gauges are to each other
S_0	Sensitivity limit
Σ_0	Stiffness limit
$F(x, y, z)$	function in x, y, z
m	slope in the equation for non-concentricity of bore in samples
c	constant in the equation for non-concentricity of bore in samples
S_x	Sample standard deviation
X_k	The outlier in the sample when testing for Chauvenet's Criterion
$\overline{X}$	Sample average
ζ	Chauvenet's Criterion
$A_0 - A_5$	Constants in Chauvenet's Criterion
$\infty - 1$	Number of symbols used
$Stiffness_{machine}$	Avery machine stiffness
$\phi_{measured}$	Measured twist
ϕ_{sample}	Sample twist
$G_{expected}$	Expected shear modulus of steel
$G_{measured}$	Measured modulus

Chapter 1

Introduction

Steel has been cast, hammered, formed and studied for centuries. Yet, still, it has not completely yielded up its secrets. Many of the tools of studying these secrets have only been developed in the last 100 years. Correspondingly, all of materials science, including the study of the fundamentals of steel, has made great leaps in the 21st century.

This study began as the investigation of one of those unexplained characteristics. Initially, the aim of this study was to investigate reversal strain ageing anisotropy in iron. Strain ageing anisotropy is the lack of a yield point on reverse straining after normal ageing times. After some preliminary work by the author, in Lausanne, Switzerland, it was seen that specialized equipment was required for the investigation. Thus the scope of the topic metamorphosed into the development of the equipment for studying the strain ageing anisotropy in iron. Testing of the system showed that some criteria were more critical than predicted; thus improved criteria were developed. This dissertation therefore consists of:

- A literature survey of the strain ageing anisotropy in iron (Chapter 2).
- The experimental section, divided into three distinct chapters, consisting of
  - the details of the preliminary experiments that showed the need for specialized equipment (Chapter 3);
  - the design and optimisation of the equipment, (Chapter 4). There were many designs; all but the final design were relegated to the Appendix B;
  - the testing of the equipment/system which involved the calibration and

the preliminary sample testing (Chapter 5), with the details of the calibration in Appendix C.

- The analysis of the results (Chapter 6), with the details of the analysis in Appendix D.
- A discussion of the results (Chapter 7).
- Improved design criteria (Chapter 8) and, finally,
- The conclusion of the experiment and recommendations (Chapters 9 and 10).

There was also a brief foray into modelling the Schmid factor in iron, and this is documented for completeness in Appendix A.

When anisotropy is described in this dissertation, lattice anisotropy is being referred to rather than macro-anisotropy associated with texturing. Lattice anisotropy describes the property variation with the direction of the stress (forward or reverse) on a crystal, while texture occurs where the individual crystals in a polycrystalline material are not randomly orientated but are rather orientated in some dominant direction, resulting in a variation in properties on a macroscale.

1.1 A brief overview of steel anisotropy

The anisotropy of steel has been an ongoing debate, at times heated but mostly a murmur. Anisotropy has been shown to have many causes, and there are almost as many theories. The focus of this survey is only one form of directionality, combined with the phenomenon of strain ageing.

When a low-carbon rimming steel is deformed plastically and then aged before continuing to strain in the same direction, a short ageing treatment is sufficient to restore a sharp yield point. This is convincingly explained by Cottrell and Bilby's theory of the pinning of dislocations by solute carbon [1] (refer to Section 2.2.5 for other effects).

One of the first researchers who showed the anisotropy of strain ageing was Tipper (née Elam) [2]. If the direction of the re-straining is different from that of the first strain, she found that the sharp yield point returned very slowly, if at all.

Elliot, Orowan and Udoguchi [3], using a torsional testing system, showed that reversal without ageing in the yield range lead to the usual smooth reduction in flow stress (Bauschinger effect). However, after ageing, where one expects the dislocations to relock, no yield point was seen. To prevent the formation of axial Lüders bands and their effect on residual stresses, they performed the experiments on grooved samples. However, they used a steel containing pearlite, which is likely to induce residual stresses on deformation.

Wilson and Ogram [4] also performed similar experiments, although they used a lower carbon steel and they did not use grooved samples. They proposed that straining a specimen in tension results in most of the mobile dislocations being pressed against obstacles such as grain boundaries, precipitate particles and dislocation tangles. When re-straining is in the same direction the dislocations continue to face the same obstacles. It would therefore be necessary to lock only a few isolated dislocations to produce a return of the sharp yield point. In contrast, if the specimen is re-strained in any direction other than the original one, most dislocations will be free to move appreciable distances, since the applied stress will then be tending to move them away from the obstacles that were blocking them. Thus even if isolated dislocations become locked before dislocations in the tangles or pile-ups (especially at low solute contents where there is not a high enough local concentration of interstitials to pin all the available sites in a tangle), then unpinned dislocations in the tangles would be free enough to prevent the appearance of a yield point in reverse straining [4].

In both Elliot *et al.'s* work and Wilson and Ogram's work the absence of internal stresses, during testing, is debatable (refer to Section 2.3). Therefore it is necessary to perform new experiments. Since careful measurement of the upper and lower torsion yield is required in these experiments, accurate equipment is required. It was hoped that more information might come from experiments with higher sensitivity. Thus the aim was to do a "best possible" experiment, which must be designed and built, as none was available in the province of Gauteng.

1.2 The need for this research

Strain ageing is of commercial importance in a number of ways. It may lead to an undesirable decrease in ductility in cold forming operations, or give rise to unsightly

stretcher-strain markings in pressing operations [5]. However, the strengthening effects can, in some cases, be used to advantage, such as for car body panels where a super-formable steel can be made more dent-resistant by utilizing the strain ageing effect that can occur during paint baking (bake-hardening steel). The precipitation of carbides (which occurs at advanced stages of quench ageing) is also used in this application.

Williams has reported the anisotropy of strain ageing in HSLA (high strength low alloy) line pipe steel [6]. In the fabrication of thick (>15mm) walled pipe from plate, reverse straining is unavoidable and thus behaviour in reverse straining is of significance. It would be highly desirable for the steel to regain the high yield strengths that occur before fabrication (spiral welding). Some sort of ageing (especially if it could occur during the post-weld stress-relieving treatment) would be highly desirable, although for line pipe material impact behaviour is of major importance and strain ageing generally leads to poor fracture toughness.

Wilson and Ogram [4] point out that directionality of strain ageing is put to use in temper rolling where the return of yield is retarded, but also limits the application of strain ageing as an effective strengthening mechanism. The most important type of pre-strain is an elongation of about 1-1.5% by temper rolling, since this process can be used to suppress the sharp yield point in sheet steel for pressing, but is more commonly used on non-strain ageing aluminium killed steel to increase surface roughness to enhance adhesion of coatings.

Both the work of Wilson and Ogram [4], and that of Elliot, Orowan and Udoguchi [3], have their shortcomings, especially in regard to the build up of unwanted residual stresses in the material due to the presence of second phases such cementite, pearlite, MnS and nitrides (this is discussed further in Section 2.3.1 and 2.3.2).

In order to avoid these problems, equipment must be built that can measure the yield point effects and a steel that has an extremely low volume fraction of carbides must be used for the sample material. It is hoped that in a further study the dislocation movement before and during yield can be investigated.

Chapter 2

Literature survey

2.1 Problem statement: strain ageing anisotropy

A yield point is generally present in a steel containing interstitial carbon and or nitrogen. Experiments done by Elliot, Orowan and Udoguchi [3] (Figure 2.1) and also Wilson and Ogram [4] (Figure 2.2) show that if the direction of straining after ageing is reversed then discontinuous yield is not always present. It appears that interstitials, which are non-lattice obstacles, give non-symmetrical opposition to glide.

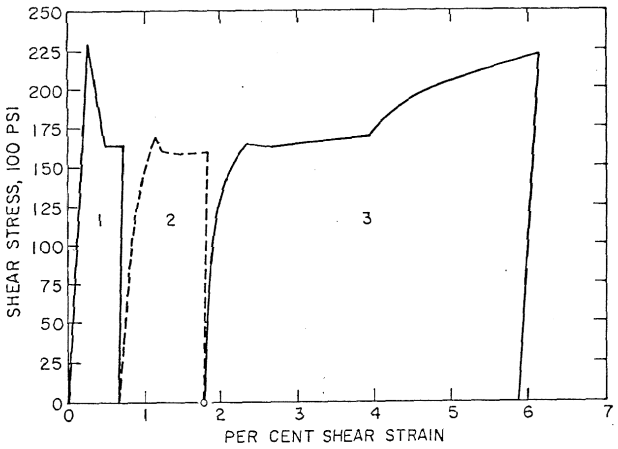

Figure 2.1: Torsion test. First straining (1). Reversal without ageing in the yield range (2): Bauschinger overshoot. After reversal, ageing followed by another reversal,(3), aluminium killed steel [3].

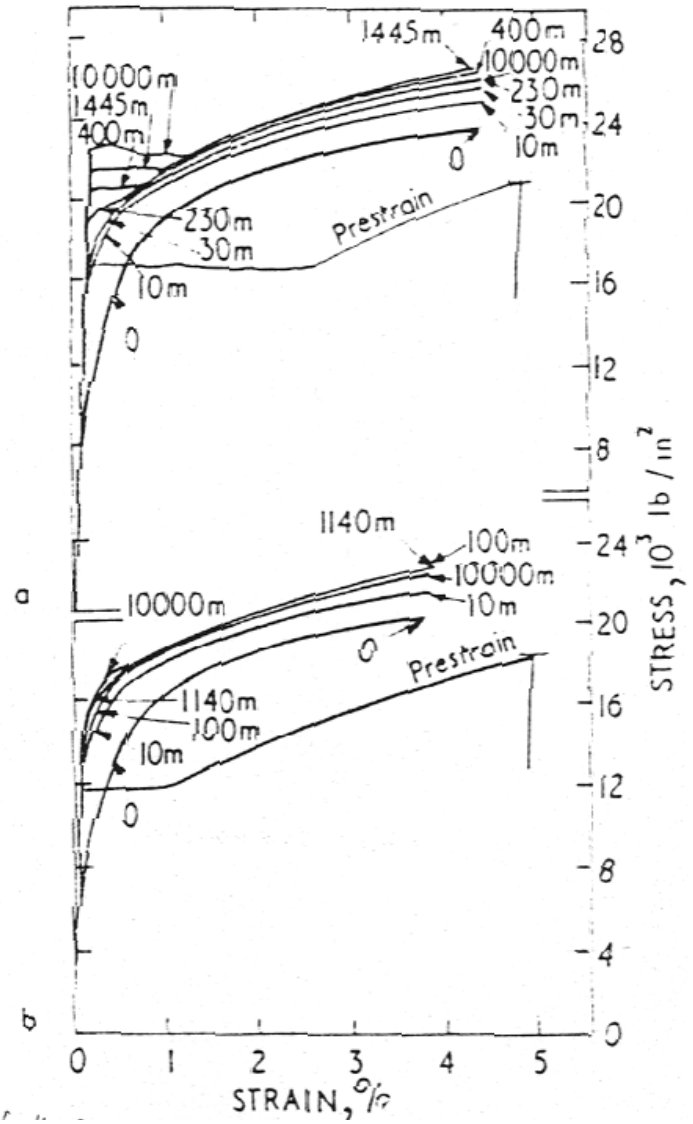

Figure 2.2: Effect of ageing (time in minutes (m)) at 89°C on torsional stress strain curves for steel, slowly cooled to 200°C before pre-straining [4]. Tested in reverse re-straining. Grain size in a) 1920 grains/mm^2, b)130 grains/mm^2. No groove. In a) the yield point returns after 230 minutes, while in b) the yield point returns after 1140 minutes.

2.2 Related phenomena

First the ground work must be laid for exploring strain ageing anisotropy. This needs a look at dislocation motion, work hardening and reverse motion of dislocations and strain ageing.

2.2.1 Dislocations in ferrite

Strain ageing anisotropy in steel is primarily the immobilization and mobilization of dislocations in ferrite. Stress will affect the behaviour and movement of dislocations, while grain boundaries, dislocation cell structure, second phase particles will interfere with their movement. There is merit therefore, in discussing dislocations in iron.

Slip

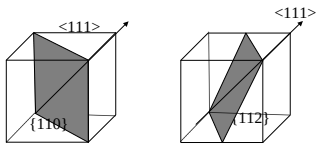

Figure 2.3: The two main slip systems in bcc.

The Peierls-Nabarro stress dictates that slip will occur predominantly on the planes of maximum atomic density. The slip occurs in the close packed direction (the shortest distance between two equilibrium atom positions) to minimize the energy requirement. In fcc this is the {111} plane, however, in bcc there are no fully dense planes. The {110} plane is the most densely packed plane and slip will first occur on the {110} plane in the most dense direction, $\langle 111 \rangle$, and then on the {112} plane in the $\langle 111 \rangle$ direction and as illustrated in Figure 2.3. A further slip plane is {123} [7].

For a certain tensile axis the dislocations on the $\langle 111 \rangle$ and the slip plane {110} or {112} with the greatest resolved shear stress will move first [7]. This stress is, in theory, determined by the Schmid factor.

Schmid factor

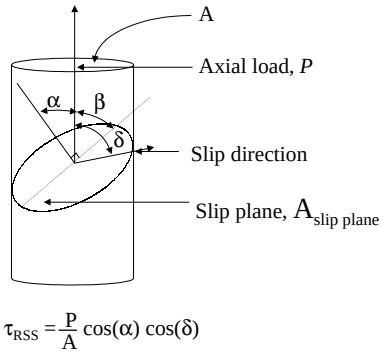

Figure 2.4: Orientation of slip plane and slip direction relative to the loading axis.

Plastic deformation in single crystals takes place when the resolved shear stress (τ_{RSS}) acting on the slip plane in the slip direction reaches a critical value (Figure 2.4).

The term $\cos\phi\cos\lambda$ is known as the Schmid factor and slip systems that are oriented such as to have the highest Schmid factor will yield first [7].

A brief foray into modelling the slip systems in bcc crystals with ideal Schmid behaviour was done by this author, and this is documented and discussed for completeness in Appendix A, page 141. The Schmid behaviour of bcc crystals was successfully simulated. This was confirmed by comparing the same simulation on fcc crystals to published fcc behaviour.

The motion of dislocations at yielding is, in reality, far more complicated.

Bcc metals can exhibit two primary non-Schmid phenomena. The first effect is the twinning-anti-twinning slip asymmetry, which is an intrinsic property of the lattice. The resistance to plastic flow on some slip planes varies with the directional sense. The asymmetry is such that the critical resolved shear stress (CRSS) is lower when the maximum resolved shear stress (MRSS) plane is closer to a {211} plane sheared in the twinning sense than to a {211} plane sheared in the anti-twinning sense. The magnitude of the asymmetry depends on the bcc metal [8].

Suzuki[9] demonstrates this theoretically at low temperatures by taking the simplest dislocation motion case at low temperatures. At these temperatures the geometry

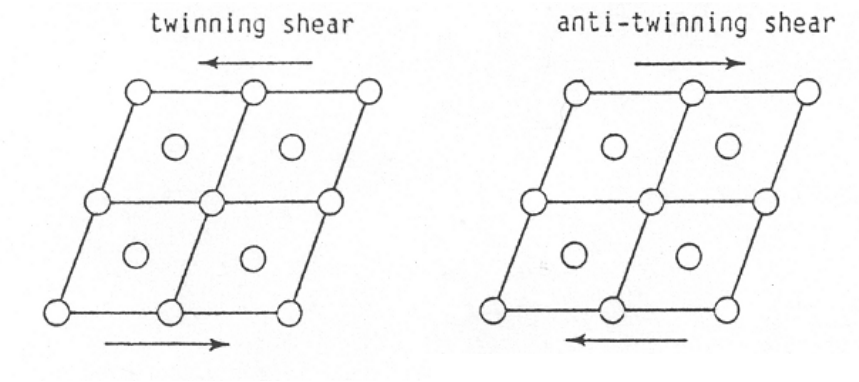

Figure 2.5: Non-equivalence of opposite senses of $\{112\}\langle 111\rangle$ shear in the bcc lattice at low temperatures [9, page 85].

of the dislocation in the bcc lattice affects its movement, as in Figure 2.5 [9]. Extrapolation to higher temperatures and the inclusion of the effects in polycrystalline material would be required to apply this to the problem of strain ageing anisotropy at room temperature.

A second non-Schmid feature is the effect of non-glide shear stresses. Suitable shear components of the applied stress tensor can affect the core structure by the interaction with edge components of the fractional dislocations forming the core of $\frac{a}{2}\langle 111\rangle$ screw dislocations in a bcc lattice. This effect may be strong in some bcc metals and weak or absent in others [8]. Unfortunately, the importance of the effect in iron was not mentioned. If these effects could be quantified in iron in a mathematical way then these could be simulated along the lines of the Schmid factor simulation in Appendix A.

Pencil glide

Iron is known to experience pencil glide (Figure 2.6), which is defined as the slip on the most highly stressed plane, not necessarily of highest density, which contains $\langle 111\rangle$. These descriptions of dislocations only applies to sparse dislocations, as soon as there are enough dislocations for interaction, the picture becomes more complicated, since work hardening starts to occur.

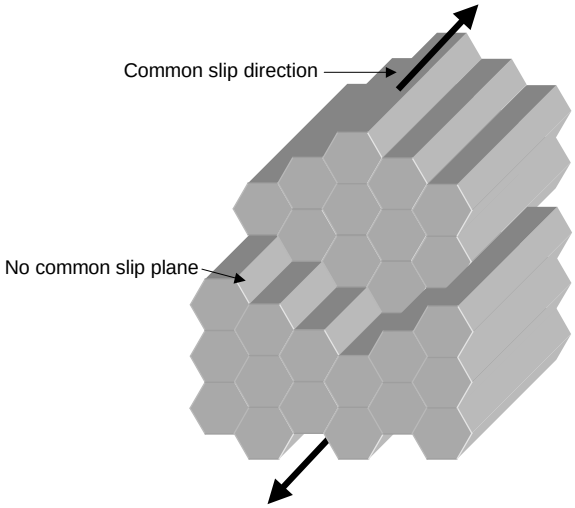

Figure 2.6: Pencil glide.

Work hardening

During plastic flow in iron, dislocations appear to be generated from grain boundaries, existing dislocations or other interfaces; they form clusters and tangles within the grain at very early stages of deformation. This occurs even in the Lüders band region if the deformation is slow or at normal and elevated temperatures [10]. The strain at the Lüders front is equivalent to the total Lüders strain and can be as large as 3% [3]. Thus, work hardening must be considered.

Most of the studies on work hardening have been done on the work hardening characteristics of fcc crystals [11]-[16]. However, very little has been reported on work hardening in steel (with interstitial carbon), iron. Li[10] has made the most significant contribution to the topic of work hardening in iron and thus his work is referred to throughout the literature survey of this dissertation. Unfortunately, no work hardening model discusses the effect of interstitial impurities, so that this effect is discussed from the conventional perspective in Section 2.2.3, page 20.

Work hardening of fcc single crystals shows three distinct stages. Stage one consists of easy glide, where a heterogenous distribution of low density dislocations exists on the primary slip plane and in a single slip system. The stage one dislocation structure (in fcc single crystal) consists mainly of isolated pairs of edge dislocations on the primary slip plane [11]. Stage two is a phase of rapid strain hardening with slip on multiple slip systems where dislocations, both screw and edge, entangle on

intersecting slip planes. Finally, stage three is frequently explained as parabolic hardening; here the rate of work hardening falls by a factor of 50% as hardening is now only from edge dislocations as screw dislocations are no longer blocked and can surmount obstacles by cross slip (which occurs more readily in high stacking fault energy materials). The last stage usually resembles the stress strain curve seen in the polycrystalline form of the material [7].

This applies to the fcc structure and not necessarily to bcc where the slip would not occur on a uniquely defined slip plane, thus in work hardening of bcc single crystals stage one is absent. Iron tends to experience multiple slip: pencil glide is often observed [17] where the slip surface has a common slip direction but many slip planes (Figure 2.6). Slip bands (common slip direction and slip plane) are less likely and no pileups occur. Tangles can occur when dislocations occur on multiple slip planes ($\{110\}$,$\{112\}$,$\{113\}$), with a common slip direction ($\langle 111 \rangle$)[10].

It has been suggested that Frank-Read sources generate dislocations, and these come against obstacles resulting in pile-ups. However, pile-ups are rarely seen in iron [18], [19], presumably as a result of multiple slip starting early in the hardening process, so that tangles are seen instead.

In fcc crystals it is believed that work hardening occurs when dislocations are created and move to form a heterogenous structure. This is because the dislocations must adjust themselves to reduce the long range stress fields between them. The crystal can be considered as a composite model of soft regions bounded by hard 'walls' of forest dislocations. The forest occurs by the interaction of dislocations on different planes. The flow stress is then a spatial average of the local flow stresses in the hard and soft regions [16].

Although it is difficult to interpret bulk properties from electron transmission foil observations, Keh [19] observed that on slight deformation in polycrystalline iron most dislocations were screw dislocations. It is possible that the dislocations that caused the deformation have passed and only the dislocations that were unsuccessful in contributing to the deformation (immobilized dislocations) are seen.

Li [10] presumes that dislocations form by being emitted from grain boundaries and other interfaces. It is possible that dislocations can exist in the form of ledges in the grain boundary. When grain boundaries are not atomically flat a grain boundary ledge exists. A ledge may also be due to the absorbtion of a dislocation onto the

grain boundary, the "absorbed" dislocation can simply be "desorbed" from the grain boundary upon the application of a shear stress (Figure 2.7). Although individual ledges may donate one or even two dislocations, a multiplication process is still required during the dislocation movement in the grain. At the time of yielding it is assumed that multiplication within the grain has not yet taken place to any great extent, and the dislocations inside the grain can be taken as all having arisen from the ledges in the grain boundary [10].

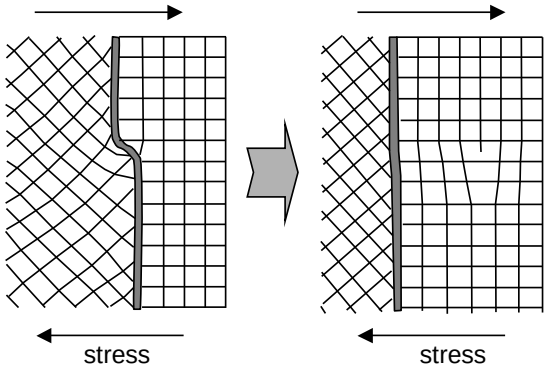

Figure 2.7: Grain boundary ledge acting as dislocation donor after Li [10].

The number of dislocations in the grain is proportional to the number of ledges, while the number of ledges is (approximately) proportional to the grain boundary area. Thus the number of dislocations per volume is proportional to the area per volume. Since the area per volume of the grain is proportional to the inverse of the grain diameter, the dislocation density at the time of yielding should be inversely proportional to the grain diameter. Li backs this claim using Brandon and Nutting's[18] results. They [18] measured dislocation densities from electron microscope images. It was shown that only forest interaction occurred with fine-grained ferrite while sub-grain boundaries (more dense than forest interactions) are formed in coarse-grained ferrite. This assumes that all the grain boundaries have the same density of ledges (which is unlikely) or the boundaries are some weighted average of high angle grain boundaries and low angle grain boundaries.

However, more precise measurements would be required to substantiate the relation between initial dislocation density at the time of yielding and the grain size. If such a relation exists it relates flow stress to the square root of the dislocation density.

This would lead directly to the Hall-Petch relationship [20, 21]:

$$\sigma_{ys} = \sigma_i + k_y d^{-\frac{1}{2}}, \tag{2.1}$$

where σ_{ys} is the yield strength of a polycrystalline sample, σ_i is the overall resistance of lattice to dislocation movement, k_y is the 'locking parameter' that measures the relative hardening contribution of the grain boundaries and d is the grain diameter.

It should be added that even a Hall-Petch explanation of lower yield has complications as there is a strong inter-relationship between σ_i and k_y in steel[22]. Mintz, Ke and Smith showed that k_y is large when segregation of interstitial solute to grain boundaries is high [23]. Carbon adds the major locking component and the ease of dislocation nucleation from the boundaries is reduced further.

To summarize the behaviour of dislocations at yield:

1. At high enough stress, ledges dissociate from grain boundaries and form dislocations
2. Small grain size results in more ledges, thus higher yield ($\sigma_{ys} \propto d^{-\frac{1}{2}}$)
3. Small grain size means that carbon can diffuse to ledges quicker and pin them more effectively increasing k_y, also contributing to higher yield stress ($\sigma_{ys} \propto k_y$).

In continuing deformation dislocations must multiply. The Frank-Read multiplication mechanism would exist when dislocations tend to stay on one slip plane. Thus the operation of the Frank-Read mechanism must be modified when dislocations can move on to cross slip planes. It is clear that cross slip occurs readily in ferrite [18] and most dislocations are characterized by a combination of screw and edge parts. If the dislocations cross-slip frequently, and do so, before the two half loops bulging out from the Frank-Read source can combine, then one or both of the half loops that cross-slip will not combine. Thus the Frank-Read source cannot renew itself, although many segments are formed by cross slip. Such a dislocation multiplication process would not produce a pile-up [10]. Pile-ups could explain Hall-Petch behaviour but are rarely seen in iron [18].

In this study the effect of precipitates on dislocation creation will be ignored, since this is an extrinsic effect and an effort will be made to eliminate it.

Cross slip is most likely induced when internal stresses build up from extensive interaction between dislocations and external stress. The result is the lengthening of dislocations, and more dislocation interactions. The dislocation interactions within the grain would cause edge dislocations of the same sign (and in the same system) to attract one another and line up to form a sub grain boundary. This differs from a pile up in that the dislocations in a pile up are orientated as to repel each other (see Figure 2.8). Such a cluster may continue to become more resistant to decomposition by external stress as more dislocations are added. Li [10] calls a collection of dislocations from a single system of the same sign a cluster [10]. If a dislocation from another system joins the cluster then a tangle will form [10].

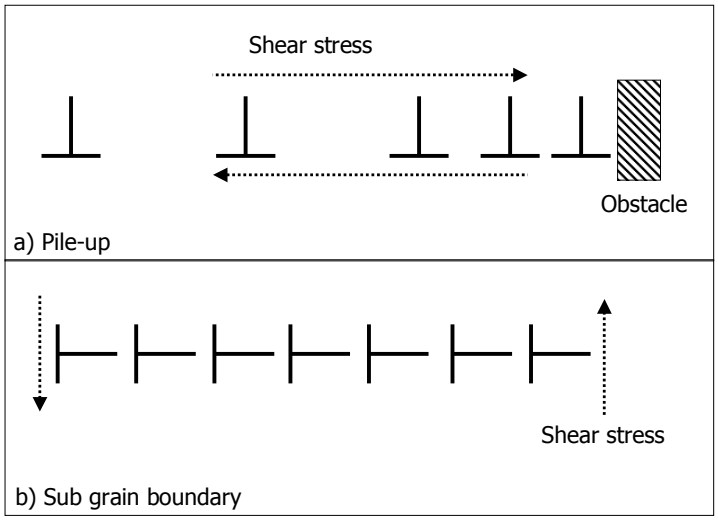

Figure 2.8: a) Pile-ups in a grain. b) Sub-grain boundary.

The average distance between clusters is affected by the frequency of cross slip and dislocation encounters, which in turn is affected by the external stress and the rate of deformation. However, once tangles start to form they become effective traps for dislocations so that new clusters will not form. This is a function of the density of the tangles, and with few tangles more clusters will form. The apparent cell size is governed by the average distance between tangles. In other words the cell size would depend on the cluster density at the time when the secondary system starts to operate or when tangles start to form. Thus cell size, although inversely proportional to the stress, will also decrease with increasing impurity content and decreasing grain size [10]. Keh and Weissmann [19] studied the effect of strain on cell size and found that the cell size initially decreased with increasing strain and then reached a constant value after around 8% strain. This would correspond to the

end of tangle formation as Li suggests. The real situation may be more complex as although the cell size may remain constant, the boundaries will keep taking up dislocations[19]. This implies that the misorientation across the boundary will keep increasing (this is of less importance in this study).

Li's observations also indicate that there will be an increase in the yield stress in ferrite when the strain rate increases or when there is a decrease in grain diameter. It also ties in with a study of tantalum single crystals by Weissmann and Hosokawa [24] where evidence of two equivalent systems operating in the pre-yield (or microstrain region) is shown. At the upper yield, they find that the one system stops operating and the second system continues. Döner and co-workers [25], show how dislocation clusters in ferrite begin to develop after 0.5-1% strain, and after 3-4% strain the cells are present in isolated areas. This could also be taken as evidence for forest hardening. They showed that the distribution of dislocations is essentially constant for a constant equivalent strain when the stressing is unidirectional and concluded that within the experimental errors involved, for the same equivalent strain the same dislocation density is seen irrespective of whether the deformation is carried out in tension, combined tension-torsion or torsion, provided the direction of the straining is not reversed [25].

Tangles account for the lack of softening after unloading. Softening upon annealing would result from the re-arrangement of dislocations. Tangles would also explain the Bauschinger effect [10]. The latter is explored further in the next section. Li's [10] work on bcc deformation has not received wide acceptance [26], although it is still considered one of the better theories [22] that do not invoke a pile-up mechanism.

Mughrabi [27] also developed a model for describing the cell structure that develops during deformation (although the greatest application of this model is at deformation levels much higher than would be encountered during yielding). He uses composite concepts to describe heterogenous dislocation distributions. The composite model consists of a heterogenous dislocation distribution with dislocation cell walls having a non-negligible or finite thickness. There are three types of dislocations; the dislocations in the cell walls, those in the cell interior and interface dislocations which maintain compatibility. He quite successfully demonstrates the applicability of this model to the continuous yielding material by considering each part of the composite as perfectly plastic- elastic, but with different plastic stresses [27].

2.2.2 Bauschinger effect

The Bauschinger effect (named after the person who first observed it in 1886) is the stress-strain anisotropy that occurs in materials when the direction of strain is altered [28]. In the narrowest meaning, the Bauschinger effect is the transient softening that occurs when the stress is reversed. On stress reversal there is also often a permanent softening[29], shown in Figure 2.9.

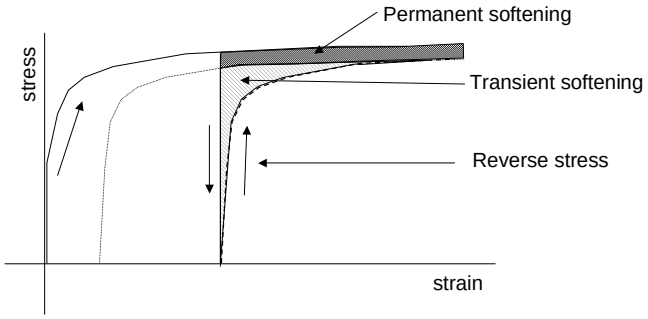

Figure 2.9: The transient and permanent softening effects that can occur on stress reversal, adapted from [30].

The result of the phenomenon is that mechanical properties after a pre-strain are a function of the direction of re-straining. A mechanism for the Bauschinger effect lies in the nature of the cold worked state, and Orowan's explanation is still favoured in textbooks [31].

Orowan [29] generalized that there are two broad categories of obstacles: strong barriers and permeable obstacles. The strong barriers are expected to promote back stress hardening due to some form of dislocation pile-up at the barriers (as seen in Section 2.2.1). Li [10] would equate strong and permeable barriers with dislocation tangles and dislocation clusters respectively.

Wilson and Bate [32] studied the effect of abrupt changes in the strain path on work hardening. They showed the transient reduction in flow stress during abrupt changes in the strain path is caused by the disruption of the initial pre-strain dislocation sub-structure. The strength of the dislocation walls rather than the grain size was found to contribute to the reduction in work hardening.

Wilson [30] took Orowan's idea of back stresses further. He explored the possibility that back stress hardening must be wiped out to a large extent by reversed plastic deformation, and that it would therefore give rise to a prominent "permanent" softening effect. This implies that part of the initial work hardening is permanently removed by reverse straining.

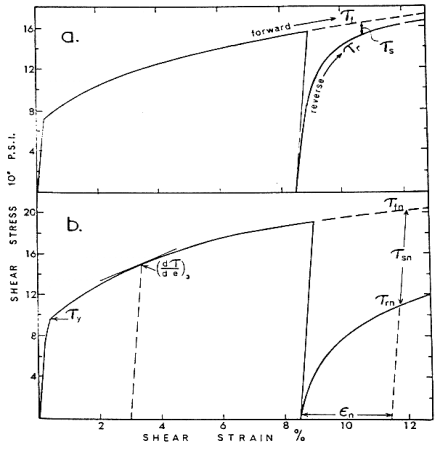

Figure 2.10: The effect of precipitation on the Bauschinger effect in Al-4%Cu: quenched from 525°C, for (a) 5hr, and (b) 340hr before straining, (b) is also used to define τ_s [30].

The evidence (in Figure 2.10) considered is, essentially, the difference in the absolute values of flow stress, for continued forward and for reverse straining, measured at the same total strain and beyond the point at which the two flow stress curves become approximately parallel. τ_s is given by the vertical separation of the flow stress curves measured beyond the first few percent of reversed strain. Wilson compared dispersion hardened metals (spherodised high carbon steel) with single phase materials (low carbon steel). He confirmed that the single phase materials suffered much less from permanent softening than the two phase materials [30]. Thus, the presence of a second phase is likely to affect strain ageing anisotropy by affecting the Bauschinger response of the material. Therefore, second phases should be avoided in the present study. In the case of low carbon steel, the second phase could include cementite (Fe_3C), ϵ carbides ($Fe_{2.4}C$), pearlite, sulphides and nitrides.

An alternative method of quantifying the Bauschinger effect is to 'convert' the effect into strain terms (after Deak [28]). This uses the concept of 'critical intermediate strain' (Figure 2.11). A sample is pre-stressed, and then the sense of the stress is reversed twice. This results in an intermediate reverse strain and then a final

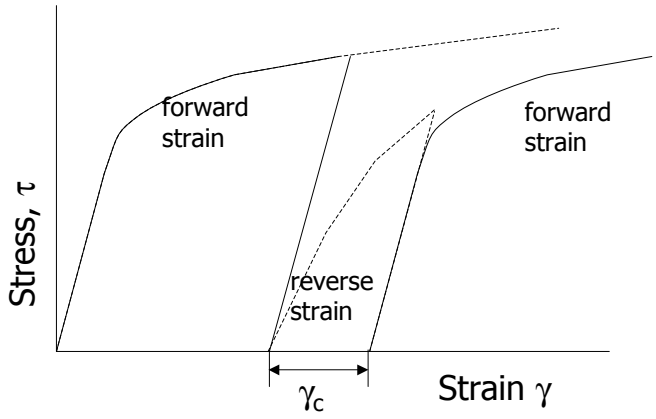

Figure 2.11: Critical intermediate strain, [28].

forward strain. At a small intermediate reverse strains, the permanent softening (at the end of the test) is not as great as at a higher intermediate strains. At a critical value of intermediate strain, the permanent softening disappears entirely. At this critical intermediate strain, the intermediate deformation removes the cause of the softening [28, page 65].

Orowan's [29] development of the theory of the Bauschinger effect considers a non-uniform distribution of obstacles. At a certain stress a dislocation will move through low densities of obstacles and come to rest up against a line of obstacles where the resistance or the density of the obstacles is at a critical value. If the stress is removed, the dislocation will remain where it is due to the friction stress, but on stress reversal will easily move back since the obstacles behind it are of a relatively lower density. Thus in forward motion the yield stress will be high, while in reverse motion there will be a low yield stress, until an equally dense row of obstacles is encountered[29].

A century after Bauschinger, Hasegawa, Yakou and Kocks [33] developed a model for the Bauschinger effect in fcc metals, which was very successful in predicting the effects above 7% strain where the dislocation cell structure is fully developed. At these higher strains, modelling of the plastic anisotropy of bcc metals is also being done [34]. Both of these models are based on the cell structure and are applicable to strains greater than will be experienced in this study.

In a TEM (transmission electron microscopy) study of tensile, torsion and tensile-torsion strains, Döner, Chang and Conrad [35] showed that although the dislocation density was constant for tension or torsion at equivalent stresses, on reversal the

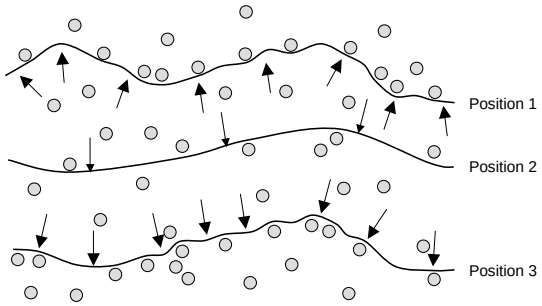

Figure 2.12: The transient softening effects that can occur on stress reversal, adapted from [29]. Position 1: Dislocation stopped at dense row of obstacles. Position 2: Dislocation can move backwards under reduced load until, Position 3: Dislocation is stopped by a row of equally dense obstacles.

dislocation density is reduced. It can be expected in the present study that this will occur during reverse torsion.

Pre-strain paths

Baird [36] summarized Wilson and Ogram's opinions on the effect of pre-strain path in the following way: "If a specimen is strained in tension and then re-strained in the same direction, most of the mobile dislocations will be unable to move far, since they will be pressed against obstacles such as grain boundaries, precipitate particles and dislocation tangles. If the specimen is re-strained in any direction other than that of the initial pre-strain, most of the dislocations (being a combination of edge and screw dislocations) will be free to move appreciable distances since the applied stress will be tending to move them away from obstacles that were blocking them" [37]. This is a re-statement of the Orowan concept.

Although in this dissertation only torsional reversal is considered, it is well established that the pre-strain path affects the return of yield point. Thus rolling, roller levelling and anisotropic pressing will affect the way steel ages.

Given the complex behaviour of dislocations under reverse loading, the next part of the picture should now be filled in, by looking at the effect of the interstitial solutes on the dislocations.

2.2.3 Yield point in steel

It was already well-known by the 18th century that if a steel specimen is strained, it does not have a yield point if re-tested immediately, but if the specimen is allowed to age, then the yield point returns [38]. Cottrell locking was first proposed in 1948-49 [1], as an explanation of this phenomenon of strain ageing. Prior to this, there were other theories including that of thin films of carbides that had to be broken before yielding could occur [39]. Other theories have been put forward subsequently, but have not gained much credence. Weissmann and Hosokawa [24] should be mentioned, they, rather heretically, suggest that discontinuous yielding is primarily caused by the relaxation of the strains on the first slip system as a result of the operation of the secondary slip system, rather than locking of dislocations by interstitials. This must be under the influence of interstitial carbon as interstitial carbon is required for a yield point in iron. Hahn [40] also claims that the importance of locking has been overstated, and can relate the yield and Lüders elongation to dislocation multiplication and velocities. However, such theories may be ignored for the design of the equipment.

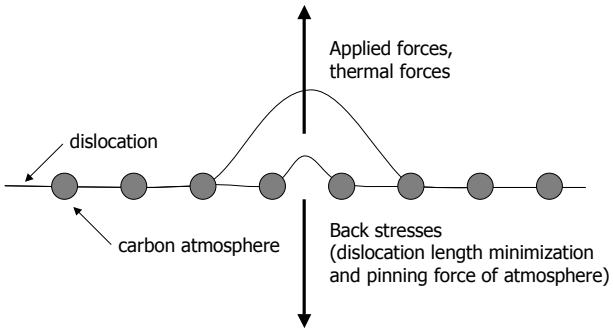

Figure 2.13: A dislocation breaking free from carbon atmospheres.

Cottrell and Bilby [1] describe how dislocations can break free from the atmospheres (Figure 2.13). A dislocation does not break free all at once, but rather bows out in a loop. The forward stress must overcome the sum of the back stresses. Forward stresses at room temperature would also include thermal fluctuations in the steel (which would allow loops below critical stresses to bow out) and external or applied forces. These would overcome the back stresses, which are the sum of the restraining force that the atmosphere exerts and the tendency of the loop to minimize its length (this assumes there are no other back stresses or obstacle stresses).

The first dislocation to be able to bow out would be in regions where the stress is higher (at a stress concentration). This unzipping of the dislocation from the atmosphere is then governed by the stress required to move two kinks sideways from the bowed out region. If the dislocation manages to escape the atmosphere, then it is able to accelerate, and sets up an elastic disturbance. The disturbance has the same effect as a localized thermal fluctuation, allowing other dislocations to break away, allowing yielding to propagate along the specimen [1].

The stress required to move an edge dislocation from its atmosphere was calculated by Cottrell and Bilby in their oft quoted paper of 1948. From the interaction energy per atom plane (U) (Figure 2.14), they calculated the corresponding force on a dislocation as a function of displacement. The binding energy is most strong when

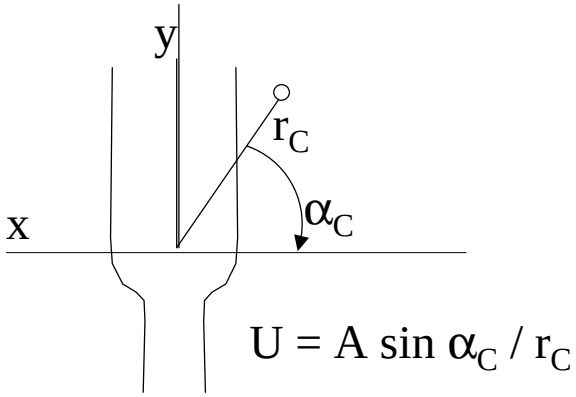

Figure 2.14: The binding energy of an edge dislocation to a solute atom at co-ordinates r_C, α_C.

r_C and α_C are $2 \times 10^{-10}m$ and $\frac{3\pi}{2}$ respectively. The binding energy per atom plane can be calculated and correlated to the maximum force. This is converted to the critical shear stress on the slip plane. In a tensile test the active planes are at approximately 45°or $\frac{\pi}{4}$ to the tensile axis, so that the critical tensile stress is

$$\sigma_0 = \frac{3\sqrt{3}A'}{4\lambda^2\rho^2}, \tag{2.2}$$

where A' is a parameter involving elastic constants [20], (3x$10^{-30}N.m^2$), λ is the slip distance in the dislocation and ρ is the equilibrium distance that a line of solute atoms lies away from the dislocation. By inserting known values of A', λ and a reasonable estimate of ρ, the upper yield stress at 0K, can be obtained [1]. This is an estimate for the upper yield stress, known to be dependent on other factors

such as stress concentration and thermal fluctuations which are not dealt with in the original paper.

Cottrell[41] observed in one of his early papers on strain ageing that it was not yet possible to decide on whether the dislocations responsible for yielding exist in dispersion throughout the lattice, or are assembled along the grain and cell boundaries. However, in relation to the mechanical properties, the upper yield point, where the first dislocation(s) break(s) free, marks the stage where plastic flow or yielding begins. The lower yield point is the continuation of yield heterogeneously through the gauge length [41].

Petch's [42] concept of upper yield is slightly more refined: In polycrystals pre-yield slip can occur in certain grains, but is confined within these grains. The upper yield point closely follows the eventual attainment of the stress at which the slip does continue into the next grain. However, the upper yield point is not coincident with the first such continuation, but when the spread of slip occurs across the specimen under more average circumstances. It thus appears that the upper and lower yield point of polycrystals are mechanistically very similar; both are concerned with the continuation of slip across a grain boundary, although in one case this slip occurs at the initial plastic nuclei, and in the other case at the Lüders front [42].

The correlation between segregated interstitial carbon and k_y, has also been explained in terms of a reduction in the grain boundaries' "permeability" to the Lüders front [22].

The effect of internal stresses on the yield point

Hutchison[43] showed that the upper yield was reduced in the centre of annealed specimens after bending the specimens around large radii, even when bending left no visible plastic deformation. Cottrell[44] referred to this work and pointed out that all manner of stress raisers will affect the uniformity of the stress before yielding and thus also the yield point.

The lack of an upper yield directly after temper rolling (and even at moderate ageing times) is another example of the effect of internal stresses on yield point. Butler and Wilson [45] found that sheets temper rolled about 1% will normally contain more than 50% of undeformed material with bands of dislocations (sketched in Figure

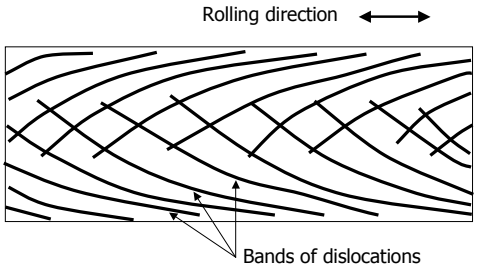

Figure 2.15: Sketch of a cross section through a 1% temper rolled sheet, dislocations revealed with Fry's reagent [45].

2.15); nevertheless such a reduction is sufficient to eliminate the sharp yield point, even in a steel of fine grain size. Moreover, the yield stress is reduced to a value well below that in the annealed material, and remains below this value after several weeks of ageing. The expectation that free dislocations within the deformed blocks will be effectively relocked by such a period of ageing (by nitrogen in the case of conventionally processed steel) is supported by the observation that, on straining in the rolling direction, the yielding occurs predominantly by plastic strain in the previously undeformed material [45], rather than the movement of dislocations in the deformed areas. Thus, the deformed areas are not a source of free dislocations. The lack of yield is, in this case, more likely due to the internal stresses rather than the lack carbon locking. These considerations suggest that internal stresses play a dominant role in controlling yield point behaviour.

The upper yield point is sensitive to stress concentrations, such as surface scratches or non-axial loading. Conversely, if the specimen is strained in one direction then all the inclusions (and presumably surface scratches) capable of acting as dislocation sources under that stress system will be used up (inactivated for subsequent dislocation generation) [44]. In the reverse direction, none of the stress concentrations have been blunted. This is a clearly anisotropic effect that would also influence torsion testing, and could be a significant contributing factor to the anisotropy of strain ageing.

Additionally, Mura and Brittain's [46] results from ageing under constant load showed that a yield point was not found even though an atmosphere exists. This indicates that more than just solute interaction with dislocations is important for a yield point; this ties in with Wilson and Ogram's work [4], as discussed in Section

2.4.1.

2.2.4 Solute interaction

Interstitials have three different effects on the yield point:

1. Snoek locking where the interstitial atom makes one jump to alleviate the stress near the dislocation. This takes around 1 second at room temperature and thus can be ignored in these tests.
2. Cottrell locking (will be discussed below).
3. Precipitation of carbides (also discussed below).

Considering Cottrell locking, during straining free dislocations are produced in the steel. Subsequently during ageing, interstitial atoms move to the dislocation core of edge and screw dislocations, and form what is termed a Cottrell atmosphere. This is favorable since there is a decrease in dilatation energy on the one side of the dislocation core. In the case of an edge dislocation, an interstitial carbon atom can relieve hydrostatic stresses and shear by entering the expanded region below the dislocation core. (The shear stresses in a screw dislocation could also be relieved as proposed by Nabarro [47]). During re-straining the dislocations must move from the pinned position, after which they are free. This means that a higher stress is required to free the dislocation than to continue moving it, hence the upper yield point [1].

The number of carbon atoms segregating during ageing to an edge dislocation has been estimated to be 1-2 per atom plane [36]. In the early stages of strain ageing, where the concentration gradients from segregation are negligible, the solute atom acquires a drift velocity, v given by

$$v = -\left(\frac{D}{\kappa \mathrm{T}}\right)\frac{dU}{dr_c}, \tag{2.3}$$

where D is the diffusion coefficient of carbon in iron, κ is the Boltzmann constant, and T is the absolute temperature. As before, U and r_c are the binding energy and distance of carbon atom from the core respectively (Figure 2.14). This equation holds as long as the concentration gradients are negligible, but as soon as the equilibrium

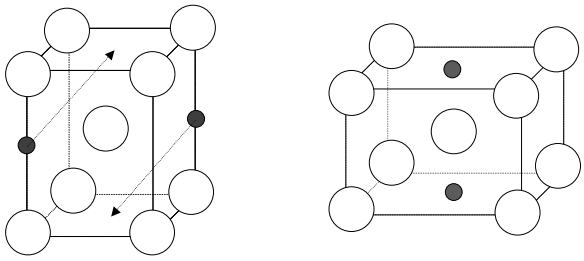

Figure 2.16: The movement of carbon interstitials in bcc lattice.

solute atmosphere density has been reached, there will be a back diffusion, and the rate of segregation around the to the dislocations will be decreased.

Cottrell's theory effectively shows how edge dislocations are pinned, but the pinning of screw dislocations by interstitials is more complicated. Nabarro [47] suggested that carbon in interstitial solid solution can contribute in another way. Nabarro based this on Snoek's analysis of internal friction. Carbon atoms may be found in the octagonal interstitial positions in bcc. If the carbon atoms all lie at the mid points of the edges perpendicular to (001), the lattice becomes tetragonal with (001) as the square base. If most of the carbon atoms jump to neighboring (010) interstitial sites the lattice becomes tetragonal with (010) at the square base, as illustrated in Figure 2.16. This shows that interstitially dissolved carbon atoms can relieve shear stresses by migrating to neighboring interstitial positions at a distance of only $\frac{\sqrt{3}a}{2}$, where a is the side of the elementary cell [47].

Clearly the presence of carbon or nitrogen is necessary for this yield point return, but it should be added that it is not a sufficient criterion. Mura and Brittain [46] performed experiment in which they aged under constant load and tested at various temperatures and they found that under constant load at temperatures sufficient to produce Cottrell atmospheres, discontinuous yield did not occur.

It is possible that dislocation line tension or the dislocation distribution are factors that also influence the yielding iron. Since, dislocations will "run back" if a stress sufficient to cause plastic strain is applied and removed. Other experiments of ageing under constant strain rate lead to the effects such as dynamic strain ageing, but will not be considered in this study.

Initially, the process of quench ageing will have a similar effect to strain ageing on the yield point. Quench ageing arises from the increased solubility of carbon and nitrogen at high temperatures (500°C). On quenching down to room temperature, the solute atoms do not have sufficient time to precipitate as carbides or nitrides. On ageing, the excess solute can precipitate, usually on dislocations, which will lock them and result in the appearance of a yield point [39].

The main differences between strain ageing and quench ageing are:

1. Quench aged steels harden on ageing, and then soften as they are allowed to overage, since fine carbides precipitate in the matrix or on dislocations, and with time at ageing temperature, coarsen [41].

2. Strain ageing only occurs after straining (dislocations required), while quench ageing occurs both in freshly quenched specimens and in strained specimens. [41].

3. The maximum hardening in quench ageing is reduced and its onset accelerated by increasing the ageing temperature. This is in contrast to strain ageing where a maximum strength is reached virtually independent of temperature in the region 0-100°C [41].

4. Quench ageing requires an incubation time whereas for strain ageing there is virtually none [41]. However, it is probable that the first step of quench ageing is still the formation of carbon clusters which would require virtually no incubation time.

5. Strain ageing should not contribute to a rise in flow stress in the material after yielding, since the dislocations should have broken free from the atmospheres and escape their influence. On the other hand, in quench aged steel there are still precipitates in the matrix that would still affect the flow stress [41]. However, dynamic strain ageing may take place. This is where the diffusion rate of the solute responsible for locking the dislocation and the dislocation velocity are matched, resulting in the relocking of the dislocations during the test and a serrated flow stress curve [39], although at room temperature this would only occur if the strain rates were less than 10^{-4}sec^{-1} [48].

In a way strain ageing does, at least at the upper yield, result in an increase in flow stress. The dislocation velocity (and thus local strain rate) with a few dislocations

that are breaking free is higher than the strain rate of a steadily hardening material (containing many mobile dislocations), which also leads to a rise in flow stress [49]. Additionally, it is seen that the dislocation structure in a steel that has been dynamically strain aged is qualitatively denser than in a conventionally tested sample (room temperature test), indicating that some dislocation multiplication must have occurred rather than dislocation unpinning [48]. Thus it is possible that a rise in flow stress may still be seen in strain aged material.

There is likely to be a smooth transition between strain ageing and quench ageing. Much work in the strain ageing has been done using internal friction methods in steel alloys that have been quenched from high temperatures, these have given a somewhat distorted picture of strain ageing. The study of these high initial solute content experiments might rather be called a study of quench ageing [36]

A good illustration of the effects of quench ageing is the set of experiments performed by Wilson and Ogram [4] in 1968. Four different dissolved carbon contents were obtained by decarburizing or quenching from temperatures of 200, 600 and 700^{o}C. The authors measured the increase in flow stress during ageing. In the steels that had low solute carbon, the increase in flow stress was much slower (but was still present). In the higher solute steels, the flow stress increased and then decreased again at longer ageing times. At the longest ageing, transmission electron microscopy showed evidence of precipitation on dislocations in the steel with the highest initial solute carbon levels [4].

The role of quench ageing can be quite subtle, as Elsen and Hougardy [50] have shown. Carbide precipitation can occur in bake-hardening steels at temperatures as low as 50^{o}C at times of 100 minutes. Bake hardening steels were developed to harden (supposedly by strain or quench ageing mechanism after deformation) at the paint curing temperature of 170 ^{o}C.

In this investigation, care would need to be taken to avoid quench ageing effects since only the strain ageing phenomenon and its effect on yield point is under consideration.

2.2.5 Lower yield

The segregation of interstitial solute also affects the lower yield. Mintz[22] observed that the locking parameter, k_y, in the Hall-Petch equation (Equation 2.1) varies over quite wide limits (5-24MNm$^{-3/2}$) depending on composition and cooling rate. For a given composition, k_y varies in an inverse manner to σ_i. It was shown that [23] k_y is large when segregation of interstitial carbon at the grain boundary is high. This is presumably because the segregation of interstitial carbon to a grain boundary ledge would increase the stress required to transform the ledge into a dislocation. The presence of the lower yield is not of as much interest in this study as the upper yield. However, it would be desirable in this study to keep cooling rates consistent to avoid changing k_y.

2.2.6 Lüders strain

After the upper yield, strain aged steel yields heterogeneously. That is to say, after the upper yield point not all parts of the gauge length are deformed by the same amount, but rather from one or more areas as the material is progressively strained (at a stress corresponding to the lower yield). This is the phenomenon of the Lüders band. The interface between the unstrained and strained areas is known as a Lüders band front. All the deformation during this discontinuous yield process occurs within this narrow Lüders front. As the material in the front is deformed it work hardens, and resists deformation until the stress is raised, and so the front progresses to undeformed areas. Since the instantaneous deformation only occurs in these areas, the local strain rate is much higher than that measured over the entire gauge length. When the front has passed through all the material in the gauge length, the material has been work hardened (at a higher strain rate) to the same extent, corresponding to the Lüders strain [41].

Li[10] suggests that during the Lüders strain, dislocations are generated from grain boundaries or other interfaces; they form clusters and tangles within the grain at very early stages of deformation, even in the Lüders band, if the deformation is slow or at normal and elevated temperatures [10]. Thus, the beginning stages of work hardening do have relevance in this study, and the formation of clusters, and possibly tangles, are significant.

Döner, Chang and Conrad [25] embarked on a study to correlate the relationship of plastic deformation with dislocation structure that develops during the deformation. Performing tests on commercial iron in tension, torsion (with reversal), and combined tension-torsion, they saw that dislocation clusters began to develop after approximately 0.5 to 1 % strain. With increasing strain, these clusters became more dense, and after about 3-4% strain, cells occurred in isolated regions. Upon reversal, they observed a decrease in the dislocation density [25]. Thus, clustering occurs before the end of the Lüders deformation and will be important in the mechanism of strain ageing anisotropy. The effect of ageing on the reduction of mobile dislocations during reverse straining will also be of interest.

The Lüders strain has been found to be a proportional to $d^{-\frac{1}{2}}$ (where d is the grain diameter) [51]. This shows the importance of grain size and its effect on dislocation structure in the Lüders strain region and thus also the mechanism for the lack of yield.

Thus again it is seen that behaviour of the Lüders band is not a separate issue from work hardening or strain paths, and any successful theory would have to combine and account for all these factors.

2.2.7 Grain size

At the upper yield, (σ_{uy}), only a limited number of grains are deforming plastically [42]. Their total volume is low, thus the effective strain rate is high and the friction experienced by a moving dislocation can be estimated from [42] (by an "upper yield Petch equation"):

$$\sigma_{uy} = \sigma_{0(u)} + \Delta\sigma_0 \log\left(\frac{1}{N_i d^3}\right) + kd^{-\frac{1}{2}}. \tag{2.4}$$

Here $\sigma_{0(u)}$ is the value the friction stress would have if all the grains were deforming in isolation, $\Delta\sigma_0$ is the change in friction stress produced by a ten-fold increase in the strain rate, N_i the number of grains per unit volume actually deforming at σ_{uy}, d is the grain diameter and $kd^{-\frac{1}{2}}$ is the resistance to the spread of a slip band associated with the presence of grain boundaries. According to Petch[42] the relationship agrees with experimental measurements in which lack of uniformity has been minimized. Since then, the difficulty of making accurate measurements of upper yield has been acknowledged [20]. The yield drop in polycrystalline iron emerges as a strain rate

effect, although the existence of the upper yield in inhomogeneous yielding may still depend on dislocation locking [42].

It is useful to compare these ideas with the 3% silicon iron experiments of Worthington [52] where he applied Petch's work. In that study, he found that the mechanisms controlling the upper yield stress are significantly different for various grain sizes. The upper yield stress in fine grain material is the stress at which slip first propagates through grain boundaries. With intermediate grain sizes, slip can propagate through and be impeded by boundaries at stresses below the upper yield stress. It should be pointed out that there are differences in the behaviour of steel and silicon iron, for instance, under fixed testing conditions the yield drop is generally greater in mild steel than that in silicon iron, although the difference is less marked at fine grain sizes [52].

Metallographic evidence [53] shows that, at a given strain rate in a tensile test, the volume of grains experiencing slip at pre-yield strains, N/mm^3, is fairly independent of grain size. Thus, the deforming volume per unit specimen is Nd^3 and the strain rate in these grains is inversely proportional to this. If the dislocation structure in the deforming grains is reasonably independent of grain size, the friction stress $\sigma_{o(u)}$ in them at the upper yield point will then vary with grain size.

Consider the modified Hall-Petch equation [53]:

$$\sigma_{0(u)} = constant + \Delta\sigma_0 \log\left(\frac{1}{N_i d^3}\right), \tag{2.5}$$

where $\Delta\sigma_0$ is the increase in friction stress due to a ten-fold increase in strain rate, N_i is the number of grains per unit volume actually deforming and d is the grain size. At coarse grain sizes, $\sigma_{0(u)}$ falls to the constant value corresponding to $N_i d^3 = 1$, in other words all the grains deform simultaneously. Both the upper and lower yield points disappear and deformation is homogenous [53].

The effect of grain size on the rate of return of yield in reverse re-straining is important (Figure 2.2, page 6). At the larger grain sizes the return of yield is slower than that for smaller grains. The increase in flow stress is evidence that ageing has occurred but its product of a sharp yield was not apparent; the reasons for this will be discussed in Section 2.3.2.

In the present work, excessively large grains should be avoided, as clearly they will affect the upper yield point.

2.2.8 A summary of the effects of stress on a dislocation

Deak [28] summed up the forces/stresses that resist a dislocation moving under an external applied stress. The following are three main categories:

1. Peierls-Nabarro force.
   This force arises from the energy barrier a dislocation must overcome each time the dislocation is moved through an unsymmetrical configuration between symmetric equilibrium atom positions (the distance is half the Burgers vector).

2. Short-range back stresses.
   If a dislocation intersects other dislocations or particles or, for that matter, is pinned by Cottrell atmospheres, these will resist the motion of a dislocation up to a certain stress, after which the defect allows the dislocation to pass with no more resistance.

3. Long-range internal stresses.
   These are caused by widely spaced and strong obstacles such as grain boundaries, sub-grain boundaries and twins. Dislocations are generally stopped by the first barrier of this kind that they meet.

All the above are fluctuating forces on a dislocation to resist its motion [28]. Thus there are three different effects on the dislocations that depend on the dislocation spacing. Their interaction is likely to be extremely complicated so the elimination of the extrinsic effects (such as precipitates) should be attempted.

2.3 Directionality of yield in steel

There are two very similar experiments on reverse strain ageing anisotropy by Elliot *et al.* [3] and Wilson and Ogram [4]. Both have been previously mentioned in passing, but it is appropriate to discuss these results carefully. Both sets of experimeters[3, 4] used thin-walled torsional samples, as this is the simplest way of obtaining equal but opposite stress systems with a nearly uniform shear stress over the cross section of the specimen [31].

The details of the two experiments is summarised in Table 2.1.

Table 2.1: Table of previous experiments on reverse strain ageing anisotropy.

	Wilson and Ogram [4]	Elliot *et al.* [3]
Composition (wt%)	0.11C, 0.0022N, 0.47Mn, 0.08Si, 0.03S, 0.03P, 0.15Ni, 0.15Cu, 0.016Si, 0.01Al	0.2C, 0.42Mn, 0.005P, 0.003O, 0.15Si
Grain size	100μm and 26 μm	no details
Ageing Conditions	89^{o}C, variable times	120^{o}C, 1hr

2.3.1 Elliot, Orowan and Udoguchi [3]

Chronologically, Elliot *et al.* [3] were the first experimenters to perform an in-depth study of the effects of strain reversal on strain ageing, although the research was only published 35 years later. The pertinent result of these experiments is reproduced in Figure 2.1.

They showed that reversal without ageing in the yield range led to the Bauschinger effect. After ageing, where one expects the dislocations to relock, the effect is seen again. These researchers used grooved specimens to avoid axial Lüders bands forming on the sample [3]. They ignored the effect of large lumps of pearlite on the grain boundaries in their steel. This second phase (about 10% of the volume) may be more effective in producing micro scale residual stresses than an axial Lüders band.

They did not publish any theory, but suggested that this observation was not compatible with the explanations of the yield phenomenon based on the locking of dislocations by impurities (interstitials) [3].

There has been some unpublished discussion between Cottrell and Orowan [54], and in a second paper on the subject, Orowan [55] attributes all known features of yielding in iron to the reinforcement of obstacles to slip by carbon and nitrogen atoms. He comments that Snoek locking by nitrogen, which alone would anchor both edge and screw dislocations would lead to full strain ageing within a few milliseconds at 70^{o}C. He assumes that the dislocation network is not locked at stresses approaching the yield. He envisages "carbon reinforced obstacles", which slow rather than lock the dislocation movement and prevent the free run of dislocations. The dislocations

are thereby prevented from reaching velocities needed for multiplication until the stress is raised to the upper yield point. At the upper yield point, the dislocation velocity is sufficient to produce dislocation avalanches and the resulting pile-ups can break through obstacles, reducing the stress needed for further multiplication and deformation [55].

Any further experimentation should avoid a steel with pearlite. However, the manufacturing of samples with a groove to avoid the Lüders bands from forming axially along the sample would be a necessary incorporation into new testing.

As pointed out before, pile-ups are not seen often in iron, and this theory flies in the face of the established theories of the day. This theory never gained credence and it was never published.

Cottrell's stress concentration theory

A counter argument by Cottrell [44] considers the blunting and sharpening of stress concentrations. During forward straining all the inclusions (and presumably surface scratches) capable of acting as dislocation sources under that stress system will be exhausted [44]. This is presumably achieved by relief of local stress by plastic flow. Re-straining in the same direction after ageing will lead to a higher upper yield. In the reverse direction none of the stress concentrations have been blunted. The Bauschinger response in steels is due to the stress concentrations still being sharp in the reverse direction, so that a continuous yield may be expected.

2.3.2 Wilson and Ogram [4]

Almost simultaneously to Elliot *et al.*, on the other side of the Atlantic Ocean, Wilson and Ogram [4] were making a comprehensive study of the effects of grain size and ageing time on yield in reverse torsional straining. The results of interest are reproduced in Figure 2.2, page 6.

They observed that after pre-straining and ageing, the reverse flow stress increased with increasing ageing times. They suggest the mechanism for the weak yield point on reverse straining after ageing as follows: After pre-straining, the dislocations move backwards under the effect of the back stresses to rest against obstacles that are hard

enough to resist the back stress (this is Orowan's idea of transient softening). New carbon atmospheres are generated during ageing (these may be carbides at higher amounts of carbon in solution, higher ageing temperature or longer ageing times). However, at 89°C and ageing times of less than 200 min, the atmosphere formation would not be complete. Dislocations tend to group together at boundaries in high densities. In these local areas, there will be insufficient solute carbon for complete segregation (long range diffusion does not occur in the time available). Thus in these areas, the Cottrell atmosphere density will not be as high as the average atmosphere density [4]. On reverse loading, some of the as yet unlocked dislocations within the tangles are freed, leading to the absence of yield on reverse loading, at short ageing times.

Wilson and Ogram [4] showed that the time of return of yield, (Figure 2.2, page 6), as seen at around 200 min in coarse-grained steel, corresponds to the end of atmosphere formation as determined by internal friction studies [56]. However, considering that Baird [5] warns that many internal friction studies often used material in the quench ageing regime of the solute carbon, this result is complicated by this possible quench ageing effect.

Wilson and Ogram's [4] upper yield point return in small-grained steel may be affected by how the steel work hardens, as it is observed that cell size is likely to decrease with decreasing grain size [10]. This can also account for the faster yield return in fine-grained material. Fine-grained material would have smaller cell sizes and dislocation interactions during reverse straining would thus also be faster for a given strain. Also Brandon *et al.* [18] measured dislocation densities in α-iron from electron micrographs. It was shown that only forest interactions occurred with finer grained ferrite while sub-grain boundaries (more dense than forest interactions) are formed in coarse-grained ferrite [18].

Thus, the differences in the times for yield return in different steels of different grain size could be related to the dislocation structure. The lower density of dislocations in the fine-grained material would improve effectiveness of locking at short times, since the dislocations are less densely packed and thereby compete less for local solute carbon and are effectively pinned quicker than in the large-grained case.

A less expected result is that the flow stress (on reversal) increased before the lower yield point and the Lüders strain reappeared. Wilson and Ogram [4] eliminated

recovery after the Bauschinger effect as a cause, by studying X-ray diffraction line broadening. It was found that there was no significant X-ray diffraction line sharpening that would have indicated any recovery at the times and temperature of the ageing treatment [4]. A well-known criticism of X-ray diffraction is that it only 'sees' the crystals close to the surface of the material ($< 10\mu$m), where the material is predominantly unconstrained due to the free surface. While according to mechanics of solids, a thin-walled tube in torsion has low residual stresses, the greatest residual stress is expected to be on the surface. Butler and Wilson [45] reporting on the study of Ogram (who performed tensile tests with different pre-strain paths) suggested that the restoration of a sharp yield point when the second strain is in the transverse direction, after prolonged ageing, is not directly related to recovery from the Bauschinger effect. In conclusion, since the dislocation substructure is probably only at the very beginning of the formation, (a few separate cells - Section 2.2.1) and the times and temperatures are low, there is little likelihood of recovery.

An alternative explanation for the increase in the flow stress is that the weak locking stress is so low that it only contributes to the friction stress [29]. More recent work of Elsen and Hougardy [50] seems to indicate that it is not unexpected to have precipitation after 100 minutes at 50°C in clean, ultra low carbon steel, thus at least some of the flow stress recovery could be attributed to quench ageing. The increase in flow stress could also be an indication that fewer dislocations are moving faster (which increases the flow stress) - i.e. some are pinned, which returns to Wilson and Ogram's theory. This implies that dislocations which become active in reverse deformation are not effectively locked at normal periods of ageing prior to reverse deformation.

However, until the mechanism responsible for the directionality of strain aged yield point in stretched sheets has been identified (and indeed identified in torsional as well), the understanding of the more complex behaviour of temper rolled sheets will remain incomplete.

Baird[5] summarises Wilson's *et al.'s*[4] work as follows: "A specimen strained in tension and then re-strained in the same direction will result in most of the mobile dislocations being unable to move far, since they will be pressed against obstacles such as grain boundaries, precipitate particles and dislocation tangles. It would therefore be necessary to lock only a few isolated dislocations to produce a return of the sharp yield point. In contrast, if the specimen is re-strained in any direction

other than the original one, some dislocations will be free to move appreciable distances since the applied stress will then be tending to move them away from the obstacles that were blocking them. They suggest that the isolated dislocations may become locked before all those in tangles or pile-ups, especially at low solute contents, so explaining the different rates of yield point return. The dislocation sources operative in forward and reverse straining are different, the latter requiring more extensive segregation of solute to lock them than the former"[5]. This is based on the assumption that yield is not the motion of the first dislocation but rather the rapid multiplication of dislocations.

An unresolved issue with Wilson's work is the presence of residual stresses due to the formation of non-circumferential Lüders bands around the sample. Lüders bands forming axially along the sample will induce residual stresses [3]. Wilson and Ogram's [4] pre-strain is quite high (5%) (sufficient for the cell structure to form in some areas). The implication of the high pre-strain is that there will be greater permanent softening effect from the well-built cell structure, as well as higher residual stresses.

The above seems to indicate that anisotropy of yield point may not be a fundamental phenomenon of iron, rather it is the interaction of dislocations with precipitates. What must be established is whether this effect would occur in pure iron, without carbides, sulphides or nitrides, otherwise it is merely an interesting interaction between precipitation and dislocation effects, with a bit of solute interaction on the side. There may be some merit in increasing this study to fcc alloys that show yield point phenomena as well.

When the pre-strains are large, the deformation cell structure would be well-established and this would cloud the issue of 'yielding'; thus in any testing, smaller pre-strains should be used. This is difficult to achieve as the pre-strain in aged samples cannot be less than the Lüders strain or the sample will have regions of non-uniform pre-strain. Of great importance is the variations in ageing times, as it gives a clue to the effectiveness of dislocations pinning by Cottrell atmospheres.

2.4 A summary of proposed theories

The literature shows that the topic is very complex and the reduction in the number of variables is very important. The aim of this section is to study the mechanisms of the different theories and suggest pertinent testing that would give credence to the mechanism.

2.4.1 An illustrative explanation and proposed tests of Wilson's theory

This section aims to illustrate Wilson and Ogram's ideas, and the figures are developed from their descriptions [4] of the mechanism. The dislocation tangles in the figures (Figure 2.17 a-f) are simplified for clarity. Wilson and Ogram's theory fits both their and Elliot *et al.*'s [3] experimental results. The return of yield only after prolonged times - at times (in their steel) where the precipitation of coherent and even non-coherent carbides is expected - is a function of diffusion distances in dislocation tangles. After yield (and at strains greater than Lüders strain), a dislocation structure consisting of cells is present (Figure 2.17a). Unpinned dislocations move a short distance in the backward direction as the yield stress is removed; this is shown conceptually in Figure 2.17b). If a reverse stress is applied (without ageing) then the dislocations all move backward easily, Figure 2.17c. For short ageing times, carbon does not diffuse fast enough to pin all dislocations in a tangle, thus there are unpinned dislocations in a tangle (especially at the center) as in Figure 2.17 d). On reverse straining, these weakly locked dislocations are able to break free of the tangle, Figure 2.17e. On the other hand, if the material was strained in the forward direction, only a few dislocations are able to break free from the tangle. At longer ageing times the yield point returns due to the pinning of all dislocations in the tangle. Unpinning or the creation of new dislocations from new sources, with dislocation multiplication, would have to occur (Figure 2.17f).

If this material was aged under external forward stress, then the dislocations that remain grouped in the tangle as in Figure 2.17a, will also experience slower locking, thus it would be expected from this theory that ageing under this type of stress would result in a slower return in yield point than ageing under no stress. This is consistent with the observations of Mura and Brittain [46], where they observed that a yield point was not found even though an atmosphere exists when ageing under

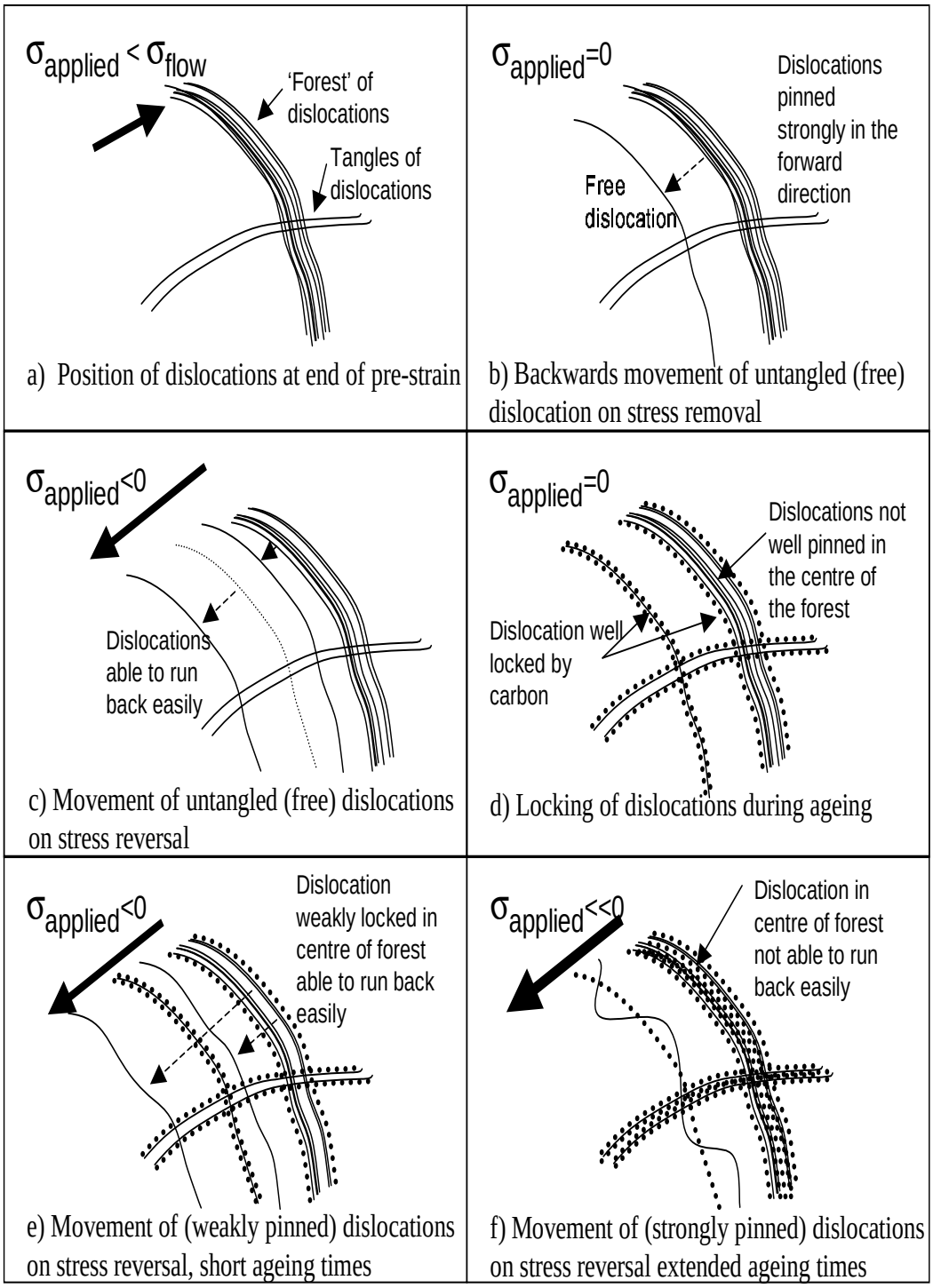

Figure 2.17: Position of dislocations at end of pre-strain. Some cell formation has occurred hence the presence of dislocations at 90°to the applied stress (developed from Wilson and Ogram [4]).

constant load. This could be explained by the fact that under load, the dislocations remain densely packed and thus all the dislocations may not be pinned.

Likewise if the material is aged at some intermediate reverse stress, the yield point should return quicker than when the material is aged under no stress. This experiment would be a good test of Wilson's theory. An alternative test would be to pre-strain to different amounts and study the yield return at different ageing times. From Wilson's theory, yield should return at shorter ageing times when the pre-strain is lower. The one provisor would be that pre-straining must be done directly after machining, to prevent Lüders band initialisation and allow pre-strain to be uniform.

2.4.2 Residual stress postulate

If it is assumed that it is not possible to obtain a 'residual stress free' sample after testing (that is after pre-strain), then it is possible to examine the effects that residual stresses may have on the yield point (as a mechanical effect). The roots of this theory are based on standard explanations of the Bauschinger effect [29], but have been expanded by the author of this dissertation to include strain ageing. For simplicity, tension-compression stresses will be considered. The figures are developed from these ideas.

Consider that in any polycrystalline material stressed in any direction there will be soft and hard grains. The reasons for the 'soft' and 'hard' grains (at around room temperature) can be attributed to orientation effects such as the Schmid factor (Figure 2.4), where grains that are unfavorably orientated will yield at higher stresses than those that are favorably orientated (the effect of the critical shear stress as a function of orientation is shown in detail in Appendix A). The stress strain curve of a polycrystalline metal characterizes the average modulus and yield. 'Soft' grains will have a significantly lower yield point than the hard grains as seen in Figure 2.18a) and b) (for clarity in the illustration the hardest and softest grain stress-strain curves are illustrated with exaggeration). The different grains may have marginally different shear modulus but this will be ignored for the purpose of postulate. When the stress on the sample is removed, the soft grains experience a residual reverse shear stress, while the hard grains experience a residual forward shear stress, Figure 2.18a. On reverse straining, the soft grains are very close to or at yield, as seen in

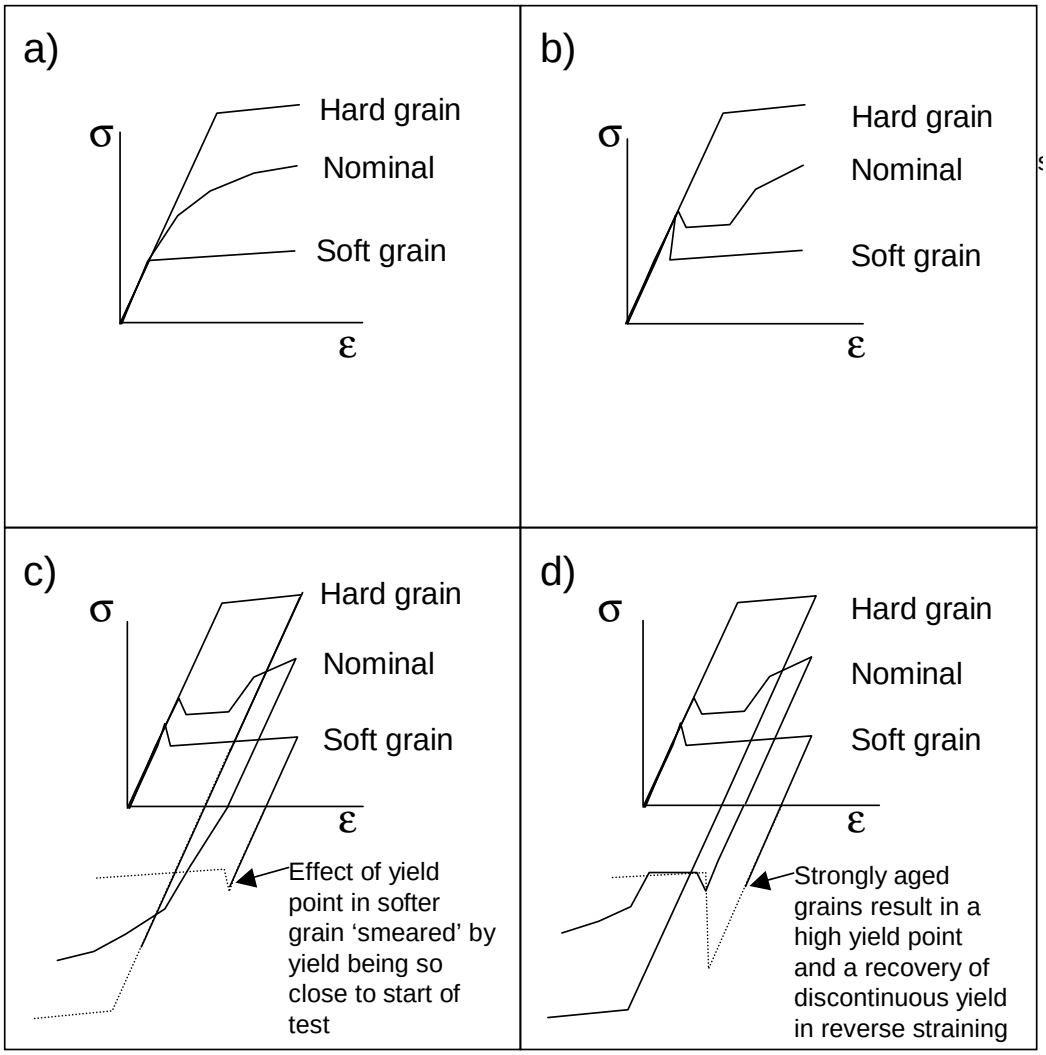

Figure 2.18: Stress-strain curves for polycrystalline iron, showing individual grain yields and the residual stress in the grains after the forward stress is removed. a) Unaged polycrystalline iron, after stress removal. b) Aged polycrystalline iron, after stress removal. c) Polycrystalline iron, after stress reversal. d) Aged polycrystalline iron, after ageing and stress reversal.

Figure 2.18b. This mechanism may now be extended to include the effect of ageing. When the steel is aged, the yield point returns in the soft grains, but this ageing is not sufficient to cause a yield drop in the bulk, Figure 2.18c. Finally, if a long enough ageing is performed then the yield in the soft grains increases, and since the dislocation structure in these grains is more developed than in the original steel or in the hard grains, there is more work hardening, Figure 2.18d.

A way of testing this hypothesis would be to take strongly textured sheet and test it both longitudinally and transversely with respect to reverse straining and return of yield point.

2.5 Research Methodology

In both of the previously reported testing methods[3, 4] there were drawbacks and advantages in the testing procedure that have been discussed (Section 2.3), these are listed here for clarity. Any further experimentation should avoid:

- Wilson and Ogram's[4] large pre-strains, where the deformation cell structure would be well established and hence clouds the issue of 'yield',
- Elliot *et al.*'s[3] pearlite punctuated steel where there are guaranteed to be spurious effects from the internal stresses (and possibly even residual stresses from the second phase).

However, further testing should incorporate

- the variations in ageing times as Wilson and Ogram's[4] experiments did,
- the groove in the samples as used by Elliot *et al*[3].

2.5.1 Torsional/stress strain testing

Most ASTM standards torsion testing is done using solid bars. The normal test procedures and parameters (strain rate, specimen geometery) are developed for that type of specimen. However, the current torsion test on a hollowed out bar (a tube is machined from a solid bar) is not the same. It is not possible to use the ASTM standards test procedures, as the sample design is deliberately different from the 'normal' test. It was decided to adhere to the previous experimenters [4, 3] parameters.

Preparation of material

Final test material may be prepared by decarburizing and recarburizing to the appropriate level [57]. The specimens can be machined and heat treated, using a wet hydrogen treatment for decarburization and a n-heptane-hydrogen atmosphere for recarburization. The aim of any treatment should be to obtain sufficient carbon in solution (3 parts per million) for the formation of atmospheres, but to prevent the precipitation of carbides and aluminium nitrides.

Hu [51] investigated the effect of phosphorus and tin on the Lüders band formation, and found that these elements, acting as grain boundary segregants, tend to increase the density of mobile dislocations generated from grain boundaries sources and thereby reduce the magnitude of the Lüders strain. These impurities may also interfere with the strain ageing process. Thus residuals should be kept to very low levels.

Larger grain diameters lead to smaller upper yield points (Equation 2.4 from Section 2.2.7). Ideally, fine-grain sizes would give a clear upper yield and simplify the equipment requirements.

Miyazaki, Shibata and Fujita [58] showed that the tensile flow stress is a function of the specimen thickness. When the ratio of specimen thickness : grain size is below a critical value (in their test, around 20), no yield point is observed in a tensile test. They also confirm that large grain sizes have the same effect as reducing the thickness of the specimen [58]. The sample thickness must meet a certain ratio of thickness to grain size (t/d $>$ 20 for grain sizes $30\mu m$ $<$d$<$ $180\mu m$) [59].

Therefore, the following heat treatment is recommended to refine the grain size and to give the appropriate solute content. It must austenitise the material, and then allow the formation of strain-free ferrite, after which the cooling rate should be as fast as possible to prevent grain growth and avoid precipitate ageing. The heat treatment that achieves this is a rapid heat to 915°C, 5 minutes at 915°C, furnace cool to 700°Cand then air cool from 700°C.

However, the dislocation substructure of ferrite is affected by the cooling rate during the phase transformation from austenite to ferrite, with higher cooling rates leading to sub-boundary networks [19]. The alternative is recrystallization in the ferrite region which produces grains essentially free of substructure. However, recrystallization in the ferrite region can only occur in pre-strained material and will, if not carefully controlled, increase the grain size.

Excess dissolved carbon (quench ageing) can occur in steels that are quenched from temperatures just below the austenitising temperature (AC_1) [41]. This sort of heat treatment should be avoided in the current research. Decarburising the steel to the required level should eliminate this effect. Additionally, k_y (Hall-Petch locking parameter) should be kept constant by ensuring that the cooling rates are kept uniform [22]

Lüders propagation

El-Magd, H. Scholles and H. Weisshaupt [60] have shown that the Lüders strain is not a material constant but increases with increasing strain rate. However, at low strain rates it is approximately independent of strain rate (quasi-static strain rates). This implies that the testing procedure should be kept to quasi-static strain rates. Verel and Sleeswyk[61] found that in Ferrovac (refined iron), the critical velocity of the Lüders band below which the Lüders strain is independent of strain rate (static loading) is 10^{-2}mm/sec. This is slower than the strain rate in Elliot *et al.*'s [3] work.

As a matter of course, if the number of propagating Lüders bands in the sample increases at a given overall strain rate, the strain rate in the band will decrease. The experimental strain rate must be kept as constant as possible to avoid changing the Lüders line speed and thus dislocation density in the cell walls (which would alter the rate of return of the yield point after ageing). However, depending on the number of active Lüders lines in the sample, the strain rate at the Lüders front is altered [62] for a constant overall strain rate. A design that ensures a constant number of propagating Lüders lines must be used. It would be advisable to use a grooved sample to ensure that a single Lüders front is started in every sample [3].

Behind the Lüders front there will be a constant amount of strain (dislocation structure). However, if the sample is strained beyond the Lüders region (similar to Wilson and Ogram's experiment [4], where the initial strains are 5%), then the substructure will change with the amount of strain.

This has implications for the design of the sample where the groove must be adequate for the formation of two circumferential Lüders bands.

Internal stresses

The effects of precipitation and second phases on the internal stress have been discussed. However, work hardening will also result in internal stress [63]. Internal stresses may cause a continuous yielding response. Thus, if in this study the material is strained beyond the Lüders band region (extensively work hardened as in Wilson and Ogram's work [4]), the strain rate must be low to avoid creating excessive internal stresses. Wilson has also remarked on the increase in the internal stress

from precipitation and the formation of dislocation loops around the precipitates [64]. The thickness of the sample will affect the internal stresses, thick-walled tubes have a stress gradient across their diameter [31].

Alignment of chucks

In both tensile and torsion [31] testing, the alignment of the chucks is important, especially when measurements are being done in the microstrain region (just before upper yield). Misalignment will cause significant bending stresses and localized flow, and reduce the magnitude of the upper yield.

Soft machines

A 'soft' machine is one that has much compliance during testing (Section 4.5.2). The same principle, that a soft tensile machine will not faithfully produce the upper and lower yield [65], can be applied to torsion machines. This effect must be quantified in any design (see Chapter 4.5.2). Dieter [31] also points out that screw driven machines are usually harder than the hydraulic type and thus would be preferred for this work.

Wolfseher, Inhelder and Helbling [66] adapted a tensile testing machine for torsion, where they effectively obtained pure torsional loads, at small torsional loads. However, in their adaptation, the presence of many thin flexible strand ropes (elastic) would affect the measurement of the upper yield as the spring constant of the machine would be reduced (refer to Section 4.5.2).

TEM work

It is of some concern what thin foil preparation of TEM will do to the dislocation structure. Li [10] showed some careful experiments where thin film measurements from aged and un-aged specimens were taken; these indicated that the thinning operation always retained a constant fraction of dislocations (even though it is expected that the aged samples would retain a greater fraction). Döner, Chang and Conrad [35] showed that with statistical methods in dislocation analysis, reproducible measurements were possible in TEM micrographs. Thus, with careful work, the TEM

could be a tool for the study of the strain-ageing anisotropy.

Chapter 3

Experimental Methodology

Originally the aim of the experiment was to explain a mechanical property (upper yield - or the lack of it) on a microstructural level. Initially, it was thought that this could sensibly be done by looking at the sub-grain cell structure.

There was also a brief foray into the theoretical modelling the Schmid factor in iron, and this is documented for completeness in Appendix A.

3.1 Preliminary Experiments

To try to relate the event of the upper yield with the microstructure, some preliminary work (07/97-09/97) was done in Switzerland with Professor Jean-Luc Martin of Génie Atomique, École Polytechnical Fédérale, Lausanne. These preliminary experiments were performed in an effort to gain insight into the effectiveness of TEM (transmission electron microscopy) as a tool to study this phenomenon. Two experiments were performed.

1. Using a low carbon steel of similar composition to Elliot *et al.*'s [3] as well as his sample dimensions, two torsion tests were performed.

2. The effect of varying amounts of pre-strain on flow stress and cell structure in an ultra low carbon bake hardening steel were investigated. This was done as a comparison to the cell structure formed in the torsion tests.

3.1.1 Low carbon torsion tubes

Figure 3.1 shows the proposed (an adaptation from Elliot *et al.* [3]) stress-strain history for a torsion test of a hollow steel tube. The heavy solid line indicates torsional strain in one direction and the light solid line the opposite direction. The strain reversal leads to the expected Bauschinger effect (the decrease in the value of the stress at which the curve deviates from linearity). The curve also rises above the yield level of the first test. If deformed steel is sampled and studied in the TEM then the dislocation behaviour in this region could be studied. This can be done on the same sample by selecting material close to the groove where the Lüders lines have already passed. For comparison, the dislocation structure of the undeformed material and unaged material will also be sampled.

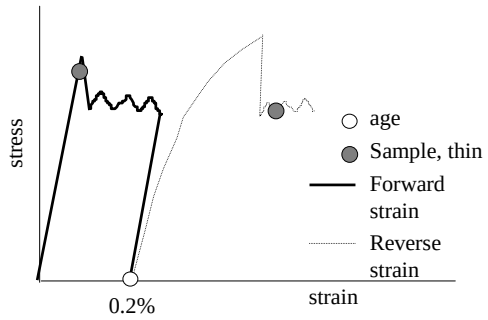

Figure 3.1: Expected torsion test results for AC2 samples.

Using a close match of the steel used by Elliot *et al.* [3], known as AC2 at Iscor Vanderbijlpark (refer to Table 3.1 for the composition and Figure 3.3 heat treatment), tests were performed using a very soft machine (the only one available at the time) on Elliot *et al.*'s style [3] torsion samples (Figure 3.2).

The results are shown in Figure 3.4. These results are fairly disturbing, as, although the aged sample had a higher upper yield, there was too much noise in the system to clearly see the linear portion of the curve. No conclusions can be drawn from these graphs, save that a far superior torsion machine had to be found. However, the material itself will still have undergone the required strain and thus could be used in Lausanne to examine the dislocation structures. Foils were prepared from material close to the groove as well as some distance from the groove. Discs were cut from the samples using an electro-spark cutting machine. This route was preferred over punching, which would introduce more dislocations into the material. The

Table 3.1: Composition of AC2.

Element	mass %	Element	mass %
C	0.17	Cr	0.02
Mn	1.41	Mo	0.01
S	0.01	V	0.003
P	0.008	Sn	0.003
Si	0.34	B	0.001
Cu	0.01	Al	0.052
Ni	0.01		

discs were then gently ground, leaving them relatively thick (75μm) before the final electrochemical polish. The polishing solution was 60% perchloric acid, 10% butyl cellusolve and 25% water in ethanol cooled to -5°C; the electropolishing was done at 25VDC. The foils were studied in a Hitachi HS-8-2 TEM (an ancient vintage) operated at 120KV. The material close to the groove was expected to have more dislocations than the material close to the shoulders as the Lüders lines are expected to initiate at the groove. The structures from the various foils are shown in Figure 3.5 to 3.6.

In both the aged and unaged samples, there are quantitative differences in the dislocation structure near the groove and at some distance from it. There are fewer dislocations in the material further from the groove (it is expected that the so-called annealed and 'undeformed' material is not free of dislocations, a dislocation free sample requires very special treatment).

The dislocations in the undeformed areas may have arisen during sample preparation (although the technique of preparing foils for dislocation analysis is a well-established procedure at Génie Atomique). It is possible that the samples may have deformed continuously (this cannot be determined from the stress-strain curves of Figures 3.4 and 3.4). Lastly, there may have been some deformation induced during the heat treatment. The last factor is quite plausible as the formation of pearlite (see Figure 3.6) during cooling will induce stresses into the pro-eutectoid ferrite as discussed in Section 2.5.1, therefore the dislocations might not be a result of sample preparation, but of cooling rate.

The dislocations in the aged sample do appear to be more "pinned" than in the

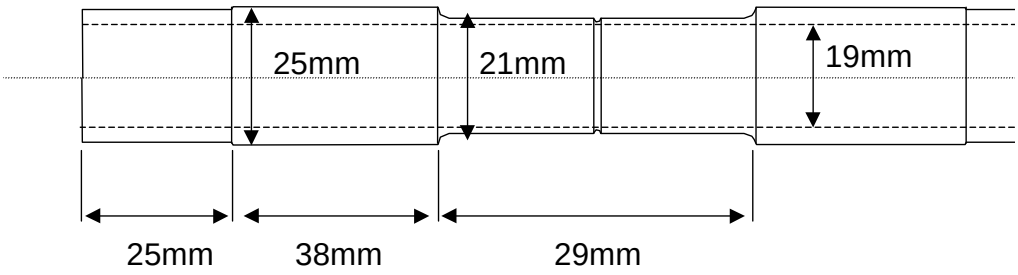

Figure 3.2: Sample dimensions for Elliot *et al.* [3] style samples.

unaged sample, as they tend have a more random orientation and are less linear, having many kinks, Figure 3.6 (left).

The precipitates in the microstructure would also interfere with dislocation motion. Although these were not analyzed, the bulk composition would suggest that these are either carbides, or sulphides. Pearlite was present in both the aged and unaged samples.

In summary, the TEM study shows that pearlite containing steels are not suitable for studying any 'pure' dislocation phenomena. The presence of the precipitates

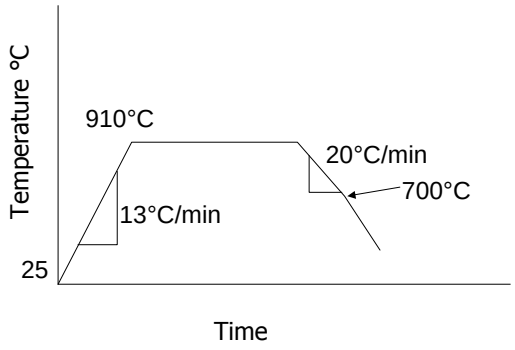

Figure 3.3: Heat treatment for AC2 samples.

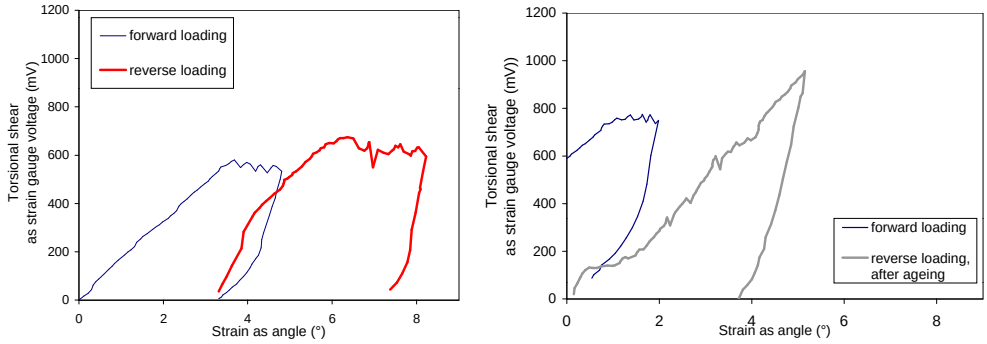

Figure 3.4: Torsion strain curves of AC2 on very soft machine, left: no ageing before reversal, right: aged before reversal.

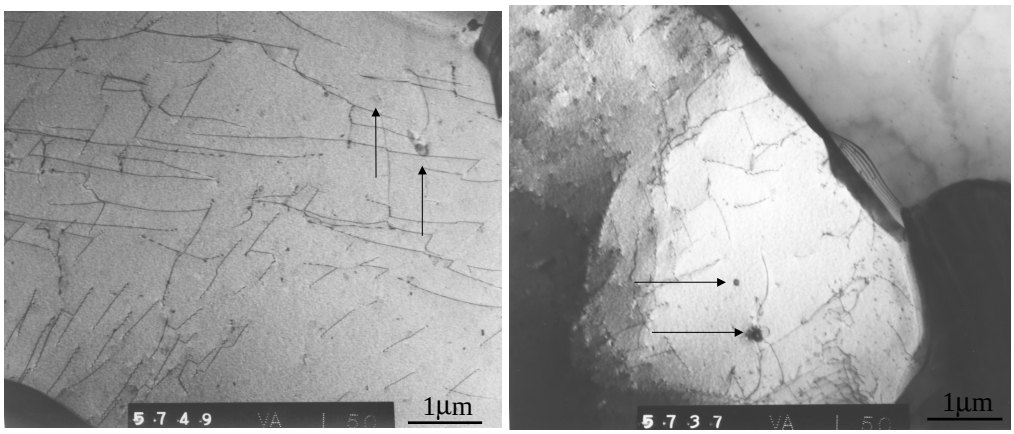

Figure 3.5: TEM micrographs of deformed material close to groove (left) and undeformed material some distance from groove (right) in the unaged AC2 sample. Arrows indicate precipitates.

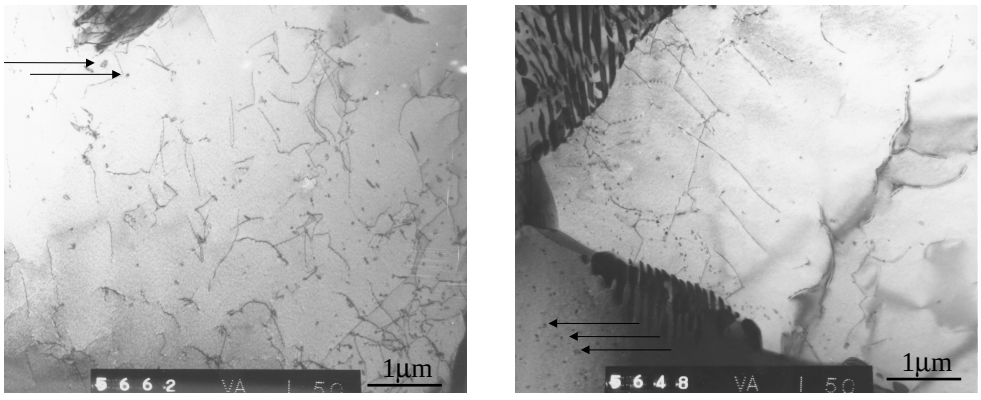

Figure 3.6: TEM micrographs of deformed material close to groove (left) and undeformed material some distance from groove (right) in the aged AC2 sample. Arrows indicate precipitates. Note the pearlite.

and pearlite would have interfered with the formation and mobility of dislocations and increased the internal stress which should have been reduced by using thinner samples.

It may be concluded that a superior choice of material would be a low alloy steel (low C, Al, Mn), or preferably a re-carburised pure iron to avoid complication of pearlite and precipitation in the test. Also, better equipment became a high priority.

Burgers vector analysis

In a pearlite-free area within the Lüders region (aged material), a Burgers vector analysis was done. The foil was tilted in the usual fashion to render the dislocations visible and invisible, according to kinematic theory. The dislocations' Burgers vectors ($\mathbf{b}$) would be visible according to Table 3.2, their projected angle (Θ) to the reflection can be calculated from

$$\Theta = \arccos\left(\frac{(\mathbf{b}\times\mathbf{z})\times\mathbf{z}}{|(\mathbf{b}\times\mathbf{z})\times\mathbf{z}||\mathbf{g}|}\right), \tag{3.1}$$

the operating reflecting plane is $\mathbf{g}$ and the $\mathbf{z}$ is the zone axis.

Table 3.2: Reflections and dislocation Burgers vectors where dislocations will be visible and invisible, and their angle to the reflection.

$\mathbf{b}/\mathbf{g}$	$\bar{1}\bar{1}0$	$0\bar{1}1$	$\bar{1}0\bar{1}$
111	invisible	invisible	visible, 30°
$1\bar{1}1$	invisible	visible, 150°	visible 30°
$\bar{1}\bar{1}1$	visible, 30°	visible, 150°	invisible
$\bar{1}11$	invisible	invisible	invisible

The analysis was done on three different orientations around the ($\bar{1}11$) zone axis (Figure 3.7).

A summary of dislocations and the Burgers vectors for some visible dislocations (Figure 3.8) shows three out of four expected types of dislocations are present (the fourth being $\bar{1}11$ which cannot be seen around this zone axis). Most dislocations are a combination of screw and edge type. The analysis is not of much significance, since there will be difficulties as mentioned before in relating the tangles to any mechanism in a meaningful way.

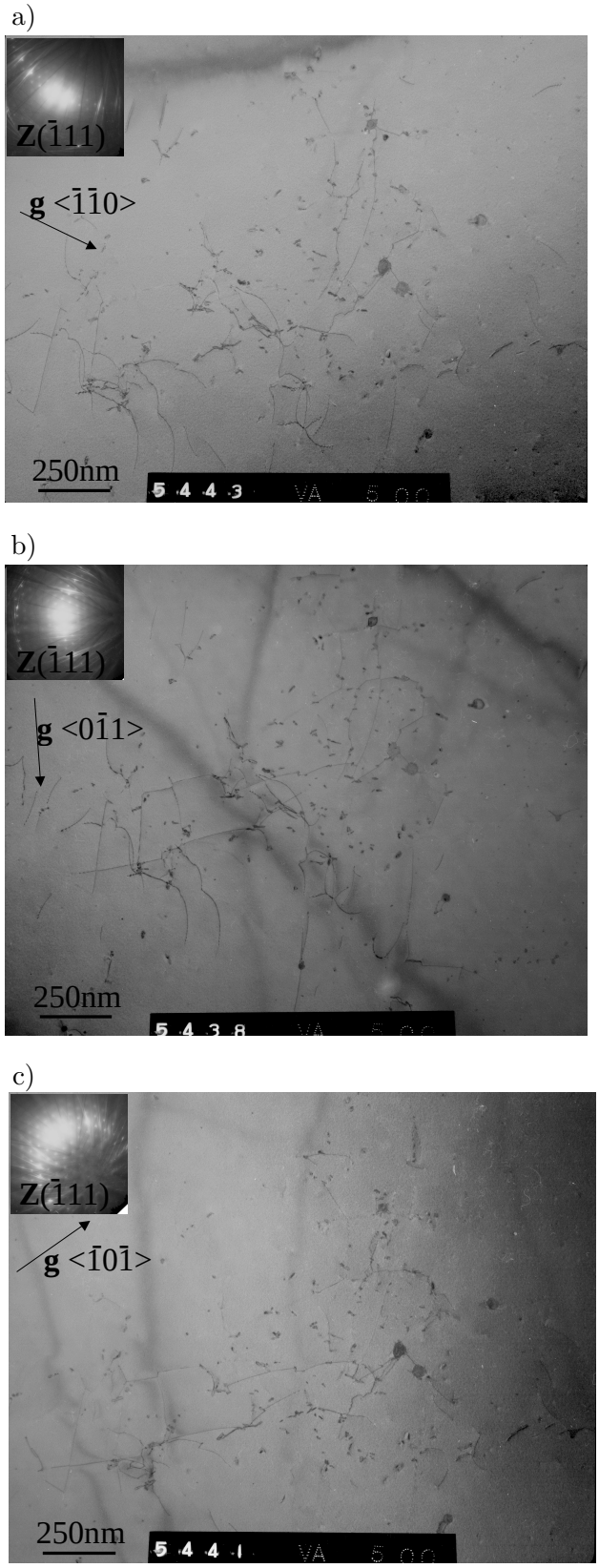

Figure 3.7: Dislocations visible in a) $\mathbf{g}\langle\bar{1}\bar{1}0\rangle$, b)$\mathbf{g}\langle 0\bar{1}1\rangle$ and c)$\mathbf{g}\langle\bar{1}0\bar{1}\rangle$. zone axis $(\bar{1}11)$.

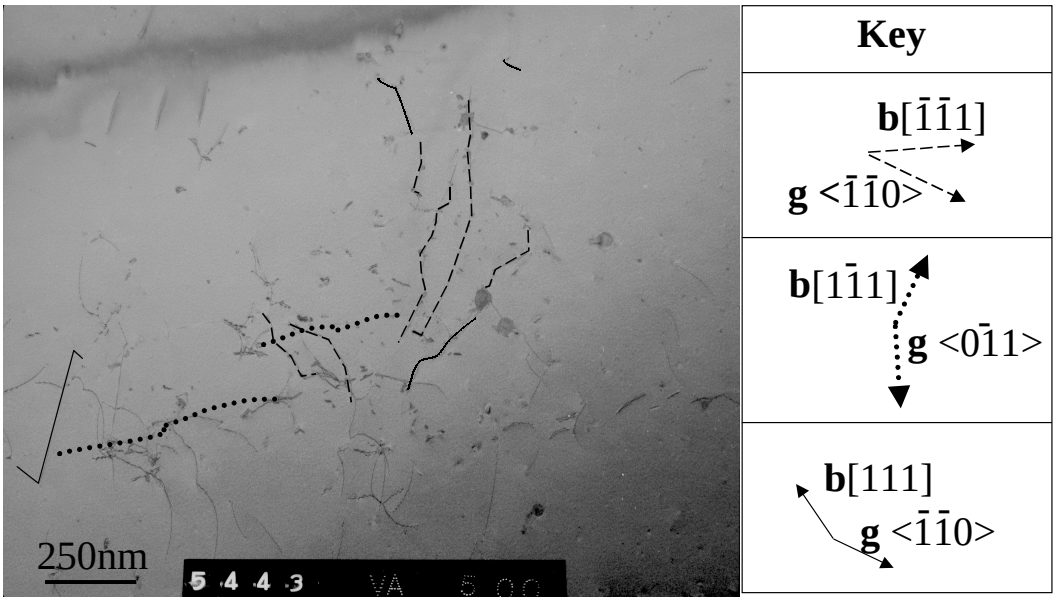

Figure 3.8: Summary of dislocations and the Burgers vectors for all visible dislocations; the line types (dash, dot and solid) correspond to the respective Burgers vector sets in the key.

3.1.2 Ultra low carbon steel tensile strain series

The behaviour of iron under repeated forward straining and ageing was studied. It was desirable to check the effect of Wilson and Ogram's [4] strains on the cell structure. The effects of these strains could be studied in the TEM. In this case, normal tensile samples could be used which made sample preparation easier. A schematic diagram of the stress-strain curves may be seen in Figure 3.9.

A low alloy steel (lacking the pearlite and of composition shown in Table 3.3) was obtained in the temper rolled condition. In this condition, this steel was known to be bake hardenable. According to Elsen and Hougardy [50], ageing at temperature of 170 °C for 30min material at strains above 2% ought to harden in 30 minutes as a result of Cottrell locking only.

Table 3.3: Composition of bake-hardening steel.

C	Mn	S	P	Si	Al
0.07	0.45	0.02	0.07	0.03	0.04

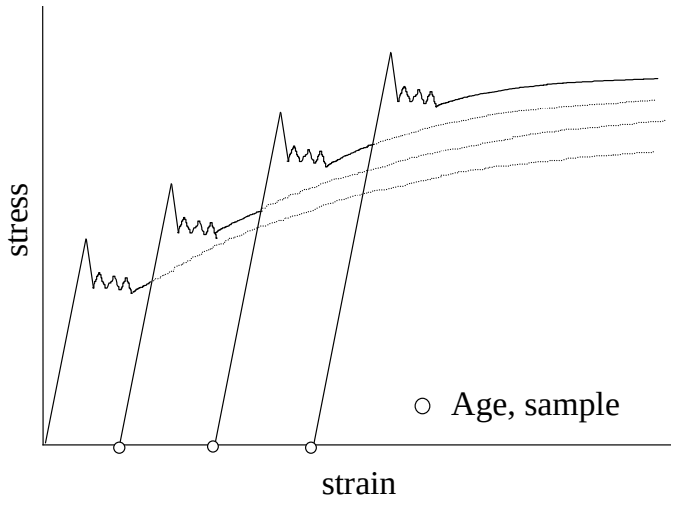

Figure 3.9: Proposed repeated forward strain on ultra low carbon steel.

The samples were tested on an Instron tensile testing machine at a strain rate of 0.0015 $\varepsilon.\text{sec}^{-1}$. No clip gauge was available, thus the strain was calculated from the cross head distance. The ageing was done at 170°C for 30min. The foils were prepared in the same manner as the AC2 samples (Section 3.1.1). The results are shown in Figure 3.10a-c.

The experiment confirms the lack of a cell structure at low strains (Figure 3.10a). The formation of sub-grain cells occurs between 1.8% (Figure 3.10a) and 4.5% (Figure 3.10b) and there is an increase in cell wall density from 4.5% (Figure 3.10b) to 5.45% (Figure 3.10c) and a slight decrease in cell size. A closer look at the stress-strain curve (Figure 3.11) of the material that is strained three times and aged twice shows that the work hardening (flow stress curve rather than the yield point elongation) does not rise above the original curve - within the accuracy of the test equipment used to test this material, which is clearly inadequate (a clip gauge would be required). So to examine these effects properly, improved testing equipment is required.

From this experiment, it is clear that there are a few variables that are not fundamental to the problem/phenomenon, and these must be eliminated. Thus, the selection of a steel that avoids a complicated microstructure, and a test technique that is accurate to the levels of these stresses should be chosen.

a)

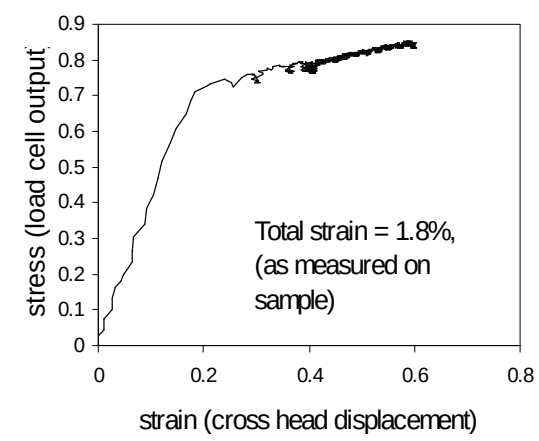

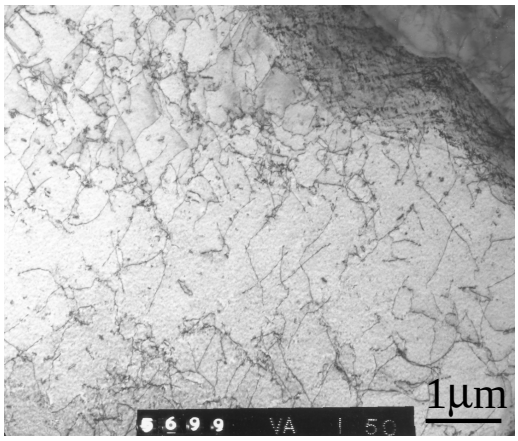

b)

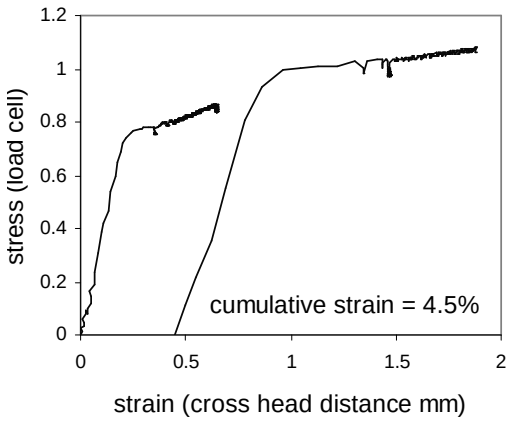

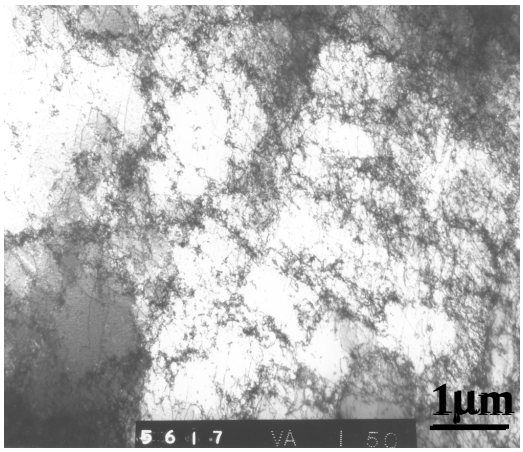

c)

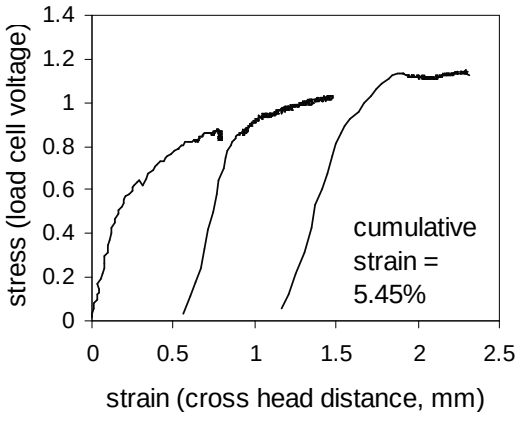

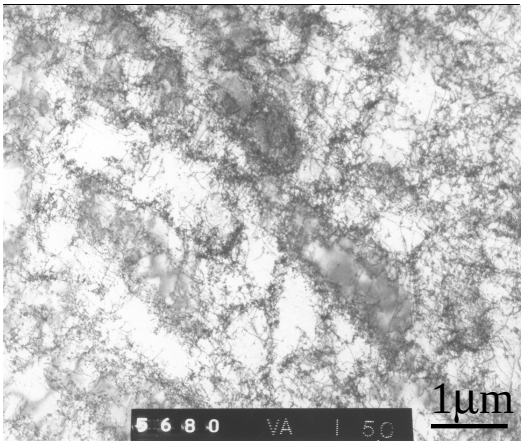

Figure 3.10: Low carbon steel strained to a) 1.8%, b) 4.5% and c) 5.45%. Aged before re-straining.

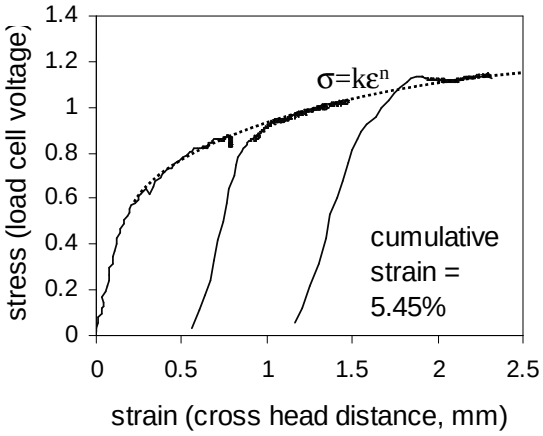

Figure 3.11: Low carbon, bake hardening steel strained to 5.45% with a power curve of the type $\sigma = k\varepsilon^n$ (n=0.26) superimposed.

3.1.3 Discussion of experimental work in Lausanne

The absence of an upper yield in the initial tests for Lausanne (Section 3.1) is either due to poor equipment or insufficient interstitial solute for strain ageing to occur. Since there is some indication of differences in the dislocation structures of the unaged and aged (dislocations appear pinned), the former is more likely, especially since the equipment was not specifically designed for the Elliot *et al.* [3] type samples. It is easily deduced from the results (Figures 3.4 and 3.4) that the torsion equipment for the Lausanne experiments is inadequate.

The lack of yield point in the second set of tests (Figure 3.10a-c) is more surprising, since these ultra low carbon steel are expected to be bake hardening steel. However, in using sub-size samples misalignment on the Istron could conceivably have resulted in greater amounts of pre-yield and thus the lack of upper yield. However, in the microstructure there was still the expected progression from dislocation tangles to a cell structure. Again, the torsion equipment for the Lausanne experiments is not suitable.

Clearly industrially 'low' carbon material (AC2) is not very suitable for studying any 'pure' dislocation phenomena. The presence of the precipitates and pearlite will interfere with the formation and mobility of dislocations. The air cooling from below 700°C is not expected [41] to result in a quench aged material, (Section 2.5.1), thus the precipitates in Figures 3.5 and 3.6, must be either nitrides or sulphides or

carbides that precipitated during air cooling.

In addition to this, it appears that a polycrystalline (as opposed to a single crystal) structure is unsuitable for meaningful transmission electron microscopy in this study. The problem is far more complex than that which can be easily solved using electron microscopy alone. It would be far more sensible to start with mechanical testing. However, the mechanical equipment must be able to measure very fine changes in stress and strain to yield sensible results.

Literature and Lausanne work

Since other authors [25] suggest that there is no difference in dislocation cell structures between tensile and torsion tests allows that the interrupted tensile tests (Section 2.2.1) be compared to Wilson and Ogram's structures. Wilson and Ogram's [4] pre-strain was 5%, while the strain in Figure 3.10b is 4.5%. Thus, this structure is approximately what is seen prior to reversal in Wilson and Ogram's experiment. Others [27] say that the tangles seen at 5% are not dislocation cells *per se*, since dislocation cells walls are much denser. Wilson and Ogram's suggestion that cell walls prevent easy pinning is maybe a somewhat optimistic, as the dislocations are not as dense as others[27] would say is required for cell wall formation. However, it is conceivable that at short ageing times, even this structure could be only partially locked.

However, the dislocation structure observed in Figure 3.10 does seem more established than the 'one or two grains' with cell structure that is described to occur at the end of the Lüders strain [18]. Moreover their density is significantly different from the density of dislocations in the torsional tests (which is a comparison with the Elliot *et al.* [3] work). Thus the issue of dislocation structure versus ageing properties has not been clarified, and there is scope for work in this area.

If Wilson's postulate holds (that the dislocations are not completely locked at short ageing times, as discussed in Section 2.4.1) then it is likely that the yield in reversal will return faster on ageing if the pre-strain is lower. Unfortunately Elliot *et al.* did not investigate the effect of ageing time on yield return. It would seem a necessary part of any further work to observe the return of yield with ageing time. It can be recommended that further work should also include experiments (as mentioned in Section 2.4.1) that involve strain ageing in situ, under load.

3.1.4 Conclusion of preliminary experiments

The preliminary experiments showed the difficulties of using 'normal' mechanical testing equipment, electron microscopy and a commercial carbon steel. This appears to confirm the opinion of Baird [36] who points out that since straining generally produces an inhomogeneous dislocation density, a given change in mechanical properties cannot yet be correlated with a known density of solute atoms on the dislocations. It was thus decided that more rigorous testing techniques (which would be mechanical testing) would be required. It was decided that the practical study of strain age anisotropy should start on this single aspect: designing the equipment capable of measuring these sorts of stresses.

3.2 Experimental design requirements

From the preliminary experiments at Lausanne it was seen that the issue of yield after reversal can easily be clouded by other issues such as second phases and internal stresses. Thus, the experiment must be designed to eliminate as many other issues as possible. The design must incorporate the necessary equipment with a realistic expectation of its limits

To summarize the aim of the equipment: The fundamental reasons for the absence of yield on stress reversal after strain ageing is being sought. A start would be to confirm the literature (see Section 2.4.1, 2.3.1) in regard to:

1. The absence of a yield point on stress reversal after strain ageing, (Elliot *et al.*'s work [3]),
2. the return of a yield point on stress reversal after strain ageing at long ageing times (this is similar to Wilson and Ogram's work [4], although the sample could be modified to include a groove to avoid inducing any internal stresses as well as investigating lower strains) and
3. investigate the Bauschinger overshoot,

while ensuring (from Section 2.5) that the material's

1. grain size,
2. amount of strain prior to reversal (dislocation structure),
3. available solute carbon (C_{sol}).

are optimal and that the machine

1. can accommodate the sample design,
2. has the correct strain rate,
3. has sufficient machine stiffness,
4. can measure the twist and torque on the sample with suitable accuracy.

For this dissertation, consideration of the following variables is required:

1. the sample design,
2. the machine stiffness
3. that small increments of twist and torque can be can measured with the required accuracy

The apparatus must be designed and tested to determine if it meets these criteria, so that, if successful, in the future it may be used for the strain ageing anisotropy research.

Chapter 4

Experimental Design

4.1 Design specification

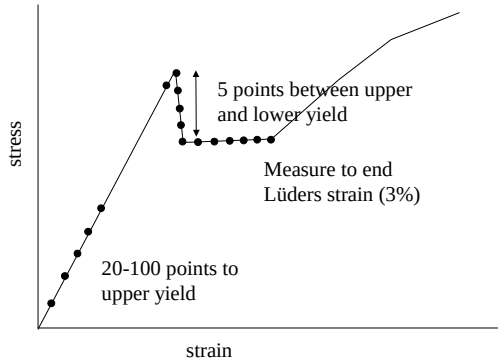

Figure 4.1: Schematic of the ideal number of measurements for test, discussed in detail in Section 4.4.

For the ideal design, the following features need to be resolved on the stress-strain curve (Figure 4.1), namely:

1. Upper yield,
2. Lower yield and
3. Lüders region.

The elements of a system to measure this adequately would be:

1. The frame to house the sample and other measuring systems,

2. A sample,

3. A strain measurement system and

4. A stress measurement system.

4.2 Frame

The advantage of using a torsion sample is that load can be more easily reversed than for a tensile specimen. Two possibilities existed, namely to upgrade an existing frame or to construct a new torsion machine. The former option was chosen due to budgetary constraints. The Avery torsion testing system at the Department of Metallurgy, University of the Witwatersrand, had very simple chucks for the sample grips which did not require clamping and thus eliminated a source of pre-strain. It was expected that the Avery was adequately stiff for the present testing purposes. The upgrading of the torsion machine is discussed later (Section 4.5).

4.3 Sample Properties and Design

4.3.1 Material Properties

Composition

The steel (composition in Table 4.1) was chosen to avoid the pearlite colonies and grain boundary carbides present in the steel that Elliot *et al.*[3] used.

Table 4.1: Composition of sample material.

Element	mass%	Element	mass%	Element	mass%	Element	mass%
C	0.018	Ni	0.010	Al	0.031	Zr	0.001
Mn	0.24	Cu	0.008	Ti	0.001	W	0.009
P	0.009	Cr	0.017	Nb	0.003	Co	<0.001
S	0.007	Mo	<0.001	B	0.0001	N	0.0025
Si	0.006	V	0.001	Sn	<0.001	Fe	balance

These microstructural features are expected to have a great influence on residual stresses in the material, thus the elimination of these would allow the study of the behaviour of the ferrite. Some grain boundary carbides could still be present (as this has been seen in steels with as little as 0.003%C [67]). Assuming that continuous annealing conditions apply (which is not strictly true), then a maximum soluble carbon is reached at carbon contents of between 0.010-0.015% [67]. This material would still have sulphides and nitrides in it. The Al:N ratio is high enough to avoid ageing with nitrogen, but would result in a small amount of AlN precipitation. For the purpose of testing the equipment, however, this material was deemed adequate.

Heat Treatment

Ideally, the material for study should be decarburised, however, for testing, as-cast material was used for convenience. Initially, the material was merely stress relieved. This was a heat treatment at 700°C for 2 hours, with furnace cooling to 500°C (cooling time 1hr 45min), after which the samples were removed from the furnace and air cooled. An austenitising treatment was performed on one sample as follows; a rapid heat to 915°C, 5 minutes at 915°C, furnace cool to 700°C, air cool from 700°C. The strain-ageing step was achieved by boiling (97°C) the sample in water for an hour (which is comparable to Elliot *et al.*'s [3] work where he aged at 120°C for 1 hr and Wilson and Ogram's ageing temperature of 89°C[4]). The prevention of oxidation of the diamond finish on the sample was investigated (refer to Table B.1 in Appendix B.1.1).

4.3.2 Sample Design

The sample was designed, in conjunction with the strain and stress measuring devices, to the following criteria:

1. Grips and diameter must be compatible with the Avery torsion machine
2. Must be thin enough to satisfy the "thin-walled sample criterion"
3. Fillet radius on the shoulder must be smooth enough to avoid increasing the stress concentration (K_{rR}) factor.

4. The notch must induce yield from the middle but must not reduce the fracture toughness excessively (must not appreciably alter the stress at which the sample fails). Ideally the notch should introduce a stress concentration in a small region compared with the specimen thickness.

5. Must not buckle under moderate strains.

6. Tolerances for machining (inner and outer) and allowable out-of-centre, must be known and accommodated.

Sample dimension design

The first limitation is that of outer radius, R_{outer}, which must be the same as that stipulated for the Avery torsion machine in the Metallurgical Test laboratory (Richard Ward building) at the University of the Witwatersrand.

$$R_{outer} \leq 8mm. \tag{4.1}$$

Thin-walled cylinders are difficult to machine accurately, since thickness variations inevitably occur during machining, especially with a large number of samples and age of the machining equipment (lathe) at Iscor. A comfortable machining thickness, t_{sample}, for the Iscor equipment is 1.5mm. With these two limits [68, page 165], the ratio of the actual (τ_{act}) versus approximate torque (τ_{approx}); ($\frac{\tau_{act}}{\tau_{approx}}$) on the outer radius of the sample is,

$$\frac{\tau_{act}}{\tau_{approx}} = \frac{4\left(\frac{R_{outer}}{t_{sample}}\right)^2 + 1}{2\frac{R_{outer}}{t_{sample}}\left(2\frac{R_{outer}}{t_{sample}} + 1\right)} \tag{4.2}$$

$$= 0.92, \tag{4.3}$$

so that a 92% approximation to a thin-walled cylinder can be achieved. The ASTM procedure [69] for determining the shear modulus at room temperature requires quite different geometry, (a longer narrower sample), but since the upper yield and the Lüders region is of greater interest these constraints will be ignored. Elliot *et al.'s* [3] samples have a lower thickness (0.9mm) but Wilson and Ogram [4] have the same thickness (1.5mm).

To prevent the Lüders band from initiating from the shoulders, or shear occurring at the shoulders [70], the shoulder fillet radius must be large enough so that the

stress concentration factor is not increased unduly. The stress concentration factor, K_{rR}, must be as close to 1 as is reasonably possible.

As seen in Table 4.2, with the dimensions of the mechanical laboratory sample (where R is the outer radius of the sample), the K_{rR} factor is around 1.1. The fillet radius r_{fillet} should therefore be greater or equal to that on the Metallurgical Engineering Laboratory design to be acceptable.

Table 4.2: Table of fillet radius to diameter and the corresponding K_{rR} factor.

	Mech lab design	Minimum ratio from Shigley [70]
$r_{fillet}/2R$	$10/15 = 0.7$	0.3
K_{rR}	close to 1.1	1.2

The second area that needs consideration in terms of stress concentration is the central groove. The groove's purpose is to induce a circumferential Lüders band in the centre; this will prevent the Lüders bands from forming axially from the shoulder fillets. Thus, the groove must have a significant stress concentration factor without inducing rupture at this point. The notch should introduce a stress concentration in a small region compared with the specimen thickness. Ideally, in terms of the testing, the best stress concentration would come from a notch that is machined after the machining and annealing of the samples but, in terms of machining, the risk of misalignment in a third machining step would be too high.

Referring to the Shigley's design criterion[70, page 680] reproduced in Figure 4.2, a stress concentration factor, K_{ts}, of 1.6 was selected as this is greater than the K_{ts} of the fillet, thus

$$K_{ts} = 1.6. \tag{4.4}$$

With a sample radius, R_{outer} , of 8mm and a groove of depth, (d_{groove}), of 1% of R_{outer},

$$\frac{2R_{outer}}{d_{groove}} = 1.01, \tag{4.5}$$

then from the graph in Figure 4.2 [70, page 680] $r_{groove}/d_{groove} = 0.15$ and the required radius of the groove is, at most,

$$r_{groove} = 0.4mm. \tag{4.6}$$

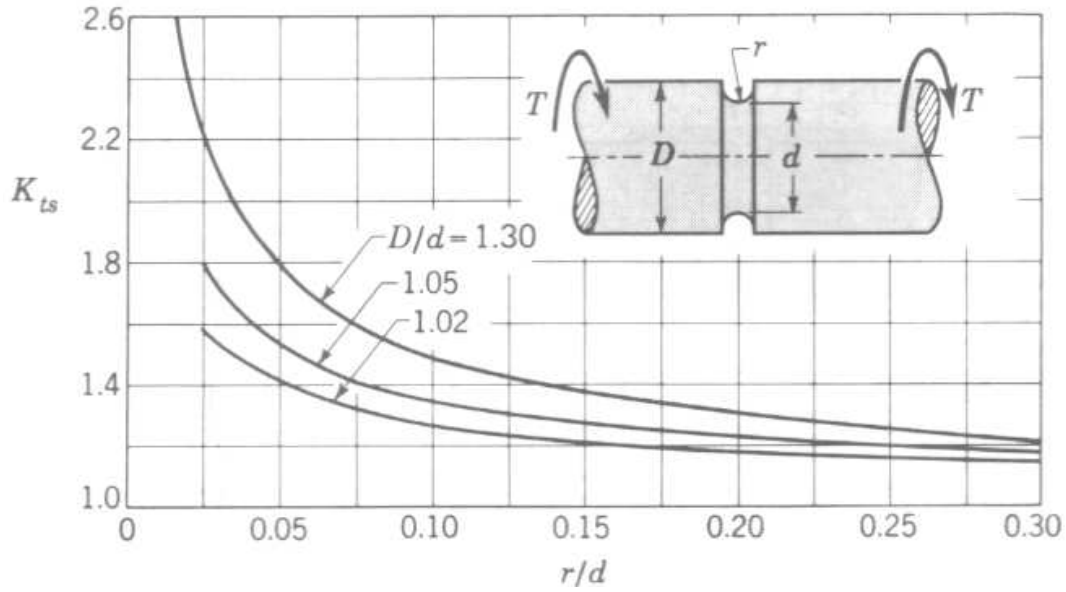

Figure 4.2: K_{ts} factors for grooved round bar in torsion, from Shigley[70, page 680].

Thirdly, buckling must be avoided. Unfortunately, conventional mechanics of solids cannot be applied as the sample is not being designed to resist yielding but to yield. Gere and Timoshenko [68, page 165] recommend a radius to thickness ratio of

$$\frac{R_{outer}}{t_{sample}} \leq 60, \tag{4.7}$$

for a long circular tube to prevent buckling in mild steel at normal working stresses. However, the strains they would be considering would be well below plastic flow, whereas the sample would be deforming plastically. Dieter [31, page 340] defines two criteria to prevent buckling when designing a torsion sample that will be deforming plastically. The first criterion is the ratio of length (L) to diameter (D_{sample}) which must be less than or equal to 10, or

$$\frac{L}{R_{outer}} \leq 20. \tag{4.8}$$

The second is the diameter to thickness ratio which must be less or equal to the range of 8 to 10, or

$$\frac{R_{outer}}{t_{sample}} \leq 4 - 5. \tag{4.9}$$

If, however, Equation 4.9 is to be fulfilled, then the design is no longer thin-walled; this would lead to internal stresses which would mask the yield point in reversal. In Table 4.3, these figures are compared to the actual sample design.

Table 4.3: Table of dimensional limits to prevent buckling.

Sample design limits from:	$\frac{R_{outer}}{t_{sample}}$	$\frac{length}{diameter}$
Gere and Timoshenko [68]	$\leq$60	
Dieter [31]	$\leq$4 or 5	$\leq$10
Sample design	$\leq$5.3	$\leq$10

Other important factors in the design include the tolerance (inner and outer) and allowable out-of-centre. These would result in variations in wall thickness. Premature yield and Lüders bands would be initiated in these regions. It was decided that the strictest available machine tolerances would be adhered to as the maximum permissible tolerances from the mechanical design point of view are difficult to ascertain.

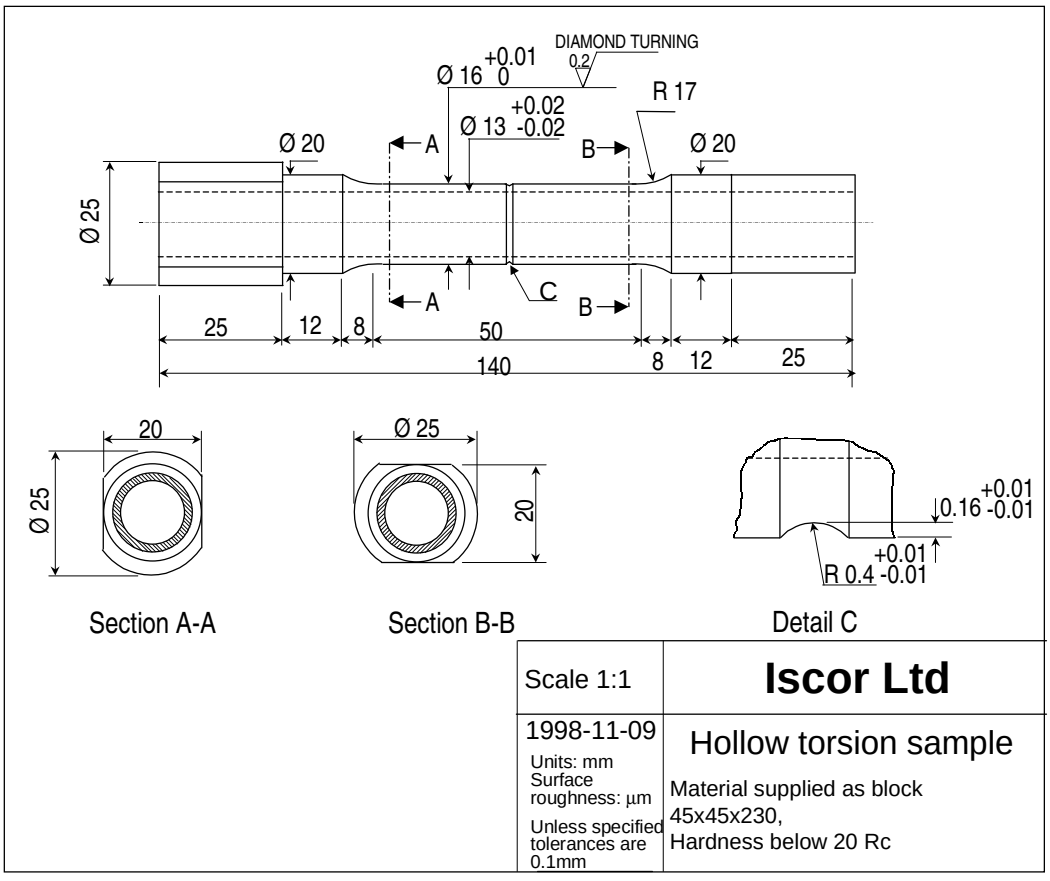

Figure 4.3: Manufacturing drawing of the sample.

Figure 4.3 shows a diagram of sample. The machining process was as follows; the bore was drilled, and then reamed out. The outer surface was machined "between

centres" on a numerically controlled machine. The final surface on the gauge length was diamond-finished. Finally, the flats on the sample grip were milled. The cost of machining the samples was kindly financed by Iscor at a cost of R10 000.

Estimated Yield, Strain, Torque and Twist

It is necessary to obtain the yield, strain, torque and twist that can be developed in the sample, since these will affect the design limits of the instrumentation.

The tensile yield strength (S_y) of fully annealed Iscor Grade AC1 is 190 MPa, while ultimate tensile strength is 270-330MPa. Using the maximum shear stress theory [70], the torsional yield shear (τ_y) is defined as

$$\tau = \frac{S_y}{2}, \tag{4.10}$$

thus the torsional shear strength is 95MPa, the shear strength is defined by the following relationship

$$\tau_y = \frac{T_y R_{outer}}{I_p}, \tag{4.11}$$

and the torque at yield is

$$T_y = 2\pi\tau R_{outer}^3 t_{sample}, \tag{4.12}$$

where T_y, I_p and t_{sample} are shear stress, torque, polar moment and thickness respectively. The elastic strain, γ, is

$$\gamma = \frac{\tau}{G}. \tag{4.13}$$

Thus the elastic twist, ϕ, at yield is given by

$$\phi = \frac{\gamma L}{R_{outer}}, \tag{4.14}$$

where L is the sample length.

4.4 Design of the strain measurement system

Strain measurements are usually performed by a troptometer [31]. This measures twist of the sample across the gauge length which is then converted to strain. The sample must be designed to accommodate the troptometer. The requirements of the strain measuring device are:

1. It must measure the range of strains experienced by the sample,
2. It must measure to the required resolution,
3. It must be compatible with the Avery torsion machine (where the outer radius of the sample is limited to 8mm, but the sample grips are 25mm in diameter).

The maximum strain on the sample during testing would not be the elongation to fracture, but the area of interest on the stress - strain curve in the steel. In any one direction, the maximum strain on the sample may be up to 10%.

For the first two criteria, the ideal stress strain curve from Figure 4.1 may be used and compared to values in the literature (Table 4.4). It was decided that ideally 100 points to specimen yield would be required, although 20 points to specimen yield would be acceptable, as this would allow roughly 5 points between upper and lower yield (Figure 4.1).

From Table 4.4 it can be seen that even the acceptable requirement (where there are only 20 points to yield) is far greater than either Elliot *et al.*'s[3] or Deak's[28] measurements. Additionally, there is a need to improve the strain system, if even the acceptable requirement is achieved. Deak's accurate twist meter only measures the small strains (3-4%)[28] and although Deak does not state the resolution specifically, the resolution may be estimated. The resolution on the strain gauge box with a maximum range of 2000 micro strain would be 10 microstrain. This would be what the optimistic eye could distinguish on an analogue scale.

The possible options for a troptometer, with their disadvantages are listed below:

1. The existing troptometer at the Mechanical Engineering Laboratory, University of the Witwatersrand, has a "death grip" on the hollow sample. The grips

Table 4.4: Strain measurement systems from literature.

Literature Source	strain resolution (%)	Points to specimen yield
Ideal	0.0012	100
Acceptable	0.006	20
Deak's vernier [28]	0.11	1
Deak's accurate twist meter [28]	0.023	5
Elliot *et al.*'s [3]	0.016	8
Existing troptometer at the Mechanical Engineering Laboratory, University of the Witwatersrand	0.0012	96

might deform the sample, producing stress concentrations which would result in Lüders bands forming from an area other than the central groove.

2. By using two lasers, and measuring their relative movements on a screen, the twist angles may be determined. However, mirrors would be required, and screen adjustments and instability have the potential to make this rather inaccurate.

3. A clinometer (this was tested and proved to be inaccurate, as may be seen from graphs in Appendix B.2.1).

4. Linear Variable Differential Transformer (LVDT) (rotary/large bore). This is expensive and none were available on a loan basis.

5. Shaft encoders can attain the resolution required (0.018° for 20000 counts per revolution), but do not have sufficiently large hollow shafts to accommodate the sample shoulders (25mm diameter)

6. An integrated distance measuring laser (which can measure the distance between two points and thus angles to a high accuracy), was considered but this also too expensive, and none were available on a loan basis.

7. Accelerometer which measures force (eg gravity. This can be used to measure change in force, such as when the accelerometer is turned and thus it can measure angle. The high accuracy type is expensive.

Of these it was decided that military grade accelerometers (obtained from Defencetek, CSIR and M. Brown of Grinaker) would be used. Two were, at the time of design, available on loan.

4.4.1 Final strain measurement system

Unfortunately, due to time constraints (availability) and budgetary constraints, only one accelerometer was used[1]. The actual equipment may be seen in Figure 4.4. The single inertial grade accelerometer used was a Honeywell Q-Flex, QA3000 accelerometer, supplied by Defencetek CSIR (specifications may be found in Appendix B.2.2 page 149). The range of this accelerometer is ± 25g (g is the acceleration due to gravity), so any range of angle or strain can be measured. The threshold resolution is $< 0.1\mu$g which for strain measuring equates to a resolution of $1\mu\varepsilon$.

The accelerometer (Figure 4.4) and casing was attached to an aluminium collar (Figure 4.5) using tight elastic bands. The casing provided a firm surface with the collar while the elastic band merely kept the two surfaces in tight contact. Conventional tensile yield extensometers utilize elastics to secure the system to the sample, it was thus not foreseen that the elastics would have any affect on the readings. The collar was positioned on the sample and attached to the sample with nylon grub screws. Nylon grub screws were used to ensure that the sample was not severely locally deformed around the screws.

Some error (noise) could have resulted from the use of gentle, but broad, nylon grub screws, where plastic strain on the sample under the screws could lead a movement of the accelerometer and thus a zero drift. However, this was a necessary compromise, the alternatives would have induced great stress concentrations (as cautioned in Hall's work [39]) on the sample and mitigate the effect of the groove. If experiments are done within the Lüders region, (so that the Lüders bands are initiated at the groove and do not reach the ends of the gauge length) it is unlikely that the Lüders front (plastic strain) will move under the grub screws and affect the reading.

The power supply and signal conditioning (as may be seen in Figure 4.6) was performed with circuitry specifically designed by CSIR for the accelerometer, while a simple gain board to amplify the signal to be suitable for input into the analog to

[1] M. Brown of Grinaker was unfortunately unable to deliver on the promise of an accelerometer and it was too costly to purchase a second accelerometer to replace it.

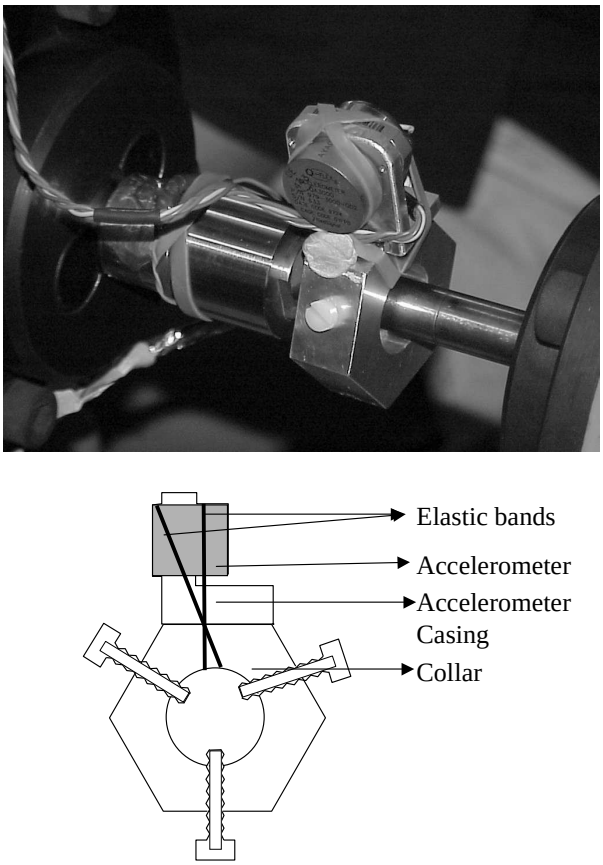

Figure 4.4: Torque tube (left), accelerometer on sample (right). Accelerometer with collar schematic (below).

digital (A/D) converter was constructed (Figure 4.7).

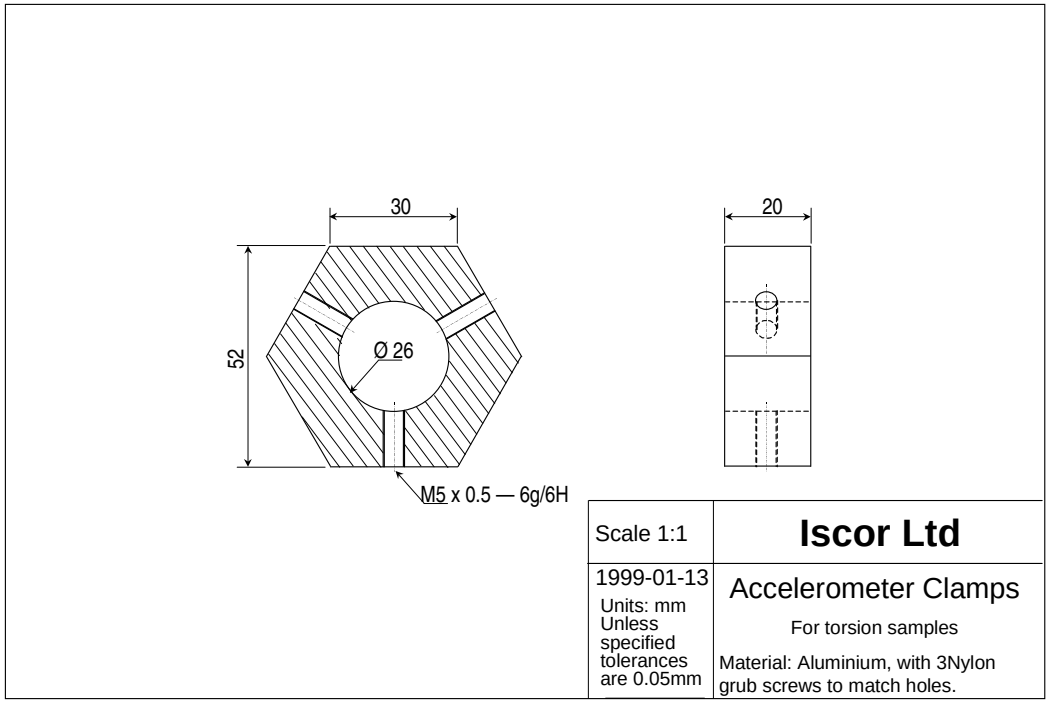

Figure 4.5: Manufacturing drawing of the collar for accelerometer.

Figure 4.6: Signal conditioning (top) and power supply (bottom) for accelerometer.

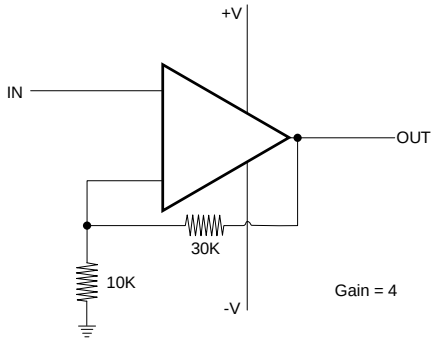

Figure 4.7: Circuit diagram of gain board for accelerometer signal amplification for input into the A/D converter.

4.5 Design of the torque measurement system

The torque measuring system was designed as a separate piece of tube between one of the grips and the sample. It is therefore 'in series' with the sample and will affect the torque measurement.

The requirements for a torque measuring system were:

1. It must be able to measure to the required *sensitivity*.
2. The torque tube must not reduce the *stiffness* of the system by more than a prescribed amount.
3. It must be able to measure the largest expected torque in the range with repeatability and without *yielding or buckling*.
4. *Practical considerations:* The system must not be inconveniently large or small.
5. *Torque tube grips:* The system must be attached to the Avery and sample.
6. *Signal conditioning and amplification* must considered.

The starting point will be the consideration of an ideal design that maximizes stiffness and sensitivity, where only the first two requirements are of importance. Secondly, the mechanical strength requirements (3) will be introduced and finally the peripheral requirements (4-6) will be considered.

4.5.1 Sensitivity

Sensitivity can be defined as the number of measurable units of output (Signal) per unit torque (T), where torque is denoted as T. In strain gauging the output can be measured with a voltmeter. The signal will be proportional to V_{out}:

$$\begin{aligned} \text{Sensitivity} &= \frac{\text{Signal}}{T} \\ &= \frac{V_{out}}{T}, \end{aligned} \tag{4.15}$$

the limits of the sensitivity (the voltmeter) are to be considered later.

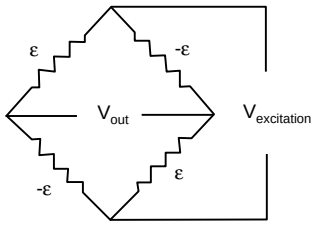

Figure 4.8: Wheatstone bridge arrangement of strain gauges on a torsional element.

When strain gauges are connected in a Wheatstone bridge arrangement as in Figure 4.8, the measured voltage (V_{out}) is proportional to the strain gauge factor (k), the strain (ϵ) experienced by the strain gauges on the surface of the torque tube and the excitation voltage ($V_{excitation}$) over the strain gauges in the bridge:

$$V_{out} = V_{excitation}\epsilon k. \tag{4.16}$$

All designs use a full (i.e. four active strain gauges as shown in Figure 4.8) Wheatstone bridge arrangement or combinations thereof. The previous equation was derived in Appendix B.3.1 [71, page 225].

Using the theories of mechanics of solids [68, pages 133-136,145] the surface strain at 45°to the axis of a hollow cylinder (ϵ_{45^o}), can be related to the torsional strain (γ) as follows:

$$\begin{aligned} \epsilon_{45^o} &= \frac{\gamma}{2} \\ &= \frac{\tau}{2G} \\ &= \frac{Tr_o}{2GI_p} \\ &= \frac{Tr_o}{\pi G(r_o^4 - r_i^4)}, \end{aligned} \tag{4.17}$$

where τ is the torsional stress, G is the modulus of rigidity, I_p is the polar moment of inertia, r_o, r_i are the outer and inner radii respectively.

The analysis will show that the well-designed torque tube is a thin-walled short cylinder, with thickness t, and mean radius r. Assuming a thin-walled cylinder, with thickness t, then:

$$\epsilon_{45^o} = \frac{T}{4\pi G r^2 t}. \tag{4.18}$$

To ensure that the design is limited to a thin-walled approximation, the following limit is applied (derived in Appendix B.3.2, page 152):

$$t \leq \left(\frac{4f_{approx}}{1-f_{approx}}\right)^{\frac{1}{2}} r. \tag{4.19}$$

Where f_{approx} is the fractional inaccuracy in the thin-walled approximationwhich, for the present set up will be shown to be $f_{approx} < 0.05$ for $t > 0.46r$.

While dedicated strain gauge amplifiers and measuring systems will be used, a standard voltmeter can be used for a substitute in the argument that follows. The information on the data sheets [72] of a standard voltmeter states that very little is gained by changing voltage ranges, although some advantage would be gained by using the full scale range. This suggests increasing the number of strain gauges if the voltmeter scale range is not filled, but not otherwise. This idea will be explored in the Appendix B.3.4, page 157. However, for consistency in the equations let n be the number of full Wheatstone bridges in the strain gauge system, so that when $n = 1$ there are 4 gauges, $n = 2$ there are 8 gauges and so on. In this section, n will always be one, since a practical design including cost considerations is required. The analysis with variable n is considerably more complicated.

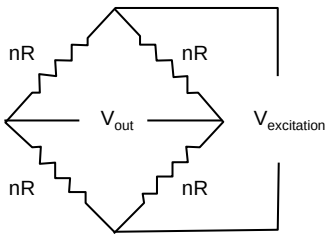

Figure 4.9: Wheatstone bridge arrangement of 4n strain gauges.

The voltage V_{gauge} across one gauge of resistance R in a multiple gauge Wheatstone bridge (as in Figure 4.9) can be written as:

$$V_{gauge} = \frac{V_{exitation}}{2n}. \tag{4.20}$$

The power dissipated in each gauge, P_{gauge} is thus

$$\begin{aligned} P_{gauge} &= \frac{V_{gauge}^2}{R} \\ &= \frac{V_{exitation}^2}{4n^2R}. \end{aligned} \tag{4.21}$$

There is a limit on the power dissipated per unit area, P', for any strain gauge system. This is related to the power dissipated in each gauge and each gauge area, A_{gauge}

$$P' = \frac{P_{gauge}}{A_{gauge}}, \tag{4.22}$$

or

$$P' = \frac{V_{exitation}^2}{4n^2 R A_{gauge}}, \tag{4.23}$$

so that

$$V_{excitation} = 2n(RP'A_{gauge})^{\frac{1}{2}}. \tag{4.24}$$

Substituting Equations 4.16, 4.18 and 4.24 into Equation 4.15, the sensitivity becomes

$$\text{Sensitivity} = \frac{nk\,(RP'A_{gauge})^{\frac{1}{2}}}{2\pi G r^2 t}. \tag{4.25}$$

It is evident from Equation 4.25 that the signal is proportional the number of gauges. The Johnson noise, V_{noise}, in the system is related to the resistance in the system as follows [73]:

$$V_{noise} = (4\kappa \mathrm{T} R \Delta f)^{\frac{1}{2}}, \tag{4.26}$$

where T is the temperature, κ is Boltzmann's constant and Δf is the bandwidth. This equation shows that the noise is proportional to the square root of the resistance and thus the square root of the number of gauges. Thus, increasing the number of gauges will improve the signal to noise ratio. This idea is expanded in Appendix B.3.4, page 157.

4.5.2 Stiffness

While most torque load cell designs, [74], [75] are designed for maximising sensitivity, there are few designed for low compliance. A high *torsional stiffness* or low compliance is important to ensure that both upper and lower yield points are measured. In a torsion test, the parts of the test equipment (including the torque tube) that deform when the torque is applied, will be defined as the machine. During this present investigation (steel torsion test), just after the upper yield point, the stress that the sample can withstand drops significantly and rapidly while the sample strain, and thus sample twist, hardly change. At this point, the sample becomes

suddenly plastic. If the machine has a similar elastic torsional strain as the sample (as in the case of a soft machine), the machine will reload the sample; this will mask the yield point, as seen in Figure 4.10.

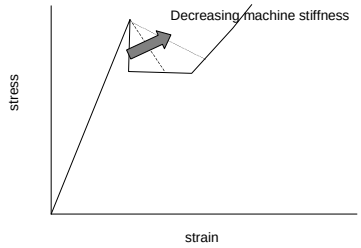

Figure 4.10: The effect of decreasing machine stiffness on the yield point in steel.

The following analysis is adapted from the axial load case [76]. It is much simpler than the axial case. Two situations are considered, one situation (1) is just before the upper yield point and the other situation (2) is just after upper yield point.

In torsion, the total system twist (ϕ_{system}) is the sum of the elastic twist of the sample ($\phi_{elastic}$), the plastic twist of the sample ($\phi_{plastic}$) and elastic twist of the machine ($\phi_{machine}$):

$$\phi_{system} = \phi_{machine} + \phi_{elastic} + \phi_{plastic}. \tag{4.27}$$

If it is considered that the machine is a torsional spring with spring constant $K_{machine}$ and torque T, then twist can be expressed as follows:

$$\phi_{machine} = \frac{T}{K_{machine}}. \tag{4.28}$$

The elastic twist of the sample can also be expressed in terms of torque, polar moment of inertia of the sample, the sample length and the sample's modulus of rigidity (T, I_p, L, G):

$$\phi_{elastic} = \frac{TL}{I_pG}. \tag{4.29}$$

Substituting Equations 4.28 and 4.29 into 4.27 gives:

$$\phi_{system} = \frac{T}{K_{machine}} + \frac{TL}{I_pG} + \phi_{plastic}. \tag{4.30}$$

Before yield (in situation 1), the Equation 4.27 is as follows:

$$\phi_{system\ 1} = \frac{T}{K_{machine}} + \frac{TL}{I_pG}. \tag{4.31}$$

Just after yield (in situation 2), the sample twists a little more by $\phi_{plastic}$ and the torque drops, so that T becomes $T+dT$ (where $dT < 0$) and Equation 4.27 becomes:

$$\phi_{system\ 2} = \frac{T+dT}{K_{machine}} + \frac{(T+dT)L}{I_pG} + \phi_{plastic}. \tag{4.32}$$

It is assumed that the twist in the system before yield and the twist in the system just after yield (situations 1,2) are equal:

$$\phi_{system\ 1} = \phi_{system\ 2}, \tag{4.33}$$

so that

$$\begin{aligned} \frac{T}{K_{machine}} + \frac{TL}{I_pG} &= \frac{T+dT}{K_{machine}} + \frac{(T+dT)L}{I_pG} + \phi_{plastic} \\ dT &= \frac{\phi_{plastic}}{\frac{1}{K_{machine}} + \frac{L}{GI_p}}. \end{aligned} \tag{4.34}$$

Both the sample parameters and the machine parameters are important in ensuring a visible yield drop. The experiment aims to determine the properties of the sample, and this requires that the measured dT should be as large as possible. The combined stiffness of the machine and sample must be large.

Torsional stiffness of the torque tube can be defined as the torque per unit twist (ϕ). Assuming that the torque tube is a thin-walled cylinder, this can be written as follows [68]:

$$\begin{aligned} \text{Stiffness} &= \frac{T}{\phi} \\ &= \frac{GI_p}{l} \\ &= \frac{2\pi Gr^3t}{l}, \end{aligned} \tag{4.35}$$

where l is the torque tube length. A design will be considered where one set of gauges is used (n=1, a single Wheatstone bridge). The other case, namely 'n max', where the gauges cover the area of the torque tube can be found in Appendix B.3.4, page 157.

Combined Stiffness and sensitivity criteria for an ideal design

In considering the design with a single Wheatstone bridge set of gauges, Equations 4.16, 4.24 (with $n = 1$) and 4.18 can be substituted into 4.15, so that the sensitivity becomes:

$$\text{Sensitivity} = \frac{k(RP'A_{gauge})^{\frac{1}{2}}}{2\pi Gr^2t}, \tag{4.36}$$

with the constraint that:

$$t \leq \left(\frac{4f_{approx}}{1-f_{approx}}\right)^{\frac{1}{2}} r, \tag{4.37}$$

from Equation 4.19.

The stiffness limit is from Equation 4.35 is:

$$\text{Stiffness} = \frac{2\pi G r^3 t}{l}, \tag{4.38}$$

so that

$$\text{Stiffness} \propto \frac{G r^3 t}{l}. \tag{4.39}$$

To maximize sensitivity (from Equation 4.36) consider:

$$\text{Sensitivity} \propto \frac{1}{G r^2 t},$$

let

$$y = \frac{1}{G r^2 t}, \tag{4.40}$$

and substitute this into Equation 4.40:

$$\text{Sensitivity} \propto y \tag{4.41}$$

and Equation 4.39:

$$\text{Stiffness} \propto \frac{r}{yl}. \tag{4.42}$$

It follows that sensitivity can be increased without limit by increasing y and one can increase stiffness without limit by increasing r or decreasing l at constant y. The 'ideal' design shape in this case would be a ring of ribbon.

It needs to be pointed out that decreasing modulus, G, will usually lead to a material choice with lower torsional yield, and it is necessary to consider mechanical strength and stability requirements.

In practice, it is possible to decide on the minimum acceptable stiffness and sensitivity and thereby obtain the minimum radius. Referring to Equation 4.36, if the sensitivity is defined to be at least a certain level, say S_0, then,

$$S_0 \leq \frac{k(RP'A_{gauge})^{\frac{1}{2}}}{2\pi G r^2 t} \tag{4.43}$$

and referring to Equation 4.35, if the stiffness is required to be greater than or equal to Σ_0:

$$\Sigma_0 \geq \frac{2\pi G r^3 t}{l}, \tag{4.44}$$

l can be considered as a constant since l only appears in the stiffness equation (4.44) and it is clear that a minimum l equal to the length of one strain gauge can be used. Keeping l constant, Equations 4.43 and 4.44 can be plotted as in Figure 4.11.

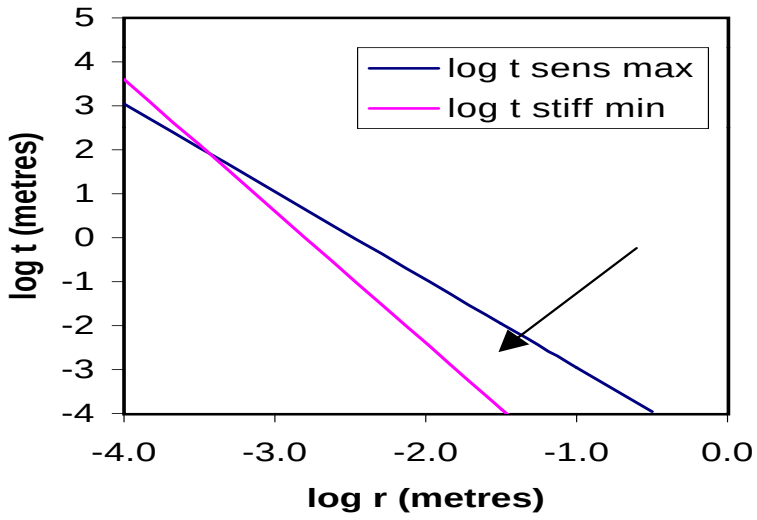

Figure 4.11: Sensitivity and Stiffness functions for one Wheatstone bridge set of gauges, where the arrow indicates the area that meets both requirements.

4.5.3 Mechanical strength requirements for one Wheatstone bridge arrangement

The mechanical limits on the design are that the yield stress and buckling torque of the design are not exceeded.

Considering the yield stress limit, the maximum torque, T_{max}, that the tube can withstand can be written as:

$$T_{max} \leq 2\tau_y \pi r^2 t,$$

which requires that :

$$r^2 t \geq \frac{T_{max}}{2\pi\tau_{yield}}. \tag{4.45}$$

For the buckling limit, a study of buckling by Timoshenko and Gere [77, page 500] can be referred to. The buckling criterion of a short tube is:

$$T_{\substack{crit,\\short}} \leq 8.78\frac{\pi E t^3 r^2}{(1-\nu^2)l^2}\left(1+0.0257(1-\nu^2)^{\frac{3}{4}}\left(\frac{l}{r^{\frac{1}{2}}t^{\frac{1}{2}}}\right)^3\right)^{\frac{1}{2}}, \qquad (4.46)$$

where E is the Young's modulus and ν is Poisson's ratio. The definition of a short tube is:

$$\frac{l^2 t}{((1-\nu^2)^{\frac{1}{2}}2^3 r^3)^{\frac{1}{2}}} < 5.5\ .$$

This assumption (that the torque tube is a short tube) will be verified later in this section.

A factor of safety needs to be included in the design. This is usually applied to the principal stresses on the mechanical member [70, p 10]. In pure torsion, this would be the shear stress and from a study of Equation 4.45, the safety factor would be applied to the maximum torque, and denoted as s.

The mechanical strength equations can be written as follows

$$r^2 t \geq \frac{T_{max} s}{2\pi\tau_y}, \qquad (4.47)$$

$$T_{\substack{crit,\ s\\short}} \leq 8.78\frac{\pi E t^3 r^2}{(1-\nu^2)l^2}\left(1+0.0257(1-\nu^2)^{\frac{3}{4}}\left(\frac{l}{r^{\frac{1}{2}}t^{\frac{1}{2}}}\right)^3\right)^{\frac{1}{2}}. \qquad (4.48)$$

Graphical representation for the sensitivity, stiffness, yield and buckling considerations (n=1)

Before these equations can be plotted, the minimum prescribed stiffness and sensitivity values must be determined. To obtain a minimum acceptable sensitivity, a torsional stress-strain curve for the material must be studied and a stress resolution decided on. Figure 4.1, page 62, illustrates qualitatively what, in principle, would be required.

In this study, the most important (interesting) area in the stress strain curve is after the upper yield point, at the stress drop. The drop must be resolved and five observations would be sufficient to resolve this. During design, tests had yet to be performed, thus work from other authors must be referred to, to determine the value

of the stress drop. A convenient reference is Elliot *et al.*'s work [3] where a stress drop of around 2500psi is experienced during sample yield.

$$\begin{aligned} \text{Required Stress resolution} &= \frac{\Delta\tau}{\text{number of observations}} \\ &= \frac{2500\text{psi}}{5} \\ &= 3.45\text{MPa}, \end{aligned} \tag{4.49}$$

which, when taking into consideration the sample dimensions (Figure 4.3), corresponds to a torque resolution of:

$$\begin{aligned} \text{Torque resolution} &= \frac{\Delta T}{\text{number of observations}} \\ &= \frac{\pi\Delta\tau(R_{outer}^4 - R_{inner}^4)}{2R_{outer}\text{ number of observations}} \\ &= \frac{\pi 0.69\times 10^9((8.0\times 10^{-3})^4 - (6.5\times 10^{-3})^4)}{2\cdot 8.0\times 10^{-3}} \\ &= 1.57\text{Nm/point}. \end{aligned} \tag{4.50}$$

An Agilent 3441 A multimeter can discern 0.0001mV in the 100mV range (lowest range). The accuracy is 0.003% of reading + 0.003% of range so that the measurement is accurate to 0.006mV. Thus, the minimum system sensitivity required:

$$S_o = \frac{V_{out}/\text{number observations}}{T/\text{number observations}} \tag{4.51}$$

$$= \frac{6\times 10^{-6}}{1.57} \tag{4.52}$$

$$= 3.8\times 10^{-6} V/Nm. \tag{4.53}$$

This equation is used with the assumption that the strain gauge system only experiences thermal and shot noise [73], although such a system does not exist. Appendix B.3.3, page 153, is a fuller discussion of both the fundamental limiting factors and the practical limitations that a strain gauge experiences. Only an attempt to keep the extrinsic or reducible noise to a minimum can be made, since it cannot be calculated in the design.

For the stiffness limit, Figure 4.1 may be referred to; in the ideal system (infinitely stiff) the stress drop would be vertical. It is known that the machine must have a much greater stiffness than the sample in order to observe a sharp yield drop. The design will be based on the requirement that the stiffness of the torque tube should

be at least 10 times greater than that of the sample. The sample stiffness is:

$$\begin{aligned} \text{Sample Stiffness} &= \frac{G\pi(R_{outer}^4 - R_{inner}^4)}{2L} \\ &= \frac{81 \times 10^9 \ \pi((8 \times 10^{-3})^4 - (6.5 \times 10^{-3})^4)}{2 \cdot 50 \times 10^{-3}} \\ &= 5800\text{Nm/rad.} \end{aligned} \tag{4.54}$$

Thus $\Sigma_0 = 58000$Nm/rad.

The material constants for aluminum and steel[68] can be found in Table 4.5. Since

Table 4.5: Material constants for steel and aluminium [68].

Property	Aluminium alloy, 7075-T6	x50 High strength steel
Shear modulus, G, GPa	26	80
Young's modulus, E, MPa	70	210
Yield shear, τ, MPa	135	500
Poisson's ratio	0.33	0.3

the failure of the design will not result in injury, (although the cost of failure is obviously significant to the experimenters) the safety factor, s, will be taken as 2.

The constants associated with the strain gauge may now be considered. The dimensions of the strain gauge are illustrated in Figure 4.12.

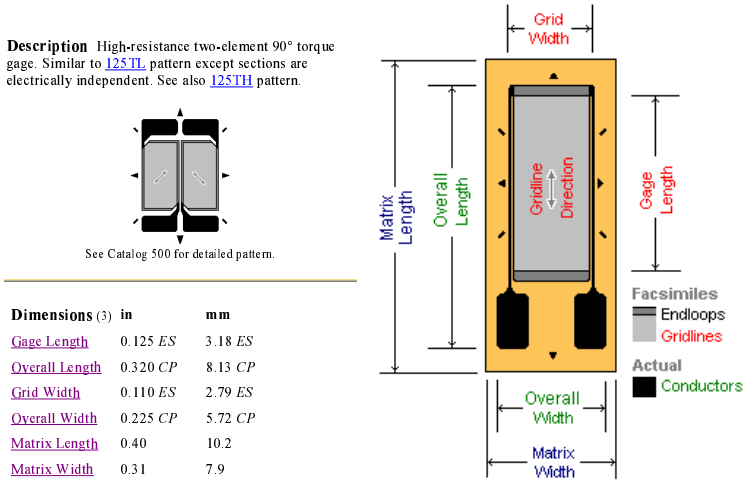

Figure 4.12: Dimensions of standard type strain gauge [78].

The electrical current passing through the gauge heats the gauge, and this can

result in errors of instability, drift and ultimately, gauge burnout [71]. Table 4.6

Table 4.6: Table of permissible heat dissipation values for various substrate materials [71] (kW/m^2).

Excellent dissipation Heavy (thick) copper or aluminium	Good dissipation Thick steel	Fair dissipation Thin stainless steel or titanium
3.1–7.8	1.6–3.1	0.78–1.6

gives values of heat dissipation for an isolated gauge. The main heat sink of the gauge is the material, so the heat dissipation in gauges is strongly related to the material that the gauge is attached to.

Using the same axes as for the sensitivity and stiffness inequalities, (Figure 4.11) all five inequalities can be plotted on one graph.

Sensitivity, from Equation 4.43 is a line of maximum allowable $\log(t)$

$$\log(t) \quad \leq \quad -2\log(r) + \log\left(\frac{k(RP'A_{gauge})^{\frac{1}{2}}}{2\pi G S_0}\right). \tag{4.55}$$

The thin-tube limit from Equation 4.19 is a line of maximum allowable $\log(t)$:

$$\log(t) \quad \leq \quad \log(r) + \frac{1}{2}\log\left(\frac{4f_{approx}}{1-f_{approx}}\right). \tag{4.56}$$

Stiffness from Equation 4.44 is a line of minimum allowable $\log(t)$:

$$\log(t) \quad \geq \quad -3\log(r) + \log\left(\frac{\Sigma_0 l}{2\pi G}\right). \tag{4.57}$$

Maximum torque, from Equation 4.47 is line of minimum $\log(t)$:

$$\log(t) \quad \geq \quad -2\log(r) + \log\left(\frac{T_{max}s}{2\pi\tau_y}\right). \tag{4.58}$$

Buckling, from Equation 4.48, is a line of minimum $\log(t)$. Since it is an implicit inequality, a numerical solution was found for each $\log(t)$ using chosen values of $\log(r)$, using the following equation:

$$8.78\frac{\pi E t^3 r^2}{T_{\substack{crit,\\ short}}\, s(1-\nu^2)l^2}\left(1 + 0.0257(1-\nu^2)^{\frac{3}{4}}\left(\frac{l}{\sqrt{rt}}\right)^3\right)^{\frac{1}{2}} \quad = \quad 1. \tag{4.59}$$

When l is set, the criteria can be plotted as in Figure 4.13.

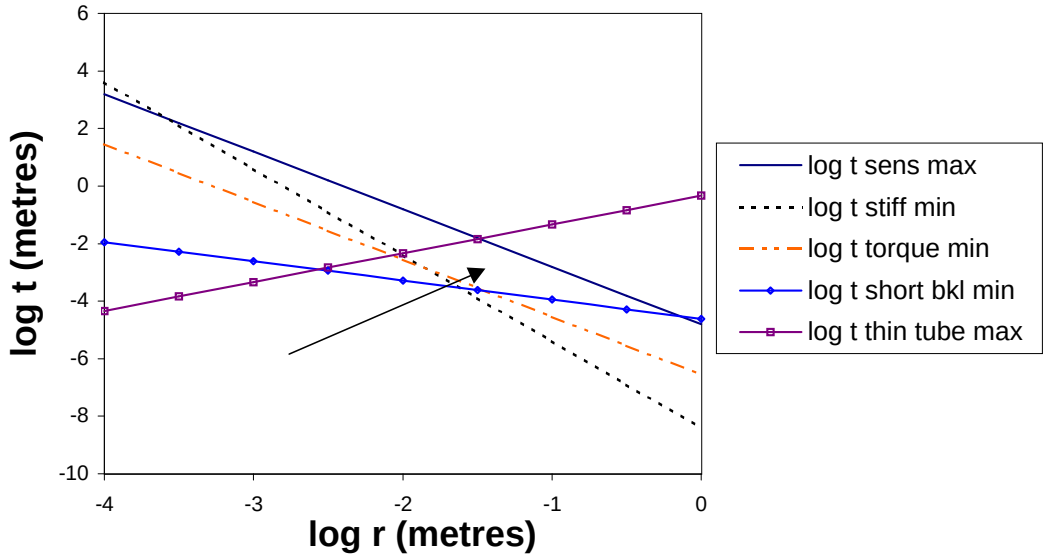

Figure 4.13: Buckling, torque contours and thin tube limit with stiffness and sensitivity criteria for $n = 1$. The arrow indicates the permissable region.

4.5.4 Practical considerations for system with one Wheatstone bridge arrangement

The fatigue life of the strain gauge must not be exceeded. The surface strain in torsion must not exceed the critical surface strain, ϵ_f, where:

$$\begin{aligned} \epsilon_f &\geq \epsilon \\ &\geq \frac{T}{4\pi G r^2 t}. \end{aligned} \tag{4.60}$$

From the graph in Figure 4.14, for a fatigue life of 10^3 cycles, a maximum alternating linear surface strain of 0.0018 ϵ_f is allowed before a measurable zero shift in the gauge occurs. Unsurprisingly, the condition has the same form as the mechanical failure criterion, although it is more severe.

A second practical limit on the design is the smallest thickness, t_m achievable in normal machining.

$$t \geq t_m. \tag{4.61}$$

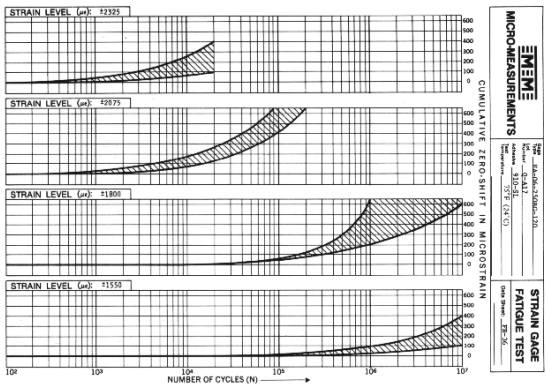

Figure 4.14: Fatigue life for standard type strain gauge [78].

Different machining shops have different opinions on what this limit is; these are summarised in Table 4.7. The Iscor value was taken since the machining would be done there.

Table 4.7: Table of minimum machining thickness.

Machine shop	t_m for aluminium	t_m for steel
CSIR [79]	0.5mm	0.5mm
Iscor [80]	1mm	1.5mm

The length of the tube should not be shorter than the length of a strain gauge, l_{gauge}.

$$l \quad \geq \quad l_{gauge}. \tag{4.62}$$

Referring to Figure 4.12 it is seen that $l_{gauge} = 10.2$mm.

The graphical representation of this may be seen in Figure 4.15.

It was found that short-tube buckling was valid for the most part of the plotted values, but in the area where the short tube assumption (Equation 4.47) did not hold, it was found that the long tube buckling equation gave a less stringent limit, and thus had no effect on the limits.

For completeness, the long-tube buckling equation is as follows:

$$t^{\frac{3}{2}} \quad = \quad \frac{3T_{max}s(1-\nu^2)^{\frac{3}{4}}}{\sqrt{2r}\ \pi E}. \tag{4.63}$$

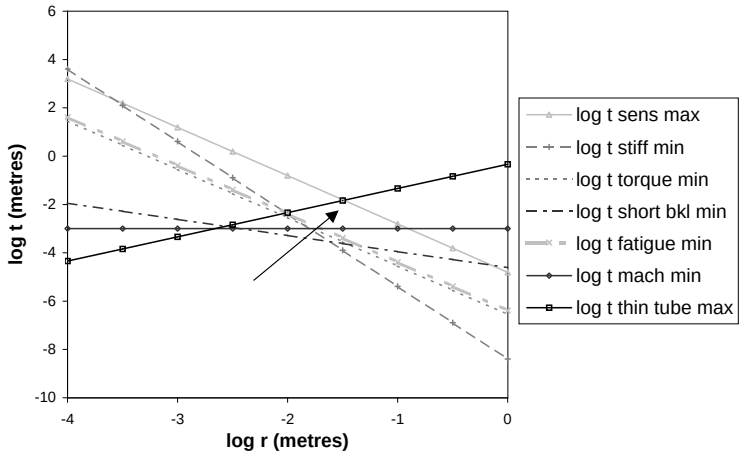

Figure 4.15: All inequalities for design with a single Wheatstone bridge set of gauges (n=1). The arrow indicates the permissable region.

A design that maintains high stiffness and sensitivity would be on a line that is equidistant from the stiffness and sensitivity lines in Figure 4.15. When practical convenience with fingers is considered, the largest radius that still achieves the sensitivity and machining criteria should be chosen. This gives $r = 15.6$mm, $t = 1$mm, while $l = 11.4$mm for a design in steel.

4.5.5 Design of torque tube grips

The connection between the measuring member and the rest of the system must be designed. On the left hand side of Figure 4.16, the sample must slip into the torque tube grip.

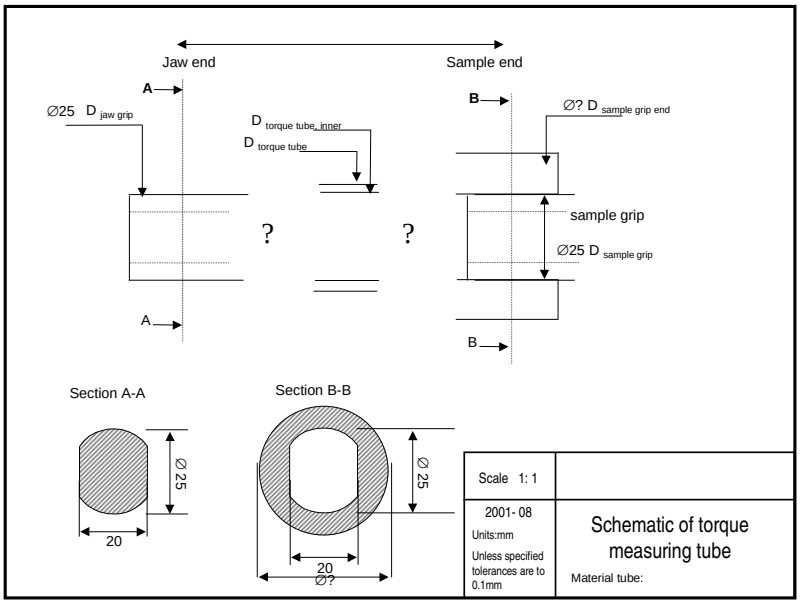

Figure 4.16: Schematic diagram of torque tube with grips.

The following considerations need to be taken into account in the design:

1. Effect of contact stresses on the torque tube grips,
2. Manufacturing route of the measuring member, and
3. Strength of the connections (fillet radii and tube thickness).

The tube will experience contact stresses where, under load, the edges of the steel sample twist against the torque tube grip, and where the torque tube fits into the Avery grip. If the aluminium design is used during each test the sample would deform the grip ('bite into') and conceivably after a few samples the samples would be difficult to insert into the grip. This limits the torque tube design to the use of steel in the design, where the steel has been reasonably hardened.

The most convenient method of manufacture would be drilling and spark eroding the inner diameter, as seen in Figure 4.17. Therefore, it would be advisable to make

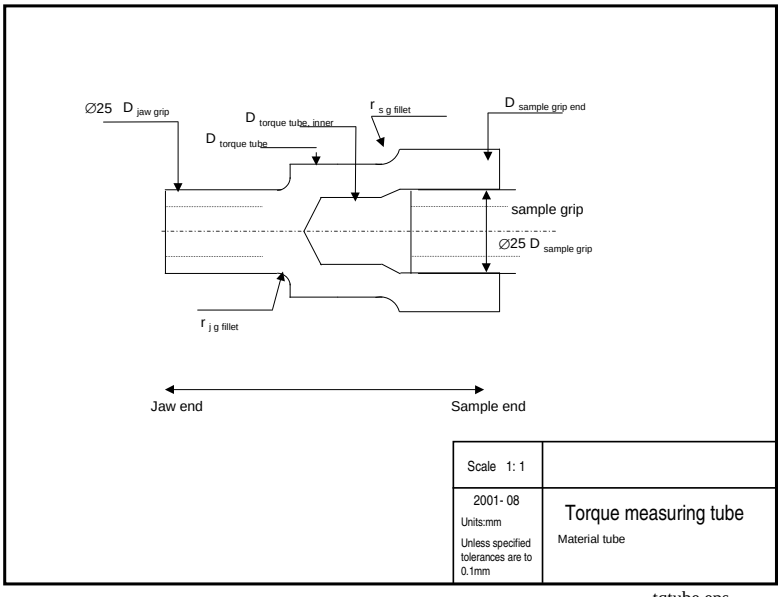

Figure 4.17: Design of bar with connectors.

the inner diameter compatible with the grip (on the right hand side of Figure 4.17). Thus, the inner diameter is altered to 20mm. The design is to remain comfortably within the allowable design in Figure 4.15. The new dimensions are $l = 12.8$mm, $t = 6$mm and $r = 13$mm.

Consideration of the strength of the connections must now be performed. Unfortunately the connectors will affect the stiffness, but including these in the stiffness optimization would have been horrendously expensive. The design must be of high stiffness. The following points must be considered:

1. Minimum diameter of the sample grip end ($D_{sample\ grip\ end}$) that will resist yielding, and the diameter that does not reduce the stiffness excessively,
2. Strength of the jaw grip end ($D_{jaw\ grip}$),
3. Fillet radii.

Design of sample grip end diameter

Considering the shear on the sample grip end:

$$\tau_y \geq \frac{TsD_{sample\ grip\ end}}{2I_p}, \tag{4.64}$$

where I_p is given by

$$I_p = \pi\left(\frac{D^4_{sample\ grip\ end}}{32} - \frac{D^4_{sample\ grip}}{32}\right). \quad (4.65)$$

Solving for $D_{sample\ grip\ end}$, it is found that $D_{sample\ grip\ end} \geq 31$mm. The required stiffness of this part is similar to that required by the torque tube, so from Equation 4.35,

$$\text{Stiffness} = \frac{GI_p}{l_{sample\ grip\ end}}, \quad (4.66)$$

where $l_{sample\ grip\ end}$ is the length of the tube at the sample grip end. Thus, solving for $D_{sample\ grip\ end}$, setting the stiffness to that of the torque tube, it is found that when Stiffness $= 4.6 \times 10^5 Pam^3$, $l_{sample\ grip\ end} = 30mm$ and $G = 80.0 \times 10^9 Pa$, $D_{sample\ grip} = 32mm$, $D_{sample\ grip\ end} = 38$mm.

Design of fillets

It must also be ensured that the stress concentration due to the fillet does not cause the shear in the member to exceed yield shear.

$$K_{ts} \geq \frac{\tau_y}{\tau}, \quad (4.67)$$

K_{ts} is taken from Shigley[70, p676] in this case (Figure 4.18), and so:

$$\tau = \frac{K_{ts}TsD_{sample\ grip\ end}}{2I_p}. \quad (4.68)$$

The ratio of sample grip diameter to torque tube diameter, $d_{torque\ tube}$, is

$$\begin{aligned} \frac{D_{sample\ grip\ end}}{d_{torque\ tube}} &= \frac{38}{32} \\ &= 1.2. \end{aligned} \quad (4.69)$$

A low K_{ts} from the graph (say $K_{ts} = 1.2$) should be chosen to ensure that the stress concentration due to the fillet does not cause the shear in the member to exceed the yield shear, this corresponds to:

$$\frac{r_{fillet}}{d_{torque\ tube}} = 0.30. \quad (4.70)$$

So that:

$$r_{fillet} = 10mm. \quad (4.71)$$

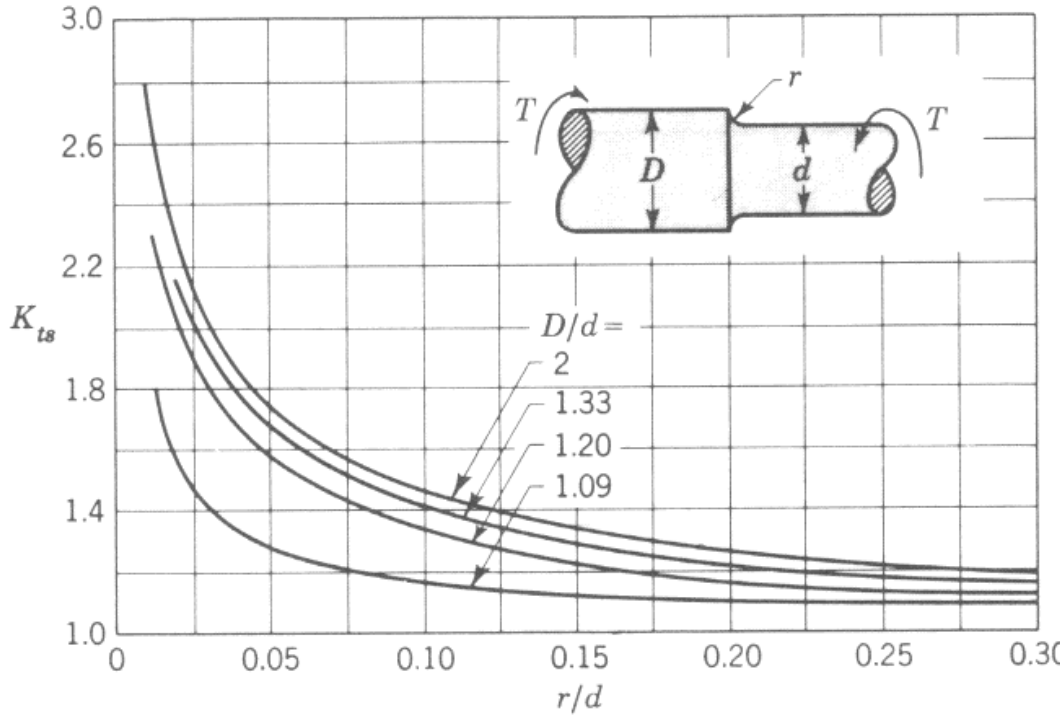

Figure 4.18: K_{ts} for fillets in torsion, from Shigley [70].

For the fillet, between the torque tube at the jaw grip

$$\begin{aligned} \frac{d_{torque\ tube}}{D_{jaw\ grip}} &= \frac{47}{25} \\ &= 1.6. \end{aligned} \tag{4.72}$$

A low K_{ts} must be chosen, ($K_{ts} = 1.2$ is minimum), and on the graph corresponds to

$$\frac{r_{fillet}}{D_{jaw\ grip}} = 0.30. \tag{4.73}$$

So that

$$r_{fillet} = 6mm. \tag{4.74}$$

The final design is shown in Figure 4.19.

The actual equipment is shown in Figure 4.20.

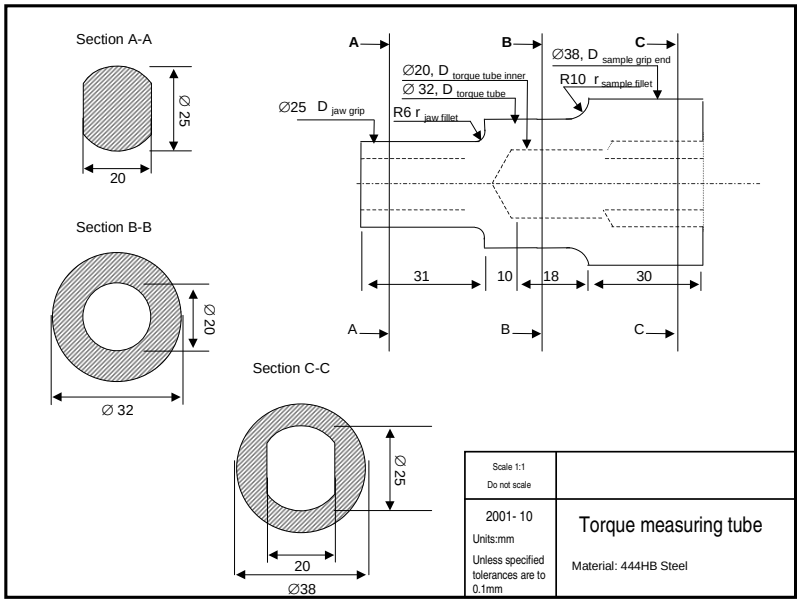

Figure 4.19: Manufacturing drawing of torque-measuring tube with connectors.

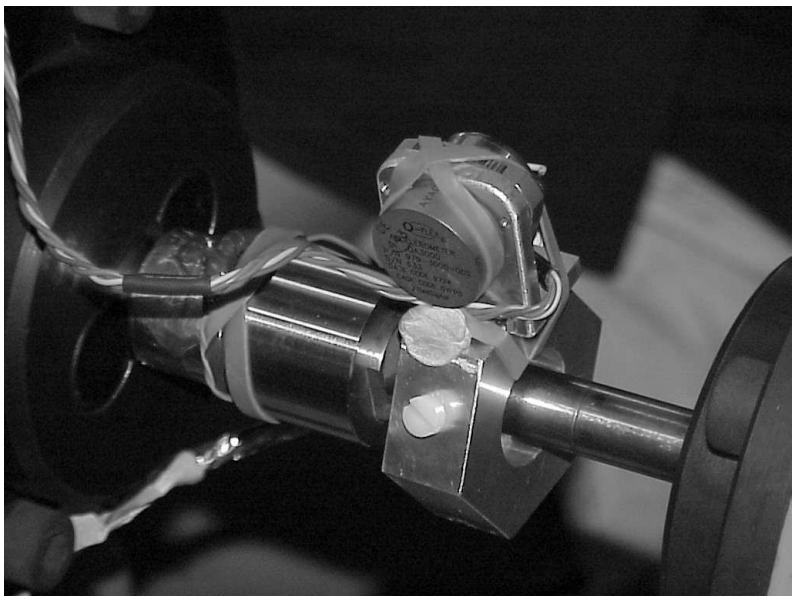

Figure 4.20: Torque tube (left), accelerometer on sample, right.

4.5.6 Strain gauge signal conditioning and amplification system (single Wheatstone bridge)

The strain gauges were connected in the conventional four gauge Wheatstone bridge or full-bridge arrangement (Figure 4.8) and were powered and the signal conditioned by a Hottinger Baldwin Messtechnik AB12 strain gauge amplifier system with a Messverstärker MCGMC305 card. The excitation voltage was 2.5V.

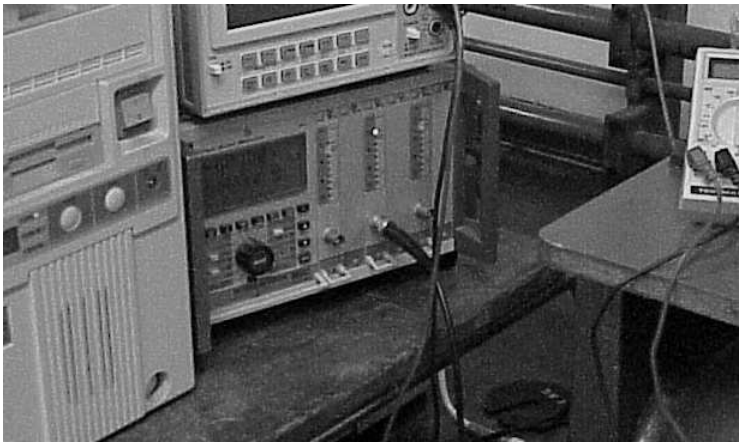

Figure 4.21: Strain gauge signal conditioner and power supply.

4.6 Summary of experimental system

1. Frame
   Avery torsion testing rig was used as the frame.

2. Sample

   (a) A 0.018wt%C steel with minimal carbides was chosen and stress relieved.

   (b) The sample design was a thin-walled tube with outer diameter 16mm, thickness 1.5mm, gauge length 50mm. There was a central groove (depth 0.16mm) and appropriately filleted shoulders to the sample grips.

3. Strain measurement system

   (a) An inertial accelerometer was used, attached to the sample with a collar and soft nylon grub screws.

   (b) The range is effectively infinite.

(c) The threshold strain resolution is potentially $1\mu e$.

(d) The power supply and signal conditioning was performed with circuitry designed for the accelerometer, while a simple gain board to amplify the signal to be suitable for input into the analog to digital (A/D) converter was constructed.

4. Stress measurement system

(a) A torque measurement system of outer diameter 32mm and thickness 6mm was designed.

(b) This design met the stiffness requirement of $> 5800Nm/rad$ and the strength requirement with a safety factor of 2.

(c) With a full-bridge arrangement on the torsional element, the sensitivity resolution of $> 3.8 \times 10^{-6}V/Nm$ was met.

(d) The practical considerations of fatigue life, grip design and grip fillet design were incorporated

(e) The Wheatstone bridge arrangement was powered and the signal conditioned by a Hottinger Baldwin Messtechnik AB12 strain gauge amplifier system with a Messverstärker MCGMC305 card.

Chapter 5

Experimental procedure

This chapter details the testing of the designed equipment and samples. This involves the calibration of torsional stress and strain measurement systems, sample treatment and the torsion test itself.

5.1 Calibration

5.1.1 Strain measurement system calibration

The calibration of the accelerometer was done by using a bubble type reference inclinometer from CSIR. The procedure involved tilting the accelerometer and inclinometer to various angles and correlating the signal from the accelerometer with the reference inclinometer. The signal from the accelerometer is known [81] to be well approximated by a third order polynomial. This calibration was done twice. The first calibration (in Figure C.1, Appendix C.1, page 169) was performed over a large range, and since far less twist was used in the testing of the samples the range was reduced for the second calibration (Figure 5.1). This was done by increasing the gain in the electronics. It also improved the precision error of the accelerometer system.

Uncertainty can be defined as an estimate of experimental error [82], or more rigourously, the bound or interval around the measurement in which the true value falls for a certain confidence level. The uncertainty for these calibrations was evaluated following Coleman and Steele [82, page 180] by taking the larger of the two

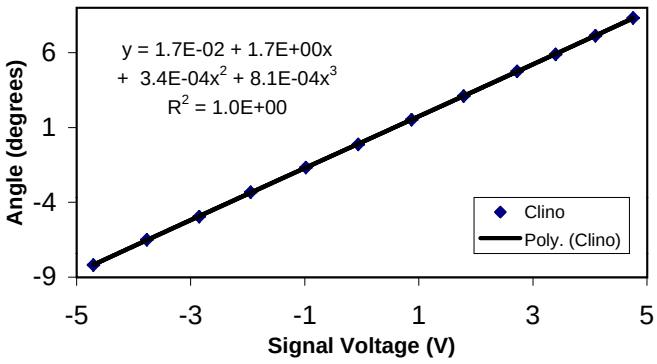

Figure 5.1: Second accelerometer calibration 2002-12-30. Inclinometer angle versus voltage on accelerometer. 'Poly (Clino)' is the 4th order polynomial regression fit of the 'Clino' points. X,Y abscissae swapped for convenience.

following uncertainties; the uncertainty associated with the measurement or 'reading' (where the uncertainty interval is related to the minimum measurable angle as determined by the minimum measurable voltage) and the uncertainty associated with the curve fitting. The 95% uncertainty from the curve fitting is considered to be twice the standard error of estimate of the polynomial (SEE) [82, page 173]. The technique for determining uncertainty associated with calibration that Coleman and Steele[82, page 173] recommend, makes use of the value standard error of estimate (SEE). This may be found from:

$$\text{SEE} \quad = \quad \left\{ \frac{\sum_{i=1}^{N} [y_i - (a_0 + a_1 x_i + a_2 x_i^2 + a_3 x_i^3)]}{N - 4} \right\}^{\frac{1}{2}} . \tag{5.1}$$

where y_i and x_i are each of the N calibration points, and $a_0,\ a_1,\ a_2,\ a_3$ are the coefficients calculated from the least squares polynomial. Note that the most convenient method of calculating this is to exchange the x and y abscissae in the calibration. More details may be found in Appendix C, page 169.

The uncertainty in the curve fit (2SEE) in the second calibrations is 0.050° which exceeds the uncertainty in the measurement (0.002mV corresponds to 0.017°), thus the uncertainty in the curve fit was used. More details may be found in Appendix C.3, Figure C.2, page 170.

5.1.2 Torque tube calibration

The calibration of the torque tube was achieved by applying a known torque to the torque measurement tube. A calibration bar was attached to the torque tube, while weights were applied at the ends of this at a measured distance. The friction from the pulley was assumed to be negligible. The technique is illustrated in Figures 5.2 and 5.2. The calculation of torque in the calibration the strain gauges is (Figure 5.2)

$$T = L_{cal} \cos\theta_{cal} M g, \tag{5.2}$$

where L_{cal} is the length of the calibration bar, θ_{cal} is the angle at which it is inclined and M is the mass of the weight pans and weights, g is the gravity constant and is assumed to be constant ($9.7860994 m/s^2$ as measured for Pretoria). The difficulties in the calibration is detailed in Appendix C.2, page 170).

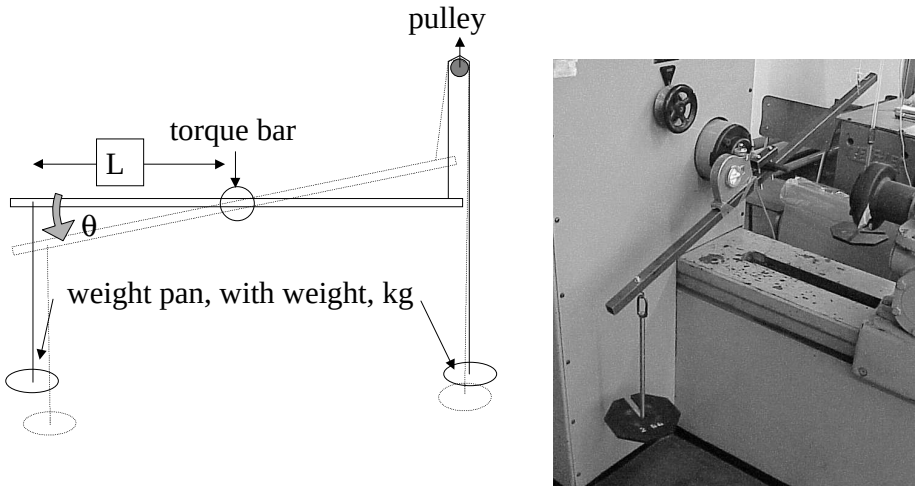

Figure 5.2: Schematic diagram of torque calibration and torque calibration equipment.

As before (Section 5.1.1), the larger of the two following uncertainties was taken; the uncertainty associated with the measurement or 'reading' and the uncertainty associated with the curve fitting. The uncertainty for these calibrations was evaluated using the value standard error of estimate (SEE). The errors in calibration are illustrated in Figure C.3 in Appendix C.3, page 171. However, the most convenient method of calculating this is to exchange the x and y abscissae in the calibration. This is done for convenience.

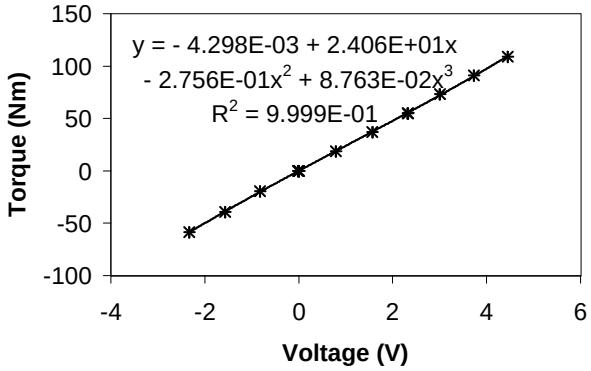

Figure 5.3: Torque calibration. X,Y abscissae exchanged for convenience.

Differentiating Equation 5.2, according to Equation C.3 in Appendix C.4 page 171 [82], results in the uncertainty in T, $\Delta T = 1.14$Nm. If the yield values show greater deviations than this, then they can be considered significantly different and reasons for the difference should be sought.

5.1.3 Summary of system

From the previous calculations, the system can measure down to an angle of 0.05° with 95% certainty and torque down to 1.14Nm to with 95% certainty. The torsional stress and strain from system would then be, from Equation 4.14,

$$\gamma = \frac{R_{outer}\phi}{L} \tag{5.3}$$

and

$$\tau = \frac{TR_{outer}}{I_{P\ sample}}. \tag{5.4}$$

5.2 Sample composition and heat treatment

The steel composition may be found in Table 5.1. The first samples (A6.1, A7.2, B5.1, C7.2, C3.2, An1, A21), only used for testing the equipment, were merely stress relieved according to Section 4.3.1, page 64 (700 °C for 2 hours, with furnace cooling to 500°C after which the samples were removed from the furnace and air cooled). Sample A41 was subjected to a full austenitising treatment, according to Section 2.5.1, page 42 (rapid heat to 915°C, 5 minutes at 915°C, furnace cool to 700°C, air cool from 700°C). All ageing of samples was done at 97°C for an hour.

Table 5.1: Composition of sample material.

Element	mass%	Element	mass%	Element	mass%	Element	mass%
C	0.018	Ni	0.010	Al	0.031	Zr	0.001
Mn	0.24	Cu	0.008	Ti	0.001	W	0.009
P	0.009	Cr	0.017	Nb	0.003	Co	<0.001
S	0.007	Mo	<0.001	B	0.0001	N	0.0025
Si	0.006	V	0.001	Sn	<0.001	Fe	balance

5.3 The torsion test

5.3.1 Strain rate

The strain rate was controlled by hand as the motor strain rates were far greater (3.5-90°/min) than those required in the current type of experiments. Elliot *et al.* [3] does not report strain rate but uses Deak's setup [28, page 36] and presumably his strain rate. Deak twisted the sample 0.02° every 30 sec, this corresponds to a torsional strain rate, $\dot{\gamma}$, of

$$\begin{aligned} \dot{\gamma} &= \frac{\phi R_{outer}}{Lt} \\ \dot{\gamma} &= \frac{0.02 \cdot \pi \cdot 0.812in}{2 \cdot 180 \cdot 0.787in \cdot 30s} \\ \dot{\gamma} &= 6 \times 10^{-6} s^{-1}. \end{aligned} \tag{5.5}$$

5.3.2 Peripheral equipment

To record the signals from the inclinometer and strain gauges, a Casey 486 computer with a PC30D analog-to-digital converter board, and Wave View for Dos 1.26 software was used. The signals were sampled at 4 Hz in burst mode in the range -5 to +5 volts. The equipment is shown in Figure 5.4. Analysis was performed on a Pentium 2 computer using Microsoft Excel.

Figure 5.4: 486 Computer with wave view software and PC30D board.

5.3.3 Procedure of the torsion tests

Samples of 0.018%C-0.24%Mn0.031%Al steel (full analysis in Table 5.1) were machined and stress relieved (excepting sample A41 which was austenitised).

The accelerometer collar was screwed with nylon screws onto the sample, the sample was connected to the torque tube and the torque tube was lined up and inserted into the chuck on the worm gear side of the machine (see Figure 4.4). The samples were strained at a rate of $5.6\times10^{-6}\ s^{-1}$ to a maximum strain of 3%, while the torque and twist values were sampled at 4Hz and recorded by computer.

The system performance was checked by straining samples in two tests as seen in Figure 5.5. This was a test procedure that imitates the previous research of Elliot *et al.*[3].All samples were tested in both forward and the reverse directions. The ageing of samples was done at 97°C for an hour.

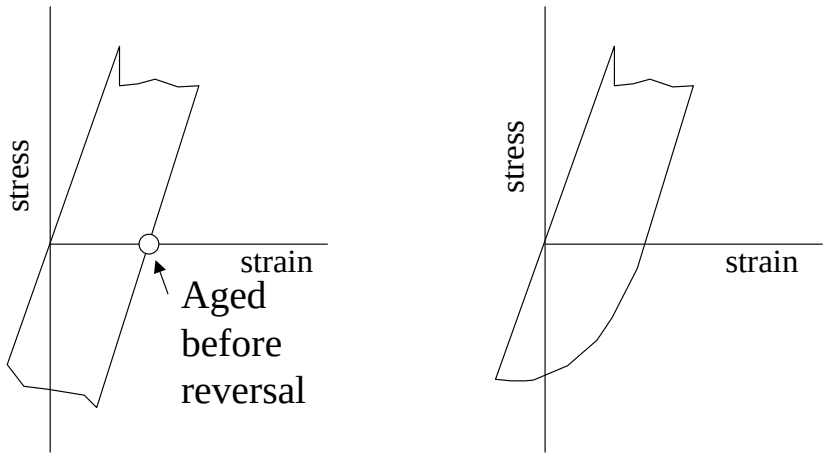

Figure 5.5: Schematic diagrams of system performance tests, left: material aged before reversal, right: material not aged before reversal.

Chapter 6

Results

The Lausanne results are documented in Section 3.1 page 47-59, since they preceded the experimental design. To summarize the Lausanne results:

1. In the torsion tests, where straining was done in forward and reverse directions, with and without ageing, there is no evidence of a yield point in reverse or forward straining. Microstructurally, there is a slight difference in the dislocation structures of the unaged and aged samples (dislocations appear pinned).

2. No yield point was seen in the interrupted tensile tests on a bake-hardening steel (ultra low carbon steel strain series), but there was still the expected progression from loose dislocation tangles to a cell structure as the strain is increased from 1.8% to 5.45%.

6.1 Torsion tests with designed equipment

The results are plotted in Figure 6.1. In all graphs, first (heavy curve) is forward straining, second curve (light) is reverse strain. There was a large amount of noise in the system, but fortunately, a large number of data points were taken, so that a 100 point moving average was used to smooth the data. It was seen that the samples did not yield in the expected way, having no upper or lower yield point and no Lüders region. Only a single sample (A41) yielded in a discontinuous manner on the first forward straining (shown in Figure 6.1,f). The torsional yield was taken as the deviation from elastic loading as defined in Appendix D.1, page 172. The torsional shear stress in forward, $\tau_{y\ forward}$, and reverse, $\tau_{y\ reverse}$, straining directions are

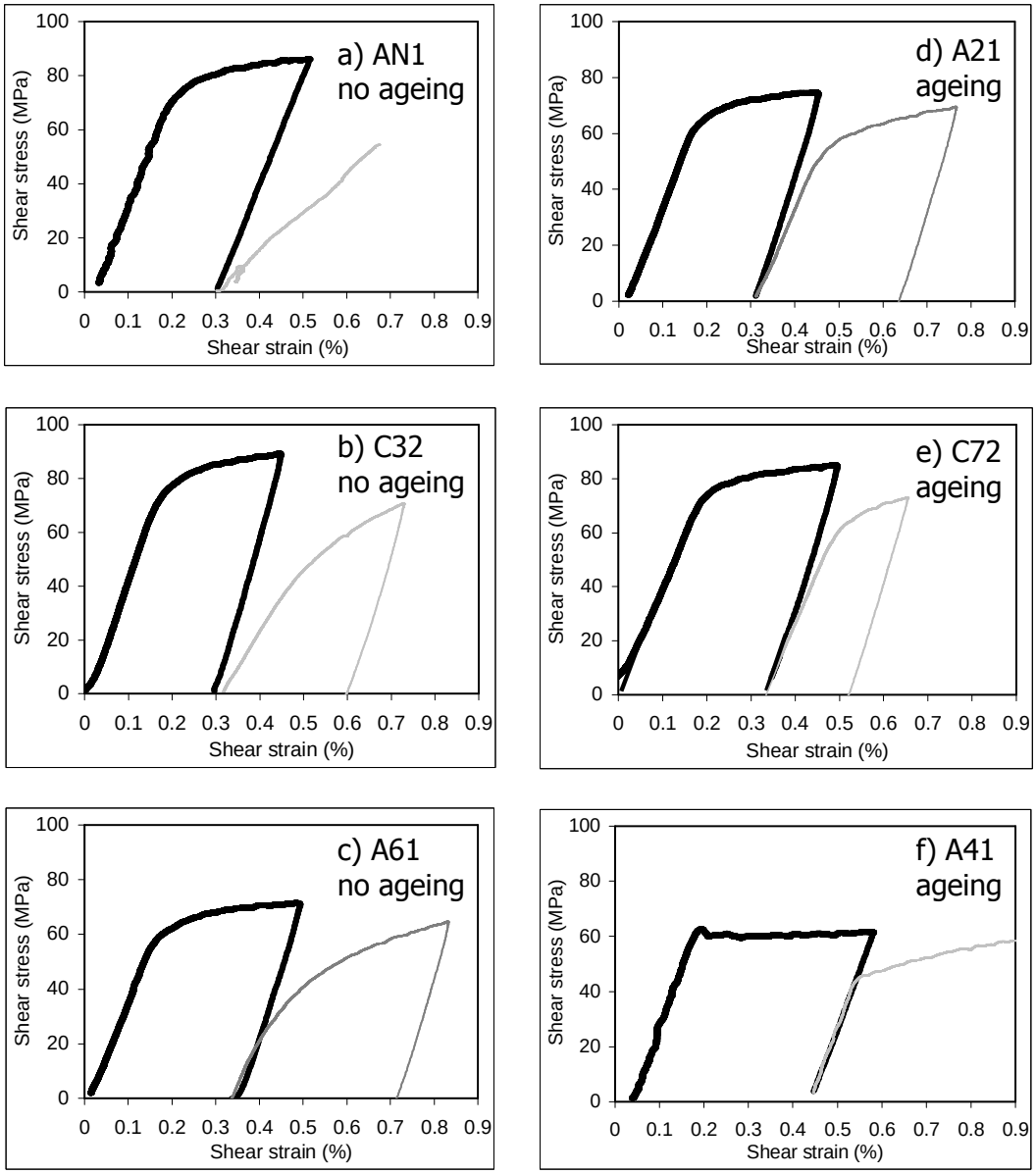

Figure 6.1: Torsional stress-strain curves for all samples, a-c) un-aged condition and d-f) aged condition (97°C for 1hr).

a-e) Stress relieved at 700°C.

f) Austenitised.

shown in Table 6.1. Ageing appears to have increased value of $\tau_{y\ reverse}$. The difference between the lower yield stress (or 0.1% proof stress) after ageing and the flow stress observed at the *end* of first (forward) straining $\Delta\tau_y$ is calculated and plotted in Figure 6.2.

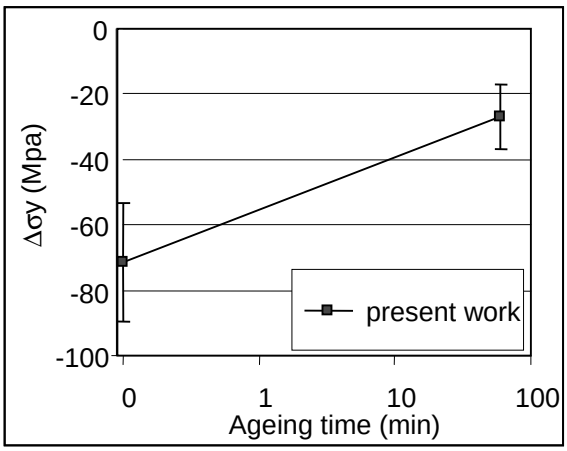

Figure 6.2: Rise in reverse yield with ageing time.

Table 6.1: Torsional shear stress for all samples.

Sample	$\tau_{y\ forward}$ (MPa)	aged	$\tau_{y\ reverse}$ (MPa)	$\Delta\tau_y$ (MPa)
AN1	71	no ageing	no yield	-
C32	66	no ageing	5	-84
A61	54	no ageing	13	-59
A21	59	aged	41	-34
C72	69	aged	54	-31
A41	62	aged	46	-16

Since the samples, on the whole, show no upper yield, causes for the lack of upper yield were investigated by analyzing uncertainties and the differences in the sample microstructure.

6.2 System analysis

Possible causes for the lack of upper yield are:

1. Microstructure.

2. Torsion machine stiffness.

3. Sample machining quality.

6.2.1 Microstructure

The microstructure for each sample was prepared in the conventional manner and etched in 2% nital. The optical micrographs are shown in Figure 6.3. No pearlite or grain boundary cementite was seen. Sample A41 can be described as having a polygonal ferrite microstructure (where the grains are equi-axed), while the other samples has a combination of Widmanstätten (where the grains are acicular) and polygonal structure, which defines allotromorphic ferrite microstructure. The grain size is highly variable between the samples and some abnormal grain growth has occurred (some grains are more than ten times the size of the smallest). The average grain size for each sample, $\overline{d}$, is calculated using the line intercept method as follows [83]:

$$\overline{d} = \frac{1.86 L_i}{N_{gb}}, \tag{6.1}$$

where L_i is the length of the line in the line intercept method and N_{gb} is the number of grain boundaries crossed by line L_i. Using Equation C.3, page 171, the uncertainty in the grain diameter is

$$\Delta\overline{d} = \sqrt{\left(\frac{1.86\Delta L_i}{N_{gb}}\right)^2 + \left(\frac{1.86 L_i \Delta N_{gb}}{N_{gb}^2}\right)^2}. \tag{6.2}$$

Sample A41 had a significantly smaller grain size than the other samples. If the relationship between yields (as measured by deviation from elastic behaviour) and grain size is plotted (Figure 6.4) then there is very little correlation. Thus, although the lack of upper yield may be due to a larger allotromorphic micrcostructure, the actual value of yield deviation is not related to grain size.

6.2.2 Torsion Machine Stiffness

If the Avery torsion machine was not stiff enough, then a yield point would be masked. Even though a single sample (A41) did show a small upper yield, an analysis

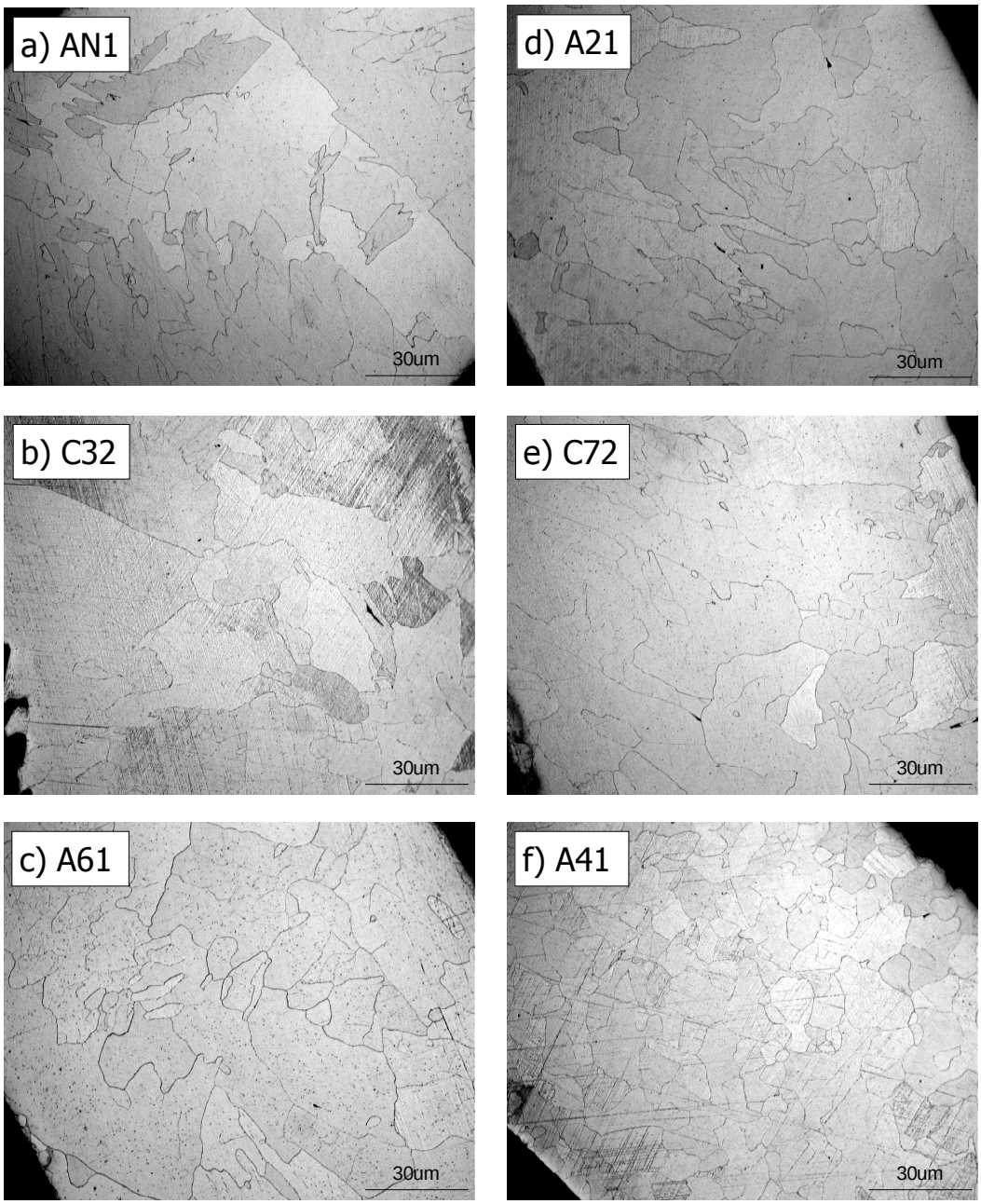

Figure 6.3: Microstructures of all samples after testing.

Table 6.2: Average grain sizes for each sample.

Sample	$\overline{d}$, (μm)	Sample	$\overline{d}$, (μm)
AN1	14.34 ± 0.37	A21	13.64 ± 0.33
C32	21.52 ± 0.83	C72	18.64 ± 0.62
A61	15.54 ± 0.43	A41	9.81 ± 0.17

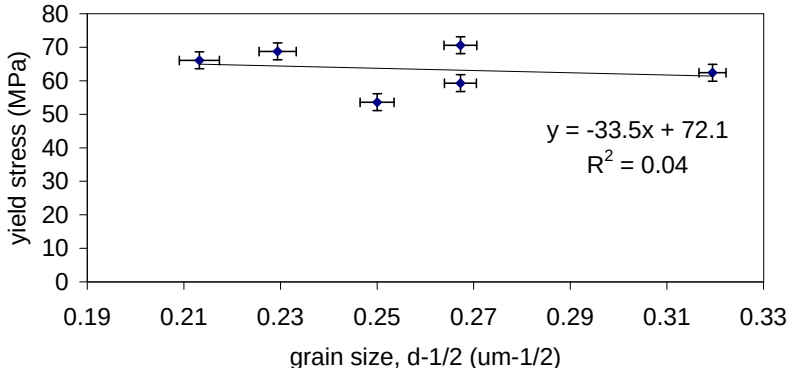

Figure 6.4: The relationship between grain size and torsional yield for all samples.

was performed to confirm that a yield drop can be observed with the experimental setup.

A statistical analysis of the system is required. The yield and modulus were calculated from the data (refer to Appendix D.1, page 172). The yield point was estimated as the point of deviation from linearity, as determined by a residual plot of the least squares regression fit of the elastic region (Figure D.1). This was done to ensure that information was obtained from the raw data in a reproducible way.

There are variations for each sample in the torsional yield, and in the slope of the elastic region (measured in first loading). First it must be determined if the variations are larger than the experimental error. The experimental error is determined from the uncertainty in the measurements. The following uncertainties must be considered:

- Uncertainty in the torque measurement (torsional stress),
- Uncertainty in the angle measurement (torsional strain) and thus,
- Uncertainty in the prediction of the shear modulus as well as,
- Uncertainty in the sample dimensions as a result of the machining.

The details of the uncertainty analysis of yield and modulus are also in Appendix D.2 and D.3 respectively. A summary of the uncertainties in torsional yield and shear modulus are shown in Table 6.3 and Figure 6.5.

The average torsional shear modulus is 40.9GPa with a standard deviation of 3.37GPa.

Table 6.3: A summary of the torsional yield and torsional shear slope for the first loading.

Sample	Torsional shear modulus (GPa)	Torsional yield (MPa)
AN1	39.1 ± 2.25	70.6 ± 2.52
C32	47.6 ± 2.71	66.1 ± 2.52
A61	40.3 ± 2.40	53.6 ± 2.52
A21	40.4 ± 2.32	59.3 ± 2.52
C72	38.5 ± 2.13	68.8 ± 2.52
A41	39.4 ± 2.28	62.4 ± 2.52

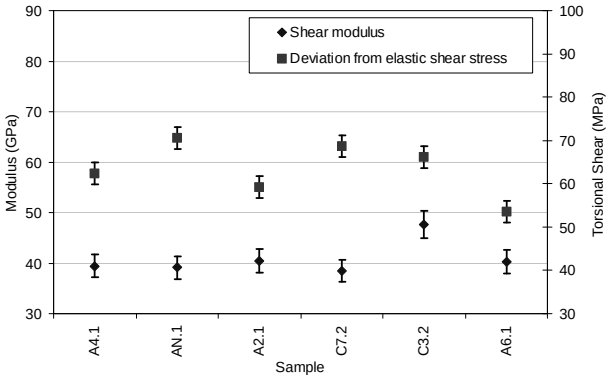

Figure 6.5: Torsional modulus and torsional shear stress for all samples, for the first loading.

As may be seen from Table 6.3, the slopes in loading are repeatable within experimental uncertainty, although sample C32 is the exception. Using Chauvenet's criterion [82], it was determined (in Appendix D.4 page 179) that this spurious data point is an "outlier" and can be ignored. Thus, the resulting average shear modulus is 39.5GPa with a standard deviation of 0.81GPa. A similar analysis for the yield values does not indicate that any of the yield values can be rejected (Appendix D.5 page 180).

However, the value of the modulus is around half of the expected value of 75-80GPa quoted in literature [68]. Due to the fact that only a single accelerometer could be obtained, the measured twist angle included the twist in the Avery torque measurement system as well. The the machine stiffness, $Stiffness_{machine}$ can be calculated from the twist ($Stiffness_{machine} = 7610Nm$). In Appendix D.6, page 180, the corresponding slope of the shear drop after yield was found to be 42×10^9Pa. This is a measurable shear drop which would be easily visible in the present system.

6.2.3 Sample Machining Quality

The samples were inspected for dimensional consistency. The samples were machined to a diamond finish to avoid nucleating Lüders bands from other areas than the groove (Section 4.3.2); however, when the samples were sectioned it was found that the inner and outer diameters were not concentric. It is thought that the reason for the misalignment in the samples is that the chuck/support designed for the machining of the samples was not aligned properly. This alters the polar moment of inertia of each sample, thereby affecting the calculation of the torsional yield and shear modulus. The polar moment of inertia (I_p) was recalculated using thickness measurements on the samples, using the parallel axis theorem [68], the details of which may be found in Appendix D.3.1, page 175. This was incorporated into the equations for shear modulus and the torsional yield. Even after this, there were still variations in yield.

Of concern was the groove depth, because an inconsistent groove depth about the sample circumference would result in localized yielding at low strains, thus the groove was measured. The groove depth was estimated by using a piece of fine wire and a vernier, as illustrated in Figure 6.6, by measuring the wire diameter and measuring the combined thickness of the wire in the groove and the sample, then obtaining the

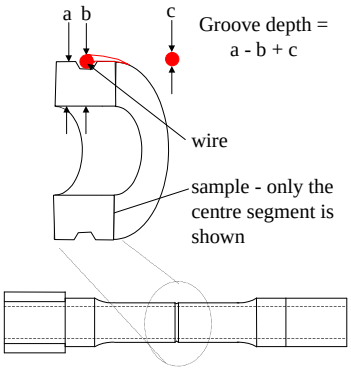

Figure 6.6: Method of estimating groove depth.

depth by the difference. These depths are given in Table 6.4. The grooves were not concentric, but the deepest part of each groove was recorded.In Figure 6.7, the yield is plotted against groove depth.

Table 6.4: The groove depths of the various samples as estimated by the method in Figure 6.6.

Sample	Groove depth (mm)
AN1	0.14 ±0.02
C32	0.14 ±0.02
A61	0.32 ±0.02
A21	0.18 ±0.02
C72	0.14 ±0.02
A41	0.18 ±0.02

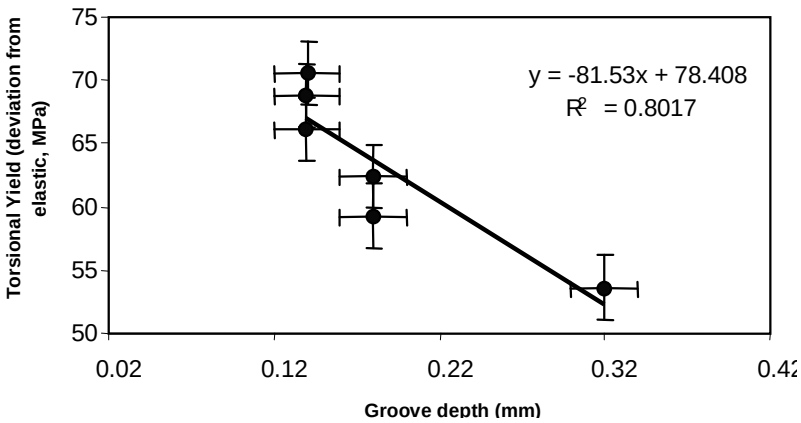

Figure 6.7: Groove depth versus torsional yield.

6.3 Summary of Results Analysis

The analysis has yielded the following results:

1. Lack of yield drop and Lüders strain correlates with samples having the larger allotromorphic microstructure.
2. Avery torsion machine would show a yield drop of $42 \times 10^9 Pa$.
3. Groove depth correlates with deviation from the elastic modulus (plastic yield).
4. Modulus is repeatable within the experimental error, but lower than expected.

Chapter 7

Discussion

7.1 Yield analysis

7.1.1 Yield and sample microstructure

While it is acknowledged that accurate measurements of upper yield have proved a difficult problem in metallurgy [20], it is disturbing that in all the preliminary samples, excepting the last sample in Figure 6.1f, neither an upper or lower yield appeared.

The samples with larger allotromorphic grain structure (Figure 6.3a-e and Table 6.2) do not have an upper yield, while the finer-grained material (sample A41, Figure 6.3f) does. The reason for the differences in grain size is that sample A41 was given the full austenitising treatment, while the other samples were only stress relieved. The grain size effect is very well documented in the literature (summarized in Section 2.2.7).

Hutchison[43] showed that although there is a relationship between upper yield and grain size, the slope differs from that of the relationship between lower yield and grain size. At large grain sizes, upper and lower yield lines intersect and there is no difference between upper and lower yield point. This occurs in Armco iron (0.03%C) at room temperature at a grain size of 180μm. In the present work the maximum grain size is 22μm. However, there may be critical differences between tensile versus torsion testing. Cottrell[84] and Hall[85] also observed that a fine scratch hardly affects the yield point of fine-grained iron. Thus, the upper yield of a finer grain material is less susceptible to stress concentrations than that of a coarse grained

material. This may explain the lack of yield in the coarse grained samples of the present work. It is also surmised that the allotromorphic structure and mixed grain size structure can lead to a deviation (decrease) in the expected yield from the Hall-Petch equation [86]. However, their results were from partially recrystallised ferrite produced by controlled rolling, where the microstructure would not be the allotromorphic structure seen here, thus confirmation of this postulate is beyond the aim of this investigation, which is to design the torsion apparatus.

The grain size of sample A41 is 9.8μm which corresponds roughly to about 150 grains across the sample thickness, while for the material with the largest grain size there are 65 grains across the thickness. From literature [58, 59], in Section 2.5.1, the ratio of thickness to grain size should be > 20. Where the material thickness is reduced by the groove, the smallest thickness to grain size ratio drops to 60. It seems that the grain size is still within the limits that are given in literature [58], although perhaps again there are critical differences for tensile versus torsion testing. Additionally, in Wilson and Ogram's [4] work, the fine-grained material had 60 grains through thickness, while their coarse-grained material has 15 grains across. They still obtained yield points in the first testing of the coarse-grained material, in comparison to the lack of yield in the present work. The mixed grain size may account for the difference, but confirmation is beyond this investigation, since the aim is to design the torsion apparatus.

From the previous two arguments, it appears that the lack of yield seems to be a complex issue, and since only effect that correlates with lack of yield is the microstructure, it is speculated that the presence of allotromorphic ferrite in combination with the groove prevents the appearance of yield point. Although this is not part of the original aim of the dissertation it does suggest that an alternative method of investigating the strain ageing anisotropy could be done by comparing different microstructures (acicular to polygonal). Conceivably, one advantage of a lack of Lüders region in the samples is that a low uniform pre-strain can be achieved during the pre-straining. This is impossible in a microstructure that displays a Lüders strain, since the material is either strained to the Lüders strain where the Lüders band has already passed or is unstrained.

The microstructural differences do seem to explain the lack of discontinuous yield in the coarse-grained samples, but even in the fine-grained sample, the upper yield point (Figure 6.1f) is not very high above the lower yield (less than 3MPa, as seen

in the enlargement (Figure 7.1) of Figure 6.1f), while other authors have reported yield drops of 17MPa [3] and 27MPa [4].

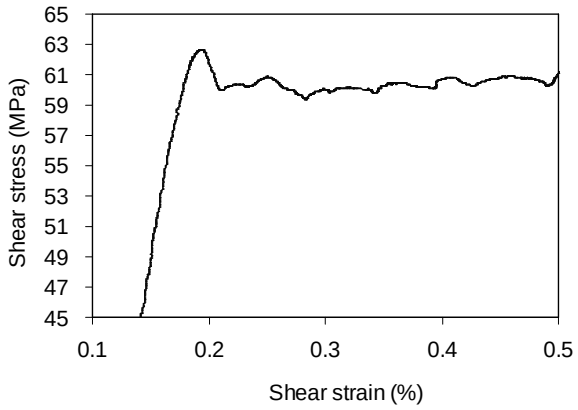

Figure 7.1: Enlargement of the first yield from sample A41.

This yield variation will be dealt with in Section 7.2. The decision to stress relieve rather than austenitise was unfortunate, but does not seem to be the cause of the low yields, since even A41, which has the finer microstructure, has an unexpectedly low yield.

7.1.2 The effect of ageing on yield

In the A41 sample, the yield point has not returned after ageing at 97°C for 60min. This confirms Elliot *et al.'s* work [3].

Although the large-grained aged samples (C72, A61) did not show an upper yield, ageing still has some effect. In Table 6.1 reverse torsional yield $\tau_{y,\ reverse}$ is between 8-24% of τ_y while after reversal and ageing it is around 68-78%. This is plotted in Figure 7.2 with Wilson and Ogram's measurements. In Wilson and Ogram's[4] work, yield in a 26μm grain size returns at an ageing time of 200min. The present work is also consistent with his observations. Additionally, in both Elliot's work and the present work, $\Delta\tau_y$, the difference between $\tau_{y\ reverse}$ and τ after the pre-strain, appears to be similar. Unfortunately, the variability in the yield means that the confidence in these trends is limited.

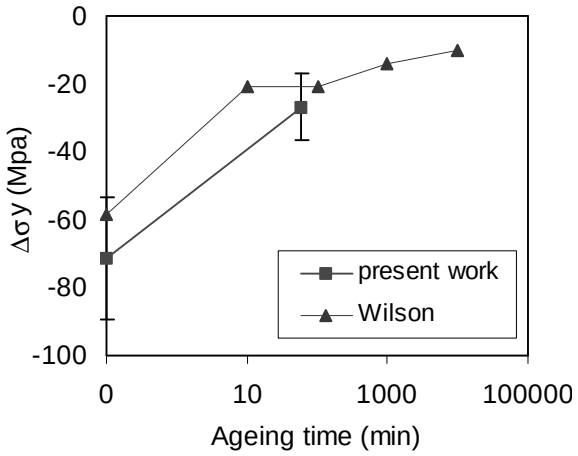

Figure 7.2: Rise in reverse yield, $\Delta\sigma y$, with ageing time, a comparison with Wilson and Ogram's results [4].

7.1.3 Yield and solute carbon

One of the obvious metallurgical reasons for the lack of yield could be that there is insufficient carbon in solution for any ageing in the large grained samples.

The amount of carbon in solution at a given temperature can be found in Hall's work [39]. For convenience this has been reproduced in Table 7.1. According

Table 7.1: Solute C in Fe at various temperatures, from [20].

Temperature (°C)	[C] wt%
200	0.00007
500	0.0056
700	0.035
900	0.1

to Cottrell and Bilby[1], in a well annealed steel (with a dislocation density of 10^8lines/cm^2), about 10^{-6} wt%C is required for pinning. This would suggest that Wilson and Ogram's work[4], where they quenched their samples from 200°C (leaving 0.00007wt%C in solution), gives sufficient carbon in solution, which is borne out by the presence of yield on first straining. In this work, the samples were air cooled from 500°C and 700°C in the stress relieving treatment and austenitising treatment respectively and it is expected that there will be enough residual carbon.

It is therefore unlikely that lack of solute is the reason for the absence of yield. In addition to this, the slight increase of yield on ageing after reversal (Figure 7.2) seems to confirm that there is some solute present.

7.2 System analysis

The deviation from linearity was at a very low stress (65MPa as compared with the expected 95MPa of Section 4.3.2). The variability is possibly due to:

- The measuring system being inaccurate,
- Avery machine is too soft (Shear modulus analysis),
- Samples being defective.

7.2.1 Detection limits of system

Calibrating the system should be the indication of the performance of the system; however, the statistics of the calibration should be taken into account. In both torque and strain calibrations, more points should have been taken; sub-optimizing the calibrations by reducing the number of points resulted in a loss of certainty. The precision errors on both the strain (Figure C.2, page 170) and stress calibrations (Figure C.3, page 171) are so small in comparison to the uncertainty of the trend line that they are ignorable. This could be partially eliminated by better planning on the part of the experimenter, where cognisance of the statistical analysis should be part of the planning (experimental methodology) in any experimental protocol.

However, comparing this to published figures of the strain resolution (in Table 4.4, page 71) while this is less than ideal, it is no worse than other experimenters [3, 28]. More calibration points could have reduced the uncertainty to around 0.005% which is the strain corresponding to the accuracy of the accelerometer. However, improvement in calibrations would not eliminate the requirement of two accelerometers.

From the torque tube design, a torque resolution of 1.57Nm was desired (Equation 4.50 in Section 4.5.3, page 84). The calibration showed that the uncertainty in reading was 1.14Nm. The required torque precision was achieved.

However, in terms of the gauge resolution:

$$\begin{aligned}
\epsilon_{45^{\circ}} &= \frac{Tr_o}{\pi G(r_o^4 - r_i^4)} \\
&= \frac{T\ 16 \times 10^{-3}}{\pi\ 80 \times 10^9((16 \times 10^{-3})^4 - (10 \times 10^{-3})^4)} \\
&= 1.15T\ \mu\varepsilon. \\
&= 1.3\mu\varepsilon.
\end{aligned}$$

puts the measurements on the lower end of strain gauging practice, whereas most practitioners [71, 87, 88] would recommend $2 - 10\mu\varepsilon$. Thus, the accuracy requires explanation. Considering a torque resolution of 1.14Nm (and corresponding gauge resolution of 1.3 micro-strain) the output voltage on the Wheatstone bridge is:

$$\begin{aligned}
V_{out} &= V_{ex} k \epsilon_{45^{\circ}} \\
&= 2.5\ \times\ 2\ \times\ 1.3 \\
&= 6.5\ \mu V
\end{aligned} \tag{7.1}$$

This is reasonably easy to measure with dedicated strain gauge signal conditioners and amplifiers (HBM), combined with the fact that the tests are conducted over short times (20 minutes) in a laboratory environment. A preliminary estimate of the noise in the torque system (by calculating the standard deviation using the first 30 measurements in the test, well before the start of straining) gives a 2σ value of less than 0.3Nm, or $1.7\mu V$.

The yield drop of 3MPa in sample A41 would produce a signal of $94\mu V$, which is more than ten times greater the uncertainty ($6.5\mu V$ in Equation 7.1) and more than fifty times greater than the noise ($1.7\mu V$). Thus, the system can measure the yield drop in an acceptable manner.

Therefore, while it is accepted that the design of the torque measuring system is on the limit of what can be achieved, it appears to have met the required torque precision. It is worth exploring the variations in yield and where they are suspected to arisen from.

7.2.2 Shear modulus analysis

The calculation of the experimental uncertainly is a guide to what the error should be. If the results fall beyond this, then it shows there is an unexplained (by the measured errors) deviation. The variation in shear modulus is within the experimental uncertainty, since the standard deviation (0.81GPa) is less than the experimental uncertainty (2.40GPa). The modulus of C32 was determined as an outlier using Chauvenet's criterion [82]. However, the value of shear modulus is well below that of low carbon steel, since the machine stiffness is being measured as well.

In Appendix D.6, page 180, it is calculated that the machine stiffness is 7610Nm/rad, while the sample stiffness is 6820Nm/rad. The machine stiffness is a combination of the frame and the torque tube. The torque tube stiffness is 58000Nm/rad, thus, the reduction in machine stiffness comes from the Avery frame.

So while sample and machine stiffnesses are similar, the yield drop of 42×10^9 Pa can still be obtained. An enlargement of the A41 curve, Figure 7.1, shows little evidence of a smeared yield, such as that described in Hall [39] for a soft machine.

It is also observed that slope in loading is different from the slope on unloading, the reason for this is that on loading, the machine 'tightens up' slowly as there is force required to overcome friction. On unloading, this force is not reversed, leading to a steeper slope on unloading. The Avery's old torque measuring system is in all likelihood the greatest source of frictional compliance (Figure 7.3) and it would be preferable that a new system would not have such a mechanism attached to it.

The use of a properly defined gauge length (two accelerometers) would avoid this problem. Alternatively, the procurement of an Linear variable displacement transducer (LVDT), which accurately measures displacement, would be advisable.

7.2.3 Sample machining accuracy

While the calculation of the experimental uncertainly is a guide to what the error should be, if the results fall beyond this, then it shows there is an unexplained (by the measured errors) deviation. Using Chauvenet's criterion [82] (Appendix D.5, page 180), indicates the real presence of variability in the yield, and none of the yield values can be rejected.

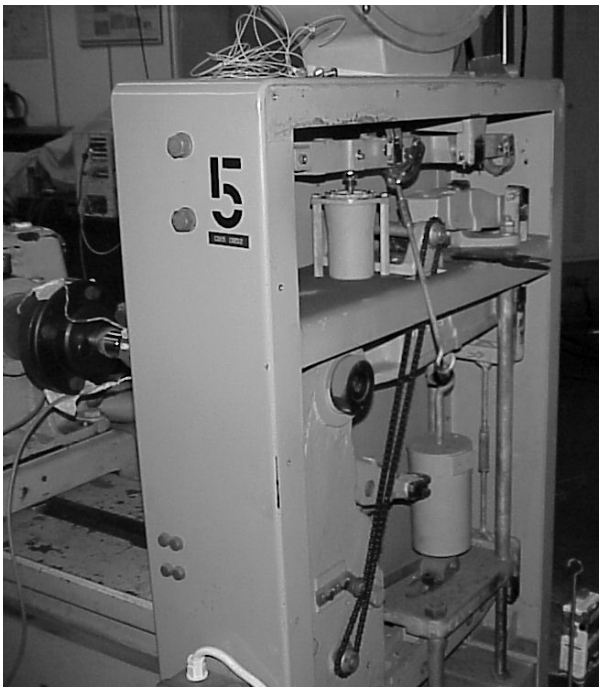

Figure 7.3: Old Avery torque measuring system.

The grooves were also seen to be uneven, (Section 6.2.3) as well as not the same as required in the design. In Figure 6.7, the yield is plotted against groove depth and there is a reasonable linear correlation between the groove and the torsional yield (the groove depth was nominally 0.16mm but varied from 0.14 to 0.32mm). This indicates that there may be a problem with the stress concentration of the groove. Good correlation is shown (Figure 7.4) between the theoretically predicted yield stress (including stress concentrations) and the experimental results. It would be necessary to re-design the groove to be less deep, since even in sample A41, there was still a very low upper yield point. It would be better for the groove to be sharp rather than deep, since it is the sharpness that would encourage the dislocation motion [44].

The relatively good trend between yield value (as measured by the deviation from elastic behaviour) and the groove depth does show that sample machining was important, as suspected from the beginning (Section 4). The stipulated groove depth of 0.16mm was too deep, since the yield stress is lowered from 95MPa to 65MPa.

The groove should be redesigned in the next study to avoid machining difficulties and ensure sufficient sharpness, while better quality control is recommended during machining. Alternative machining techniques (such as electrospark cutting), which

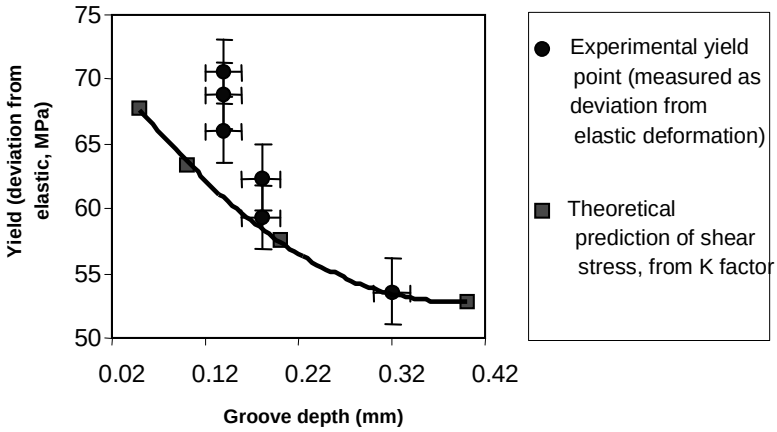

Figure 7.4: Groove depth versus torsional yield.

have the potential of being more accurate, could also be investigated. However as discussed before in Section 7.1.1, upper yield is also more greatly affected by groove depth in coarse grained material, so avoidance of coarse grained material is still necessary. Dimensional checks of the specimens received from machining should have been done. While non-concentricity checks would have been difficult, the variable groove depth ought to have been checked.

7.3 Other considerations

It appears that an emphasis was placed on the theoretical side of the work, to the detriment of experimental planning and execution. However, some of the experience of planning and execution are only gained in hindsight, and with a greater supply of resources, the encountered problems would have been overcome. From this discussion, the experimenter has shown that familiarity with the technique has been gained, although the resources (especially time) for further work are unavailable. The pitfalls of torsional testing are clearly illuminated. However, another worker could continue, using the findings of this investigation.

7.3.1 Experimental design

The strain measurement system was potentially highly accurate, although, the unavailability of one accelerometer resulted in a serious degradation of this parameter.

This parameter is fortunately less significant in the measurement of upper yield and the stress drop than is the torque measuring system.

A discussion of other torque designs (by this author) may be found in Appendix B.3.4, page 157. It is quite clear from the choice of the final dimensions of the torque tube that the practical parameters (manufacture and cost) override the choice (ideal design) based on required sensitivity, stiffness and the mechanics of solids parameters.

7.3.2 Statistics

It is clear that the calibration statistics should have been planned into the experiment at the design stage; however, it is not all that easy to do. Some of the statistics in this experiment were only deduced after testing. A better route may be an iterative procedure on experimenting and redesign. However, given discussions on sample machining, it was not worthwhile pursuing higher precisions on the current samples and equipment. It is recommended that enough data points are taken during calibration to ensure the precision of the instrument is the dominant uncertainty.

7.3.3 Signal averaging

In the present work, the noise on the curve was removed through 100 point averaging. At a sampling frequency of 4Hz, this results in the data being averaged over of 25sec. Others [3] read one point every 2min, thus the averaging is an acceptable smoothing technique. They also used hand-driven equipment, but had the advantage of only performing one measurement per hand driven strain cycle, ostensibly "after the transient vibrations had died down" [3]. Van Rooyen also reports hysteresis effects when using a clip gauge in tensile testing, which he attributes to an unstable Lüders front [62], so that some "noises" are inherent in tests in region of the Lüders strain.

The system analyses were done on the unfiltered raw data (for example, Appendix D.1, Figure D.2, page 173), to avoid the possibility of error from the averaging. While design errors, such as the loss of one acelerometer in the strain measuring system and the possible compliance of the nylon grub screws and elastics, could have introduced extra noise, it is seen that the noise is readily removed with the averaging.

7.3.4 Sample material

Careful austenitising of the material (Section 2.5.1) would result in an equi-axed fine grain size and the appearance of discontinuous yield, as seen in the case of sample A41. However, there is no point in testing austenitised samples to confirm that the groove has been poorly machined.

7.3.5 Time constraints

The accelerometer was kindly lent by CSIR; however it was also required for commercial projects shortly after the testing was completed and thus there was a time constraint to complete this experimental work. In addition, the unfortunate withdrawal of one of the accelerometers at the last moment resulted in the degradation of strain measurement system. Obviously, this had not been planned.

7.4 General discussion/Final comments

The lack of yield after ageing in the reverse direction confirms what other researchers[3, 4] have observed. It would be advisable to use lower yield as a measure of return of yield as in Wilson and Ogram's [4] work, since the present work does confirm the observation of Hall that upper yield has proved a difficult problem in metallurgy [39]. The lack of discontinuous yield was attributed to the coarse allotromorphic grain structure. The low yield, as measured by deviation from yield, was shown to be dependent on groove depth (Figure 6.7). Poor machining resulted in this variable sample geometry.

This work showed that the correlation of microstructure with the mechanical properties is not a trivial exercise. Insufficient attention was paid to the calibration statistics, although sufficient data were extracted to assess the performance of the system.

The next section is the proposed criteria for an improved design based on the experience gained in the present design.

Chapter 8

Criteria for a new design

8.1 Goal statement

The goal is to design a system that measures dislocation behaviour in a forward and reverse direction in the presence of solute carbon. It must measure the dislocation motion (stress, strain) in a statistically significant manner in a uniform stress field. This would allow the measurement of upper, lower yield and the Lüders region. The measurements would be the bulk average strain and the uniform stress in a sample that consists of low dislocation density ferrite grains and solute carbon. To reduce experimental uncertainty, it is desirable to measure the stress and strain in the most direct manner. The output of the equipment would be similar to the graph in Figures 2.1 and 2.2, with improved resolution.

8.2 General requirements of testing system

The general requirements of the testing system are given below.

1. System stiffness required for a yield drop $\frac{d\tau}{d\gamma} < -10$MPa. In a torsion design this corresponds to the sample and machine stiffness being roughly equivalent. The machine stiffness requires the consideration of the torque tube and frame.

2. Equipment not to fail by buckling or plastic deformation in use (i.e. be strong enough). It is desirable that a safety factor > 2 on the equipment (frame and measuring system) must be used. A robust design is required.

3. (*desirable*) Must not add unquantifiable noise to the strain, stress measurements.

4. (*desirable*) It is must incorporate as much standard existing equipment as possible.

5. (*desirable*) Easy to use, fast to set-up (so that many samples can be readily tested).

6. (*desirable*) It is desirable that the design is as cheap as possible.

For general literature requirements and the rationale, refer to research methodology Section 2.5, page 42. The specific requirements for each element in the design is given below.

8.2.1 Frame

The frame must not introduce secondary stresses into the sample (well aligned frame). It must be stiff.

8.2.2 Sample

1. The sample material requirements are:

   (a) Low carbon (<0.02 wt%). No precipitation (low Al, N and S). Reduce other impurities to the minimum.

   (b) Sufficiently fine-grained for upper yield to appear, in the case of torsion the sample thickness to average grain diameter, $\frac{t}{d} > 150$ (Section 7.1.2).

   (c) Low density dislocation structure (well annealed). Fairly slow cooling rate (do not quench) during the phase transformation from austenite to ferrite [48], (Sections 2.2.5, 7.1.3).

2. The sample dimensions requirements are:

   (a) Torsion sample must be thin-walled, see Appendix B.1.2 for calculation of internal strain during torsion.

   (b) A single pair of Lüders front are to be initiated (shallow sharp groove/some stress concentration). In the previous design, the yield was affected by the

groove depth, and the groove depth was not constant. Experimentation with groove design or other Lüders band "initiator" is required (Section 7.2.3).

(c) Repeatability and geometrical accuracy in machining is required, and the surface finish must be good (Section 7.2.3).

8.2.3 Strain and Stress measurement

The requirements for stress and strain measurement are illustrated in Figure 8.1.

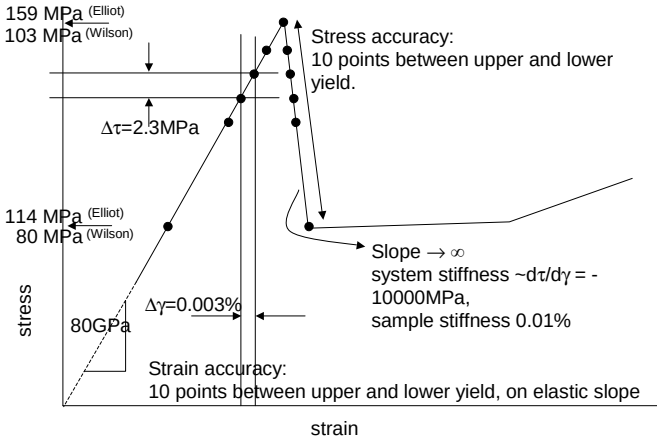

Figure 8.1: Requirements for stress and strain measurement.

1. The previous tests showed the necessity for better strain measurement accuracy, as well as a method of eliminating or accounting for vibration (Sections 7.2.2, 7.2.3, 7.3.3).
2. Maximum strain would be at least 5%, maximum stress 193MPa.
3. Strain measurement accuracy 0.003%; stress measurement accuracy 2.3MPa.
4. (*desirable*) It is desirable that the data be directly obtained via computer, sampling with time base.

8.3 Process requirements

The test should be strain-rate controlled (rate between 10^{-4} and $10^{-6}s^{-1}$) and the strain sense must be reversible.

8.3.1 Calibration

Calibration of stress and strain systems must be to known standards. Sufficient calibration points (30-50) should be taken for statistical validity (Section 7.3.2).

Chapter 9

Conclusions

Although the work recorded in this dissertation to build a functional torsional tester was achieved, given an improved strain measurement system, all the information that has been painstakingly derived can also be used again to facilitate testing. Some of the more important findings with regards to testing are listed below.

1. It should be noted that when a fine grain size was achieved, a sharp yield point was observed and, although more testing is required, this result does suggest that the strain ageing anisotropy phenomenon does occur with torsion testing (which was the original aim of the work). This lack of yield after ageing in the reverse direction confirms the observations of other researchers[3, 4].

2. It is thought that the general absence of a sharp yield in the present work was a combination of a large allotromorphic grain structure and unsuitable sample design (details below). This was in spite of the grain size being within the limits given in the literature.

3. In the ideal design of a torque tube, a tube above a minimum radius can achieve any desired combination of sensitivity and stiffness. Sensitivity and stiffness in principle are not competing requirements, although, for real materials (with strength, buckling and machining limits) there is an allowable design region.

4. In the testing of the the torsion system:

   (a) The torque measuring system was on the limit of the resolution. A design that meets the required torque precision can be achieved, in spite of the high resolution requirements.

(b) The good correlation between yield value (as measured by deviation from linearity) and the groove depth shows that sample machining was important, it also shows that the sample groove depth of 0.16mm was too deep as the yield stress is lowered from 95MPa to 65MPa (Section 7.2.3).

(c) The measured uncertainty of the strain system was not indicative of the true performance of this system. The uncertainty of the strain system could be significantly improved by increasing the number of calibration points and thereby improving the statistics of the strain calibration (Section 7.2.1). However, improvement in calibrations would not eliminate the requirement of two accelerometers.

(d) Electron microscopy is an important technique for studying strain ageing anisotropy. The TEM work has shown the influence that small strains have on the development of dislocation networks on forward stressing and there was also some evidence for strain ageing leading to the pinning of dislocations on reverse stressing. Further work is required preferably on very low carbon steels having a range of grain sizes.

Chapter 10

Recommendations

1. The relationship between dislocation structure and ageing properties has not been clarified, and there is scope for more work in this area. The effects of internal stress on the ageing properties merits more investigation, and use could be made of different microstructures (fine-grained, polygonal, allotromorphic coarse-grained) to elucidate the internal stress issue.
2. It would seem a necessary part of any further work to observe the return of yield with ageing time (Section 3.1.3), as well as ageing in situ under load.
3. In designing a new system, it would be optimal to introduce parameters like the manufacturing route and cost earlier on in the design process to eliminate the duplication of designs.
4. An alternative strain measuring system should be used.
5. The statistics of the calibration should be taken into account, especially in the strain measurement system.
6. It would be advisable that an alternative sample is designed.
    - The groove should be re-designed to avoid reducing the yield value excessively.
    - Accurate machining of samples is crucial to give consistent results, samples should be designed so that this can be achieved.
    - Better quality control is recommended during machining and samples should be designed so that this can be achieved.
    - Careful attention to sample composition and heat treatment is also required

References

1. A.H. Cottrell and B.A. Bilby. Dislocation theory of yielding and strain ageing of iron. *Proc. Phys. Soc.*, LXII:49–63, 1948.

2. C.F. Tipper. Effect of direction of rolling, direction of straining, and ageing on the mechanical properties of a mild steel plate. *J. Iron Steel Inst.*, 172:143–148, 1952.

3. R.A. Elliot, E. Orowan, T. Udoguchi, and A.S. Argon. Absence of yield points on strain reversal after ageing, and the Bauschinger overshoot. *Mechanics of Materials*, 36:1143–1153, 2004.

4. D.V. Wilson and G.R. Ogram. Directionality of yield point in strain-aged steels. *J. Iron Steel Inst.*, pages 911–920, Sept 1968.

5. J.D. Baird. The effects of strain ageing due to interstitial solutes on the mechanical properties of metals. *Metallurgical Reviews*, 149:1–18, 1971.

6. D. Williams. Interaction between Bauschinger effect and strain ageing. *Met. Trans. A.*, 11A:1629–1631, September 1980.

7. R.W. Hertzberg. *Deformation and Fracture Mechanics of Engineering Materials.* Wiley and Sons, New York, Fifth edition, 1976.

8. M.S. Duesbery and V. Vitek. Plastic anisotropy in bcc transition metals. *Acta Met.*, 46(5), 1998.

9. T. Suzuki, S. Takeuchi, and H. Yoshinaga. *Dislocation Dynamics and Plasticity.* Springer-Verlag, Berlin, 1991. ISBN 3-540-52693-5.

10. J.C.M. Li. Some dislocation mechanisms in deformation, recovery and recrystalliszation of metals. *J.Aust. Inst. Metals*, 8(2):206–221, May 1963.

11. S.J. Basinski and Z.S. Basinski. *"Plastic Deformation and Work Hardening"*. Dislocations in Solids. North-Holland Pub. Co., First edition, 1979. ed F.R.N. Nabarro.

12. P.B. Hirsch. *"Observations of dislocations in metals"*. Internal stresses and fatigue in metals. Elsevier Pub. Co. London, Second edition, 1959.

13. T. Hasegawa, T. Yakou, and U.F. Kocks. Length changes and stress effects during recovery of deformed aluminum. *Acta Met.*, 30:235–243, 1982.

14. P.S. Bate. Effects of combined strain path and strain rate changes in aluminum. *Met. Trans. A*, 24A:2679–2689, December 1993.

15. G.I. Taylor. Plastic strain in metals. *J. Inst. Met.*, 62(10):307–324, 1938.

16. H. Mughrabi. On the flow stress of deformed crystals containing heterogenous dislocation distributions. *S. Afr. J. Phs.*, pages 62–68, 1986.

17. A.H. Cottrell. *Dislocations and plastic flow in crystals.* Oxford University Press, London, 1961.

18. D.G. Brandon and J. Nutting. Dislocations in α-iron. *J. Iron Steel Inst.*, 196:160–166, October 1960.

19. A.S. Keh and S. Weissmann. *Deformation Substructure in Body Centered Cubic Metals.* Electron Microscopy and the Strength of Crystals. Wiley, Interscience, New York, 1963.

20. E.O. Hall. The deformation of mild steel: III discussion of results. *Proc. Phys. Soc.*, 64:747–753, 1951.

21. N.J. Petch. The cleavage strength of polycrystals. *J. Iron Steel Inst.*, 174:25–28, 1953.

22. B. Mintz. Importance of K_y (Hall Petch slope) in determining the strengths of steels. *Met. Tech.*, 11:265–272, 1984.

23. B. Mintz, H. Ke, and G.D.W. Smith. Grain size strengthening in steel and its relationship to grainboundary segregation of carbon. *Mat. Sci. Tech.*, 8:537–540, 1992.

24. S. Weissmann and N. Hosokawa. Yielding of tantalum single crystals. *J. Aust. Inst Met.*, 8(1):25–32, February 1963.

25. M. Döner, H. Chang, and H. Conrad. Stress-strain behaviour and the dislocation structure at small strains in iron deformed in tension, torsion and combined tension torsion. *Met. Trans. A*, 6A:1017–1028, May 1975.

26. F.R.N. Nabarro. Department of Physics, University of the Witwatersrand. Private communication, 2001.

27. H. Mughrabi. Dislocation wall and cell structures and long-range internal stresses in deformed metal crystals. *Acta. Met.*, 31(9):1371, 1983.

28. G. I. Deak. *A study on the causes of the Bauschinger effect.* PhD thesis, Massachusetts Institute of Technology, 1962.

29. E. Orowan. *Causes and Effects of Internal Stresses.* Internal stresses and fatigue in metals. Elsevier Pub. Co., London, 1959.

30. D.V. Wilson. Reversible work hardening in alloys of cubic metals. *Acta Met.*, 13:807–814, July 1964.

31. G.E. Dieter. *Mechanical Metallurgy.* Mc Graw Hill Book Co., New York, 1988.

32. D.V. Wilson and P. Bate. Influence of cell walls and grain boundaries on transient responces of an IF steel to changes in strain path. *Acta Met. Mat.*, 42(4):1099–1111, 1994.

33. T. Hasegawa, T. Yakou, and U. F. Kocks. A unified representation of stress-strain curves in reversed direction of pre-strained cell-forming metals. *Trans. Jap. Inst. Met.*, 27(6):425–433, 1986.

34. B. Peeters, S.R. Kalidindi, P. Van Houtte, and E. Aernoudt. A crystal plasticity based work hardening/softening model for bcc metals under changing strain paths. *Acta Met.*, 48:2123–2133, 2000.

35. M. Döner, H. Chang, and H. Conrad. A comparison of the dislocation structures at small strains in copper deformed in tension and torsion. *Met. Trans.*, 5:1383–1391, June 1974.

36. J.D. Baird. Strain-aging of steel - a critical review, Part 2. *Iron & Steel*, pages 368–405, July 1963.

37. D.V. Wilson and G.R. Ogram. *Private communication to Baird in [36].*

38. C.F. Elam. The influence of rate of formation on the tensile test with special reference to the yield point in iron and steel. *Proc. Roy. Soc. A*, 135:568–592, 1938.

39. E.O. Hall. *Yield point phenomena in metals and alloys.* Macmillan and Co. Ltd, London and Basingstoke, 1970.

40. G.T. Hahn. A model for yielding with special reference to the yield-point phenomena of iron and related bcc metals. *Acta Met.*, 10:727–738, August 1962.

41. A.H. Cottrell. *Theory of the yield point of iron.* British Iron and Steel Research Association, Park Lane, London, W1, November 1948. Chapter II.

42. N.J. Petch. The upper yield stress of polycrystalline iron. *Acta Met.*, 12:59–65, January 1964.

43. M.M. Hutchison. The temperature dependance of the yield stress on polycrystalline iron. *Phil. Mag.*, 8:121–127, 1963.

44. A.H. Cottrell. Discontinuous yielding. *N.P.L Symposium 'Relationship between Structure and Strength in Metals'*, 2(15):455–473, 1963. Her Majesty's Stationery Office.

45. R.D. Butler and D.V. Wilson. The mechanical behaviour of temper rolled steel sheets. *J. Iron Steel Inst.*, page 19, January 1963.

46. T. Mura and J.O. Brittain. Contribution of dislocation line tension and the density of the solute atmosphere to the yield point in strain aged ingot iron. *Acta Met.*, 8:767–772, November 1960.

47. F.R.N. Nabarro. *Report of a Conference on Strength of Solids.* Phys. Soc., London, 1948.

48. A.S. Keh, Y. Nakada, and W.C. Leslie. *Dynamic Strain Ageing in Iron and Steel.* Dislocation Dynamics. McGraw-Hill Book Co, New York, 1968.

49. J. Bonneville. I.G.A, Ecole Polytechnique Fédérale, Lausanne. Private communication, 1997.

50. P. Elsen and H.P. Hougardy. On the mechanism of bake-hardening. *Steel Research*, 64(8/9):431–436, 1993.

51. H. Hu. Effects of solutes on Lüders strain in low-carbon sheet steels. *Met. Trans. A*, 14A:82–91, 1983.

52. P.J. Worthington. The upper yield stress of polycrystalline 3% silicon iron. *Acta Met.*, 15:1795–1798, December 1967.

53. N.J. Petch. *Theory of the yield point and of strain-ageing in steel.* Advances in physical metallurgy. The Institute of Metals, London, 1990. pp14-15.

54. F.R.N. Nabarro. Department of Physics, University of the Witwatersrand. Private communication, 1998.

55. E. Orowan. Theory of the yield phenomenon in iron. Unpublished work, 1967.

56. W.R. Thomas and G.M. Leak. Internal friction in steels. *J. Iron Steel Inst.*, 180:155, 1955.

57. J.O. Brittain and S.E. Bronisz. Stress induced strain ageing. *Trans. Met. Soc AIME*, 218:290, April 1960.

58. S. Miyazaki, K. Shibata, and H. Fujita. Effect of specimen thickness on mechanical properties of polycrystalline aggregates with various grain sizes. *Acta. Met.*, 27:855–862, 1979.

59. H. Fujita and S. Miyazaki. Lüders deformation in polycrystalline iron. *Acta Met.*, 26:1273–1281, 1978.

60. E. El-Magd, H. Scholles, and H. Weisshaupt. Influence of strain rate on the stress strain curve in the range of Lüders strain. *Steel Research*, 67(11):495–500, 1996.

61. D.J. Verel and A.W. Sleeswyk. Lüders band propagation at low velocities. *Acta Met.*, 21:pp1087, Aug (1973).

62. G.T. Van Rooyen. Basic factors which influence the Lüders strain during discontinuous yielding. *Mat. Sci. Eng.*, 7:37–48, 1971.

63. W.A. Spitzig and A.S. Keh. The role of internal and effective stresses in the plastic flow of iron single crystals. *Met. Trans. A*, 1:3325, 1970.

64. D.V. Wilson. Magnetic properties, internal strains and the Bauschinger effect in metals. *Nature*, 170:30–31, 1952.

65. G. Welter and S. Gockowski. The stress-strain diagram for mild steel. *Metallurgia*, pages 13–18, May 1938.

66. R. Wolfseher, J. Inhelder, and A.K. Helbling. System for the adaptation of tensile testing machines for executing torsional tests. *J. Test. Eval.*, 15(2):122–124, March 1987.

67. P. Messien and V. Leroy. Solute carbon and nitrogen in the ferrite after continuous annealing of low carbon low aluminium steels. *Steel Research*, 56:385–391, 1985.

68. J.M. Gere and S.P. Timoshenko. *Mechanics of Materials.* Van Nostrand Reinhold. Co., UK, Second edition, 1987.

69. American Society for Testing Materials, New York. *E 143, Standard Method for Shear Modulus at Room Temperature*, 1993.

70. J.E. Shigley. *Mechanical Engineering Design.* McGraw Hill Book Co., Singapore, First metric edition, 1986.

71. A.L. Window, editor. *Strain Gauge Technology.* Elsevier Applied Science, Essex, Second edition, 1989.

72. Agilent 34401a multimeter. Web site http://www.agilent.com /Top /English /index.html, 1998.

73. P. Horowitz and W. Hill. *The Art of Electronics.* Cambridge University Press, Cambridge, Second edition, 1990.

74. E.O. Doebelin. *Measurements Systems: Design and Applications.* McGraw-Hill Book Co., New York, 1966.

75. J.W. Dalley, W.F. Riley, and K.G. McConnell. *Experimental Measurements.* Wiley Scientific, 1984.

76. J.A Bailey. *Metals handbook*, Volume 12. American Society of Metals, New York, Ninth edition, 1985.

77. S.P. Timoshenko and J.M. Gere. *Theory of plastic stability.* McGraw-Hill Book Co., New York, Second edition, 1961.

78. Micro measurement typical standard strain gauge. Web site http://www.measurements group.com /guide /500 /gages /125tk.htm, 1998.

79. Mike Woodhead. Manserv, CSIR, Tel 349-1362. Private communication, 1998.

80. Marius Meiring. Manager, Machine shop, Iscor. Private communication, 1998.

81. Fabrizio Dononesius. Project manager, Defencetek, CSIR. Private communication, 2001.

82. H.W. Coleman and W.G. Steele. *Experimentation and uncertainty analysis for engineers*. John Wiley & Sons, New York, 1989.

83. G.F. Van der Voort. *Grain Size Measurement*. Practical Applications of Quantitative Metallography. American Society for Testing and Materials, USA, 1984.

84. A.H. Cottrell. The yield point in single crystals and polycrystalline metals. Technical report, Metallurgy Department, University of Birmingham, June 1951.

85. E.O. Hall. *Private communication to Cottrell in [84].*

86. T. Gladman and F.B.Pickering. *Effect of Grain Size on Mechanical Properties of Ferrous Materials*. Yield Flow and Fracture of Polycrystals. Applied Science Publishers, London, 1983.

87. P. Bidgood. Defencetek, CSIR. Private communication, 1998.

88. R.B. Tait. University of Capetown. Private communication, 2005.

89. C.F. Elam. *Distortion of metal crystals*. Clarendon Press, Oxford, 1935.

90. I. Schwartz. Metallurgy department, University of the Witwatersrand. Private communication, 1998.

Appendix A

Schmid factor simulations

A.1 Rationale

Schmid factor simulations were used to demonstrate the major slip systems in bcc using the Schmid criterion, and to illustrate the maximum Schmid factor as a function of grain orientation in bcc.

A.2 Schmid factor

Plastic deformation in single crystals takes place when the resolved shear stress (τ_{RSS}) acting on the slip plane in the slip direction reaches a critical value (refer to Figure 2.4). The term $\cos\phi\cos\lambda$ is known as the Schmid factor and slip systems that are oriented such as to have the highest Schmid factor will yield first [7].

In bcc iron, slip will occur in the $\langle 111 \rangle$ direction on the $\{110\}$ and $\{112\}$ planes as in Figure 2.3. Put another way, for a certain tensile axis the dislocations in the $\langle 111 \rangle$ and on the slip plane $\{110\}$ or $\{112\}$ with the greatest Schmid factor will move first.

A.3 Coding methodology

The aim of the program was to generate a surface of the largest Schmid factor (all $\langle 111 \rangle$ acting in the $\{110\}$ and $\{112\}$ planes) of all tensile axis orientations in the stereographic projection.

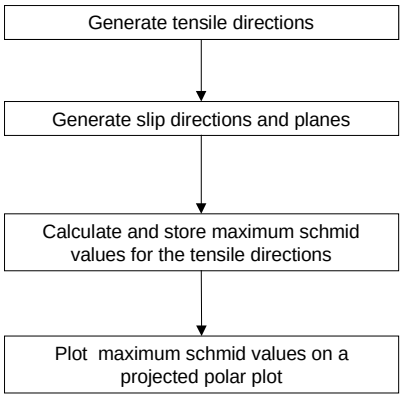

Figure A.1: General flow sheet for program.

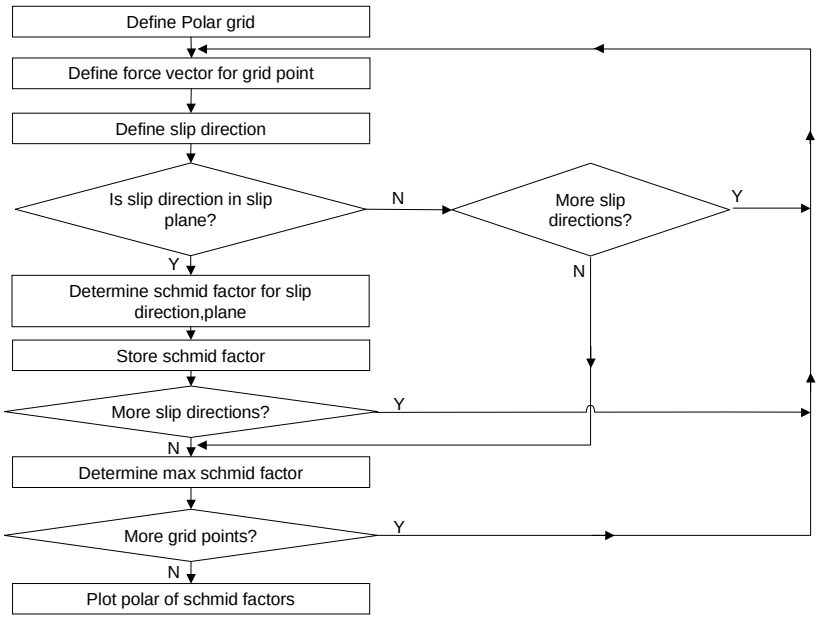

Figure A.2: Detailed flow sheet for program.

The flow sheet for the general programming is shown in Figure A.1 and the detail is in Figure A.2. The code was written by both A.S. Tuling and S Tuling.

A.4 Results and discussion

The result may be seen in Figure A.3. The same exercise was done for the fcc crystal to test the program (see Figure A.4), and the same result was achieved as published by Elam [89]

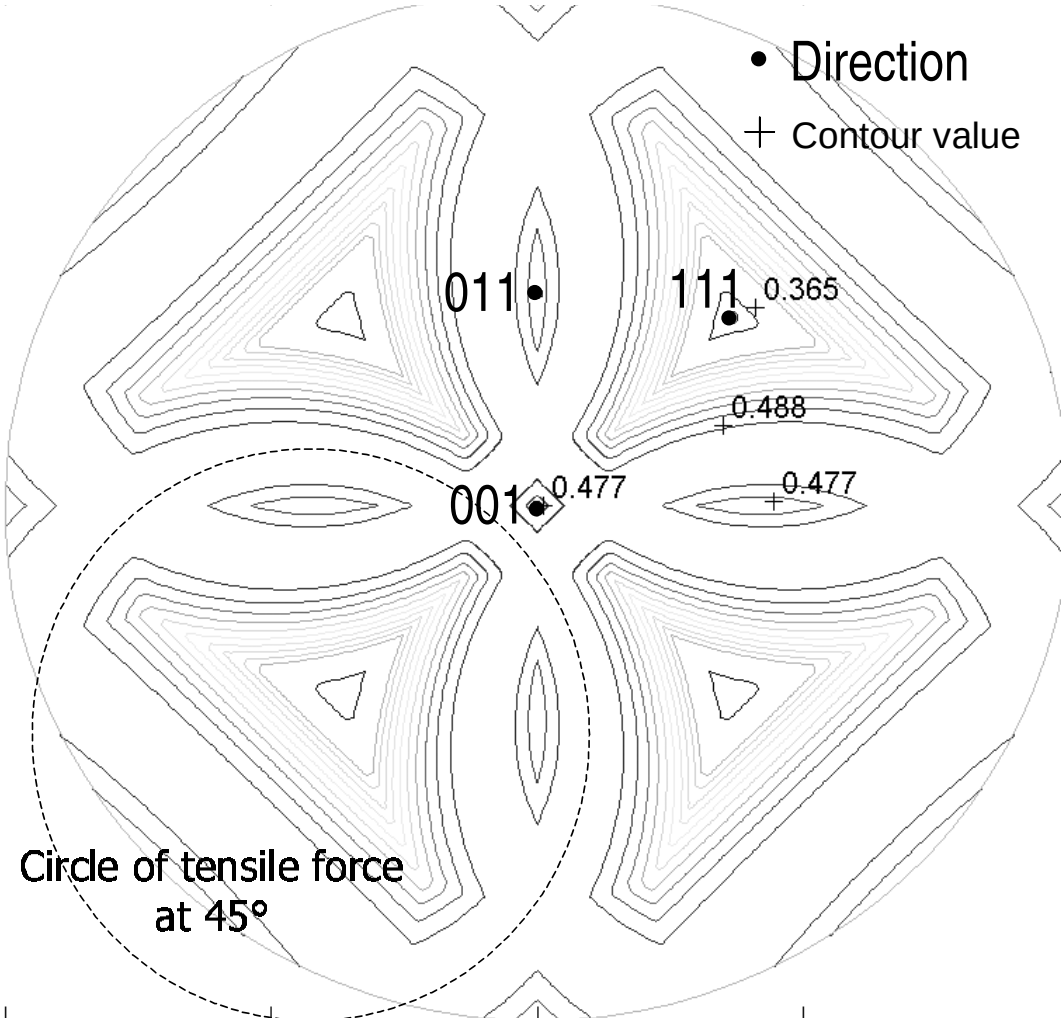

Figure A.3: Stereographic projection of Schmid factor contours for a bcc material.

It is seen that when the tensile force is at 45° to the ⟨111⟩ there is a maximum of the Schmid factor. When bcc material is being deformed, the planes at 45° to the ⟨111⟩ slip most easily, these will tend to rotate and become parallel to the stress

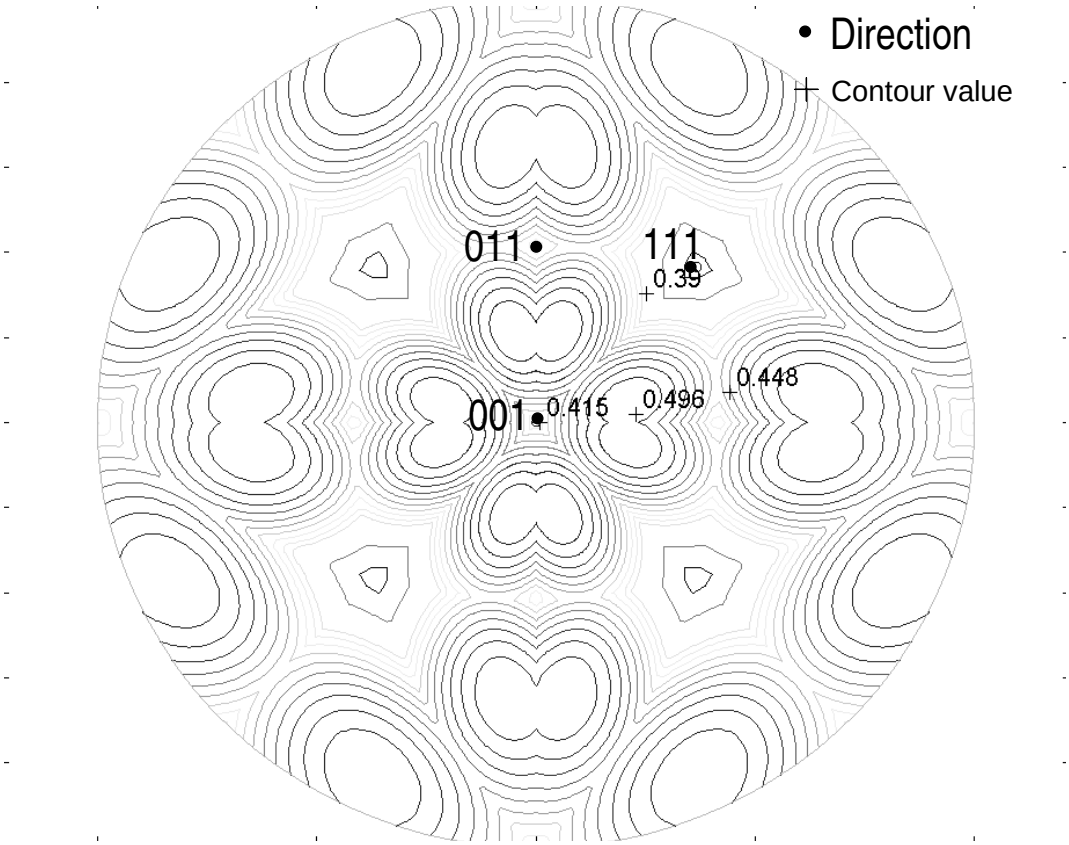

Figure A.4: Stereographic projection of Schmid factor contours for an fcc material.

while the ⟨111⟩ will tend to rotate so that it is at 45° to the tensile stress.

This Schmid factor simulation in bcc was a simple simulation with the assumption that the crystal has completely Schmid-like behaviour. Non-Schmid behaviour has not been included in the simulation, although it would be possible to include this, if the behaviour can be described mathematically.

A.5 Conclusion

The Schmid behaviour of the bcc crystal has been successfully simulated.

Appendix B

Experimental design details

B.1 Sample design

B.1.1 Hydrogen treatment

There was some concern that the anneal in hydrogen may result in unacceptable decarburisation. The Table B.1 details the composition of a bar heat treated in wet hydrogen. One side of the bar was coated in a Zirconium anti-oxidant coating, to try to establish the level of decarburisation in the sample. The heat treatment was as follows: rapid heat to 915°C, 5 minutes at 915°C, furnace cool to 700°C, air cool from 700°C.

Table B.1: Composition before (original) and after hydrogen treatment for Zirconium-coated and uncoated samples.

Element	Original composition	Uncoated side	Zirconium coated side
C	0.018	0.016	0.014
Mn	0.24	0.242	0.244
N	0.0025	0.004	0.0033

The amount of carbon lost in the wet hydrogen treatment was evaluated (by spark analysis) and carbon loss found to be around 0.002%. The error in the measurement is assumed to be 0.001%. From this result, it appears that zirconium decarburises the steel more effectively than the wet hydrogen treatment alone, although the decarburisation is not excessive.

B.1.2 Internal strain analysis of sample

The internal strain generated during torsion can be calculated. Consider torsion in a thin walled sample:

$$\tau = \frac{Tr}{I_p}$$

Where τ, T, I_p and r have their usual meanings. The stress in the material at the inner and outer radii (τ_i and τ_o for r_i and r_o respectively) is as follows:

$$\tau_i = \frac{Tr_i}{I_p}$$
$$\tau_o = \frac{Tr_o}{I_p}$$

The fractional stress differential between inner and outer radii is

$$\frac{\tau_o - \tau_i}{\tau_o} = 1 - \frac{r_i}{r_o}$$

For Elliot *et al.*'s work [3] where $r_i = 0.1732$ and $r_o = 0.815$,

$$\frac{\tau_o - \tau_i}{\tau_o} = 0.102$$

It can be concluded that even if there is a stress difference of 10%, upper yield is seen.

B.2 Strain measuring system

B.2.1 Clinometer investigation

This section details the investigation on two *Accustar* clinometers to determine the suitability of these instruments as troptometers. The clinometers were 'calibrated' by attaching a laser pointer to each clinometer and calculating the inclination angle by measuring the deviation of the laser beam. This is illustrated in Figure B.1. It was found that at some angles, the voltage reading on the clinometer took 60

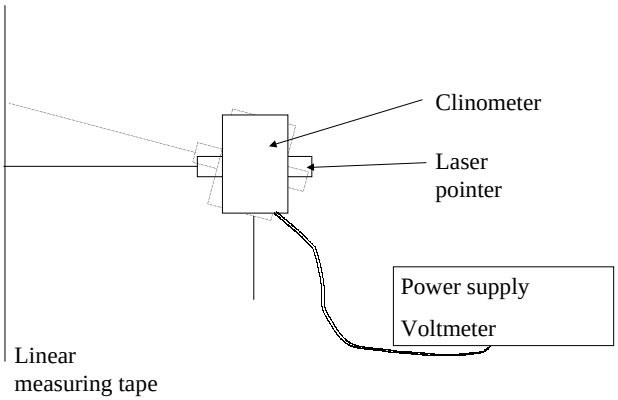

Figure B.1: Schematic of clinometer test.

seconds to settle. The results can be found in Figure B.2 and the difference between the readings and the laser reading are shown in Figure B.3.

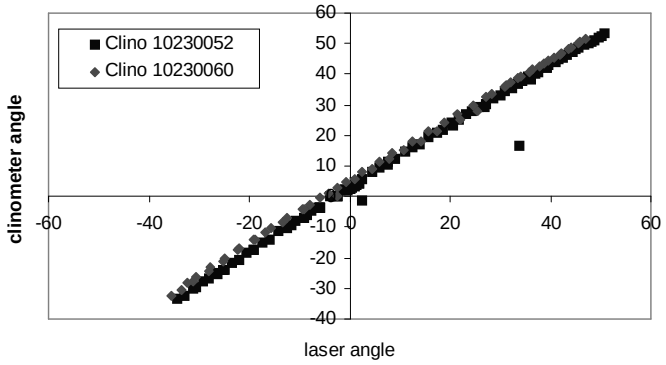

Figure B.2: Clinometer versus laser test, the axis units are degrees.

The clinometers' voltages are not reproducible (they deviate more than a degree),

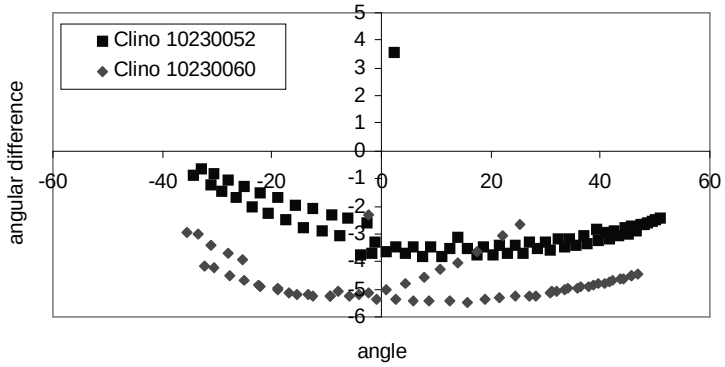

Figure B.3: Difference between clinometer angle and laser angle.

and thus the clinometers was discarded as a viable option.

B.2.2 Honeywell accelerometer specifications

Honeywell

Honeywell
Q-Flex® QA3000 Accelerometer
Highest inertial navigation-grade performance

For the highest inertial navigation-grade performance available in today's market, Honeywell produces the Q-Flex® QA3000. Built on the same production line as the industry-standard QA2000 Accelerometer, the QA3000 Accelerometer has the same inherent quality, reliability, and long-term performance characteristics of the QA2000 Accelerometer. Primary applications include spacecraft navigation and control systems.

As with the entire Q-Flex family of accelerometers, the QA3000 features a patented Q-Flex etched-quartz-flexure seismic system. An amorphous quartz proofmass structure provides excellent bias, scale factor, and axis alignment stability.

The integral electronics develops an acceleration-proportional output current providing both static and dynamic acceleration measurement. By use of a customer supplied output load resistor, appropriately scaled for the acceleration range of the application, the output current can be converted into a voltage.

The QA3000 also includes a current-output, internal temperature sensor. By applying temperature-compensating algorithms, bias, scale factor, and axis misalignment performance are dramatically improved.

Features

- Highest performance accelerometer available
- Excellent turn-on repeatability and stability performance
- Environmentally rugged
- Analog output
- Field-adjustable range
- Three fastener precision mounting flange
- Internal temperature sensor for thermal compensation
- Dual built-in test

Accelerometers exported from the United States must be done in accordance with the Export Administration Regulations (EAR) and/or the International Traffic in Arms Regulations (ITAR) as applicable. EXP029, March 2004

Configuration Drawings

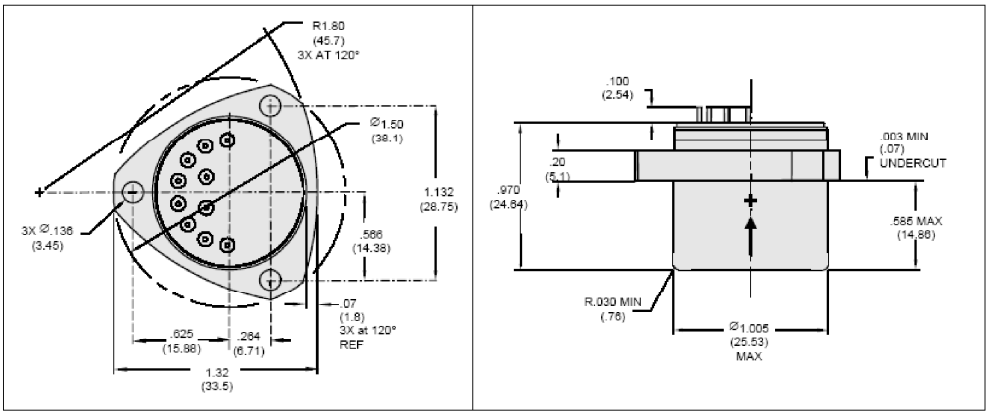

Performance Characteristics

Additional product specifications, outline drawings and block diagrams, and test data are available on request.

Performance	**QA3000-030**	**QA3000-020**	**QA3000-010**
Input Range [g]	±60	±60	±60
Bias [mg]	<4	<4	<4
One-year Composite repeatability [µg]	<40	<80	<125
Temperature Sensitivity [µg/ºC]	<15	<15	<25
Scale Factor [mA/g]	1.20 to 1.46	1.20 to 1.46	1.20 to 1.46
One-year Composite Repeatability [ppm]	<80	<160	<250
Temperature Sensitivity [ppm/ºC]	<120	<120	<120
Axis Misalignment [µrad]	<1000	<1000	<1500
One-year Composite Repeatability [µrad]	<70	<80	<100
Vibration Rectification [µg/g^{2}rms]	<10 (50-500 Hz)	<15 (50-500 Hz)	<20 (50-500 Hz)
	<35 (500-2000 Hz)	<40 (500-2000 Hz)	<50 (500-2000 Hz)
Intrinsic Noise [µg-rms]	<7 (0-10 Hz) <7 (10-500 Hz) <1500 (500-10,000 Hz)	<7 (0-10 Hz) <70 (10-500 Hz) <1500 (500-10,000 Hz)	<7 (0-10 Hz) <70 (10-500 Hz) <1500 (500-10,000 Hz)
Environment	**QA3000-030**	**QA3000-020**	**QA3000-010**
Operating Temperature Range [ºC]	-28 to +78	-55 to +95	-55 to +95
Shock [g]	100	150	150
Vibration Peak Sine [g]	15 @ 20-2000 Hz	15 @ 20-2000 Hz	15 @ 20-2000 Hz
Resolution/Threshold [µg]	<1	<1	<1
Bandwidth [Hz]	>300	>300	>300
Thermal Modeling	**QA3000-030**	**QA3000-020**	**QA3000-010**
	YES	YES	YES
Electrical	**QA3000-030**	**QA3000-020**	**QA3000-010**
Quiescent Current per Supply [mA]	<16	<16	<16
Quiescent Power [mW] @ ±15 VDC	<480	<480	<480
Electrical Interface	Temp Sensor	Temp Sensor	Temp Sensor
	Voltage Self Test	Voltage Self Test	Voltage Self Test
	Current Self Test	Current Self Test	Current Self Test
	Power / Signal Ground	Power / Signal Ground	Power / Signal Ground
	-10 VDC Output +10 VDC Output	-10 VDC Output +10 VDC Output	-10 VDC Output +10 VDC Output
Input Voltage [VDC]	±13 to ±28	±13 to ±28	±13 to ±28
Physical	**QA3000-030**	**QA3000-020**	**QA3000-010**
Weight [grams]	71± 4	71± 4	71± 4
Diameter below mounting surface [inches]	Ø1.005 Max	Ø1.005 Max	Ø1.005 Max
Height - bottom to mounting surface [inches]	.585 Max	.585 Max	.585 Max
Case Material	300 Series Stainless Steel	300 Series Stainless Steel	300 Series Stainless Steel

ISO-9001 Certification Since 1995

For more information, please visit www.inertialsensor.com
Or contact:
Honeywell International, Inc.
Defense and Space Electronic Systems Redmond
15001 N.E. 36th Street
Redmond, Washington 98073-9701
PHONE: 888 206 1667 or FAX: 425 883 2104

Honeywell

B.3 Torque measuring system

B.3.1 Strain gauges and gauge factor, k

A strain gauge is essentially a resistor. As the gauge is stretched, its length L changes by dL, the resistance R changes by dR. The ratio of the of the strain to the resistance change is the gauge factor, k. Mathematically:

$$k = \frac{dR/R}{dL/L}. \tag{B.1}$$

This is related to the material of the strain gauge as follows

$$k = 1 + 2\nu + \pi_i E, \tag{B.2}$$

where ν π_i, E are Poisson's ratio, the longitudinal piezoresistance coefficient and the Young's modulus, respectively. The first term accounts for the length change, the second to the change in area and the third to piezoresistive effects. Piezoresistance effects are small for metals and large for semiconductors [74, page 225]. The gauge factor is independent of the resistance.

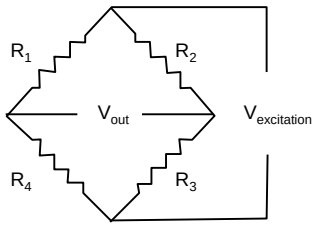

Figure B.4: Wheatstone bridge arrangement of strain gauges.

The output voltage V_{out}, on a full Wheatstone bridge (Figure B.4), is as follows:

$$\frac{V_{out}}{V_{excitation}} = \frac{R_1 + \Delta R_1}{R_1 + \Delta R_1 + R_2 + \Delta R_2} - \frac{R_4 + \Delta R_4}{R_3 + \Delta R_3 + R_4 + \Delta R_4}.$$

Assuming the fractional change in resistance is in the region of 10^{-3},

$$\frac{V_{out}}{V_{excitation}} \approx \frac{1}{4}\left(\frac{\Delta R_1}{R_1} - \frac{-\Delta R_2}{R_2} + \frac{\Delta R_3}{R_3} - \frac{\Delta R_4}{R_4}\right).$$

In a full strain gauge bridge, in torsion $\Delta R_1 + \Delta R_2 = 0$ and $\Delta R_3 + \Delta R_4 = 0$, then

$$\frac{V_{out}}{V_{excitation}} \approx \frac{\Delta R_1 - (-\Delta R_1) + \Delta R_1 - (-\Delta R_1)}{4R}$$

$$\text{So } V_{out} = V_{excitation}\frac{\Delta R}{R},$$

where $V_{excitation}$ is the excitation voltage on the strain gauge circuit and $\Delta R/R$ is the ratio of the change in resistance to the original resistance in the strain gauges.

$$V_{out} = V_{excitation}\epsilon k \tag{B.3}$$

$V_{excitation}$ is usually limited by the amount of power that can be dissipated in the gauge. It is desirable to maintain the strain gauge temperature close to ambient to prevent drift in the measurements (because there is power generated in the gauge). The power dissipated a gauge, P_{gauge}, is

$$P_{gauge} = \frac{V_{excitation}^2}{4R}.$$

The power density in the gauge, P' is the power per unit area:

$$P' = \frac{P_{gauge}}{A},$$

where A is the gauge area (the gauge is usually a grid of parallel foil wires), and is calculated by multiplying the active gauge length by the grid width. Combining these two equations

$$V_{excitation} = 2\sqrt{RP'A}. \tag{B.4}$$

Substituting this into B.3

$$V_{out} = 2\sqrt{RP'A}\epsilon k. \tag{B.5}$$

According to Doeblin[74], the smallest detectable strain is limited by the noise from thermal or Johnson noise. This range should be avoided and this is dealt with in the following section.

B.3.2 Derivation of thin tube limit

In the design, the approximation of thin-walled tube is used in calculating the polar moment of inertia. The actual monment of inertia, $I_{p\ actual}$ is:

$$I_{p\ actual} = \frac{\pi}{2}(r_o^4 - r_i^4), \tag{B.6}$$

Where r_o and r_i are outer radius and inner radius respectively.

The approximate thin-walled moment of inertia is:

$$I_{p\ thin} = 2\pi r^3 t \tag{B.7}$$

where r, t are the average radius and thickness.

In the design, t and r are free, and a limit must be set on these to keep the approximation valid. Consider a fractional inaccuracy of f_{approx}, so that

$$\begin{aligned} f_{approx} &= \frac{I_{p\ actual} - I_{p\ thin}}{I_{p\ actual}} \\ &= \frac{\frac{\pi}{2}(r_o^4 - r_i^4) - 2\pi r^3 t}{\frac{\pi}{2}(r_o^4 - r_i^4)}, \end{aligned} \tag{B.8}$$

where $I_{p\ actual}$ is the actual polar moment of inertia and $I_{p\ thin}$ is the thin wall approximation to the thin-walled cylinder. Considering the relationship between average radius, thickness, outer radius and inner radius (r, t, r_o and r_i); $r = \frac{r_o + r_i}{2}$ and $t = r_o - r_i$:

$$\begin{aligned} f_{approx} &= \frac{(r_o^2 + r_i^2)(r_o + r_i)(r_o - r_i) - \frac{1}{2}(r_o - r_i)(r_o + r_i)(r_o^2 + 2r_o r_i + r_i^2)}{(r_o^2 + r_i^2)(r_o + r_i)(r_o - r_i)} \\ 2f_{approx} &= \frac{(r_o - r_i)^2}{r_o^2 + r_i^2}. \end{aligned} \tag{B.9}$$

Re-using the relationship between r, t, r_o and r_i with $r_o = r + \frac{1}{2}t$, $r_i = r - \frac{1}{2}t$ and $t = r_o - r_i$,

$$\begin{aligned} 2f_{approx} &= \frac{t^2}{r^2 + rt + \frac{1}{4}t^2 + r^2 - rt + \frac{1}{4}t^2} \\ &= \frac{t^2}{2r^2 + \frac{1}{2}t^2}, \end{aligned} \tag{B.10}$$

or

$$t = \left(\frac{4f_{approx}}{1 - f_{approx}}\right)^{\frac{1}{2}} r. \tag{B.11}$$

For the design $f_{approx} \leq 0.05$ is considered so that $t \leq 0.46r$.

B.3.3 Limits of sensitivity in strain gauges and associated systems

Theoretical errors

There are uncertainties that the user of strain gauges cannot eliminate, the most important being electronic noise (an 'intrinsic' uncertainty). A convenient estimate of noise is the signal to noise ratio (SNR) [73]

$$\text{SNR} = 10 \log_{10}\left(\frac{V_s^2}{V_n^2}\right), \tag{B.12}$$

where the signal and noise voltages (V_s and V_n) are rms values and SNR is measured in dB. It is also important to quote the bandwidth and central frequency at which the noise is measured. It may be of some merit to discuss these on a theoretical level. Electronic noise(s) will affect all the electronic parts in the strain gauge system. There are four main types.

1. Thermal noise (Johnson noise)
2. Shot noise
3. $1/f$ noise (flicker noise)
4. Interference.

The first, thermal noise, is a white noise that has a flat frequency spectrum, meaning that there is the same power in each unit of frequency range. This noise, $V_{rms\ noise}$, is caused by the random motion of electrons in any resistor and is defined as:

$$V_{rms\ noise} = \sqrt{4\kappa \mathrm{T} R \Delta f}, \tag{B.13}$$

where κ is the Boltzmann constant, T is the absolute temperature, R is the resistance and Δf is the bandwidth of a 'perfectly engineered' voltmeter. Taking the ratio of output signal (Equation B.5) to noise (Equation B.13), an evaluation of the factors that can improve the ratio can be performed:

$$\frac{V_{out}}{V_{rms\ noise}} = \frac{V_{excitation}\epsilon k}{\sqrt{4kTR\Delta f}} \tag{B.14}$$

$$= \frac{V_{excitation}\epsilon(1+2\nu+\pi_i E)}{\sqrt{4kTR\Delta f}} \tag{B.15}$$

$$= \sqrt{\frac{P'A}{kT\Delta f}}\epsilon(1+2\nu+\pi_i E). \tag{B.16}$$

A 'typical' strain gauge for measuring the strain from pure torsion (strain gauge catalogue number HBM XY21) is considered. It has dimensions of 17.5 × 12.7mm, a resistance of 350Ω and a maximum excitation voltage of 21V. The noise as measured by an 'off the shelf' voltmeter with frequency range of 1kHz would be:

$$\begin{aligned} V_{rms\ noise} &= \sqrt{4kTR\Delta f} \\ &= \sqrt{4\ 1.38\times10^{-23}\ 293\ 350\ 1000} \\ &= 75nV. \end{aligned}$$

The same 'off the shelf voltmeter' will only be able to measure to 0.1mV. Accurate voltmeters are able to measure to around 1 μV. Thus, in practice, this noise is much smaller than the measurement capabilities of the system. However, other sources of noise (e.g. lead impedances, transistors, other resistances) also limit the system resolution [74].

The second noise, shot noise, is associated with the current in the component. Since current is a flow of discrete electrical charges, this leads to statistical fluctuations in the current. In a metallic conductor, this type of noise is lower than predicted as there are long range correlations between charge carriers [73]. $I_{rms\ noise} = 6.8$nA for the experimental setup under consideration (where $I_{dc} = 14$mA) and can thus be ignored.

The third noise type, flicker noise, is an 'excess' noise. Resistors suffer from fluctuations in resistance, which depend on many factors including the construction, material and end-cap connections of the device. This type of noise has approximately $1/frequency$ spectrum (a pink noise) [73]. Metal films have a flicker noise of $0.02 - 0.2\mu V$ per volt applied across the resistor, measured over a decade of frequency (the ratio of upper frequency to lower frequency is 10)[73]. For this system, this equates to a noise of 1.4μV, which is also negligible.

Finally, interference must be dealt with. The characteristics of the noise obviously depend on the source. Sources would include lighting, electro-magnetic frequency broadcasting, nearby electrical equipment, motors, CRT (cathode ray tubes). Many of these sources can be eliminated by careful shielding and filtering, but at other times it is not possible to effectively shield components and 'draconian measures' must be taken [73]. A strain gauge is effectively an antenna; this is why smaller gauges with closer grid lines are 'quieter'. Shielding can protect a gauge from electrostatic interference, while electromagnetic interference can be dealt with by placing two grids exactly on top of each other, although this reduces the strain sensitivity. Leads may be electrostatically shielded by either driven or passive shields, and common mode rejection can be performed on the signal to eliminate electromagnetic interference. Most of these problems are not expected, but cognisance of the interference potential was taken.

Possible practical errors

There are a large number of factors which influence a strain gauge's sensitivity and lead to error. Pople [71] draws four broad categories (with many details); the progression also shows the increase in uncertainty as potential errors accumulate:

The errors possible in this application/design are:

1. Gauge system and its environment
   (a) The gauge factor on a gauge can change with excessive loads, that why the maximum strain is important. Also, designing the system within the strain gauge fatigue limits (as quoted by the manufacturer) is important.
   (b) The strain transmission characteristics will be altered if the adhesive is cured for insufficient time, or it is poorly glued, and if there are inclusions or voids in the glue line.
   (c) The protective coating must prevent corrosion of grid or solder connections.
   (d) With changes in ambient temperature, the gauge factor varies so that ideally the environment should be a constant temperature. Electromagnetic and electrostatic fields can affect the gauge.
2. In the signal acquisition, joints, connections and leads can generate thermal emfs. Leads can also 'pick up' noise.
3. The system readout might be affected by the stability of the voltage supply and the resolution and linearity of the signal conditioning, and signal processing, as well as pick up in electromagnetic and electrostatic fields.
4. Finally, errors are associated with gauge misalignment.

The point of this list is only this: a great deal of time could go into the theoretical analysis of errors and uncertainties, but, as with all practical solutions, only a little of the uncertainty can be accounted for theoretically, and for the most part, the errors are estimated empirically - back to good old experience. Of course that is unless resources are not a problem and the ideal equipment is available.

All that is required from the torque tube designer's view point is the reading value and the uncertainty in any reading value (the 'goodness of the reading'). The latter

is the effective resolution (as found in practical strain gauging) of the system (the practical resolution can be defined as the smallest meaningful discernable difference between two values). Some books on the subject[71], predict that a novice, using strain gauges in average test conditions is liable to produce an uncertainty in the region of ±7-14% and give a maximum value of 0.1 microstrain. This is approximately 0.001 ± 0.0001. Workers with much experience in applying strain gauges give a practical strain resolution limit of 10^{-5} (an indication of the uncertainty), but shirk at giving an uncertainty [87].

B.3.4 Design of packed torque tube, n = max design

If close packing of the gauges is assumed, the dimensions (r, l) of the torque tube are related to the area of a single gauge as follows:

$$\begin{aligned} 2\pi rl &= 4nA_{gauge} \quad where\ n = 1, 2, 3.... \\ A_{gauge} &= \frac{\pi rl}{2n}. \end{aligned} \tag{B.17}$$

When the area of the tube with strain gauges is covered, the permissible power dissipation of each gauge will decrease. This will reduce the maximum allowed power, P' and alter the sensitivity (Equation 4.25). Thus when many gauges are packed together, then P' will be called P'_{packed} and with isolated gauges P' will be called $P'_{isolated}$, where

$$P'_{packed} < P'_{isolated}. \tag{B.18}$$

If the gauges are packed close together, the heat dissipation pattern is modified, and the maximum permissable dissipation by each gauge is reduced.

It will be assumed that the packed scenario will be similar to the approximation in Figure B.5. It is assumed that most of the heat is lost to the area a gauge length away from the gauge. It will be assumed that there is an effective gauge radius, $R_{\text{effective}}$. The ratio of power distributions could be estimated as

$$\begin{aligned} \frac{P'_{packed}}{P'_{isolated}} &\propto \frac{\pi R^2_{\text{effective}}}{\pi(2R_{\text{effective}})^2} \\ &\propto \frac{1}{4}, \end{aligned} \tag{B.19}$$

so that P'_{packed} is 25% of the value given for separate gauges.

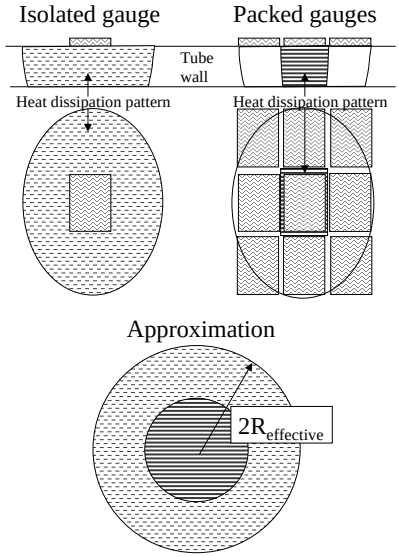

Figure B.5: Heat dissipation for isolated and close-packed gauges.

Substituting Equation B.17 into Equation 4.25 and using P'_{packed}, the sensitivity becomes

$$\text{Sensitivity} \quad = \quad \frac{k}{2Gt}\left(\frac{nRP'_{packed}l}{2\pi r^3}\right)^{\frac{1}{2}}. \tag{B.20}$$

Re-substituting Equation B.17:

$$\text{Sensitivity} \quad = \quad \frac{kl}{4Grt}\left(\frac{RP'_{packed}}{A_{gauge}}\right)^{\frac{1}{2}}. \tag{B.21}$$

Consider both sensitivity and stiffness relationships (Equations B.21, 4.35):

$$\text{Sensitivity} \quad \propto \quad \frac{l}{Grt}, \tag{B.22}$$

$$\text{Stiffness} \quad \propto \quad \frac{Gr^3t}{l}. \tag{B.23}$$

Both sensitivity and stiffness must be maximized (Equations B.22, and B.23). Thus,

$$x \quad = \quad \frac{l}{Grt} \tag{B.24}$$

and substitute this into Equations B.22, and B.23:

$$\text{Sensitivity} \quad \propto \quad x \tag{B.25}$$

and

$$\text{Stiffness} \quad \propto \quad \frac{r^2}{x}. \tag{B.26}$$

It follows that sensitivity can be increased without limit by increasing x, and thereafter increase stiffness without limit by increasing r at constant x. This would mean that it is desirable to increase l, or decrease t or to a limited extent G. This implies an 'air-ship' design, made of a material with a low shear modulus (for instance aluminum would be more suitable than steel). However, considerations of strength must also be added.

Packed torque tube design with sensitivity and stiffness limits (n = max)

In practice, it is possible to decide on the minimum acceptable stiffness and sensitivity and thereby obtain the minimum radius. Referring to Equation B.21, if the sensitivity is defined to be above a certain level, say S_0, then,

$$\begin{aligned} \frac{kl}{4Grt}\left(\frac{RP'_{packed}}{A_{gauge}}\right)^{\frac{1}{2}} &\geq S_0, \\ \text{so that, } \frac{l}{t} &\geq \frac{4S_0Gr}{k}\left(\frac{A_{gauge}}{RP'_{packed}}\right)^{\frac{1}{2}}. \end{aligned} \tag{B.27}$$

Referring to Equation 4.35, if the stiffness is required to be greater than or equal to Σ_0:

$$\begin{aligned} \frac{2\pi Gr^3t}{l} &\geq \Sigma_0 \\ \text{so that, } \frac{l}{t} &\leq \frac{2\pi Gr^3}{\Sigma_0}. \end{aligned} \tag{B.28}$$

Combining Inequalities B.27 and B.28,

$$\frac{S_0 4A_{gauge}^{\frac{1}{2}}Gr}{kR^{\frac{1}{2}}{P'_{packed}}^{\frac{1}{2}}} \leq \frac{2\pi Gr^3}{\Sigma_0},$$

so that

$$r^2 \geq \frac{2S_0\Sigma_0 A_{gauge}^{\frac{1}{2}}}{\pi kR^{\frac{1}{2}}{P'_{packed}}^{\frac{1}{2}}} \tag{B.29}$$

$$\text{and } \frac{l}{t} \geq \frac{S_0^{\frac{3}{2}}\Sigma_0^{\frac{1}{2}}G}{2^{\frac{1}{2}}\pi^{\frac{1}{2}}k^{\frac{3}{2}}R^{\frac{1}{4}}{P'_{packed}}^{\frac{1}{4}}}. \tag{B.30}$$

From the Inequality B.29, it is observed that a minimum radius is required, while from inequality B.30, a minimum $\frac{l}{t}$ is required to meet the combined stiffness, sensitivity limits. This can also be seen in Figure B.6 where Inequalities B.27 and B.28

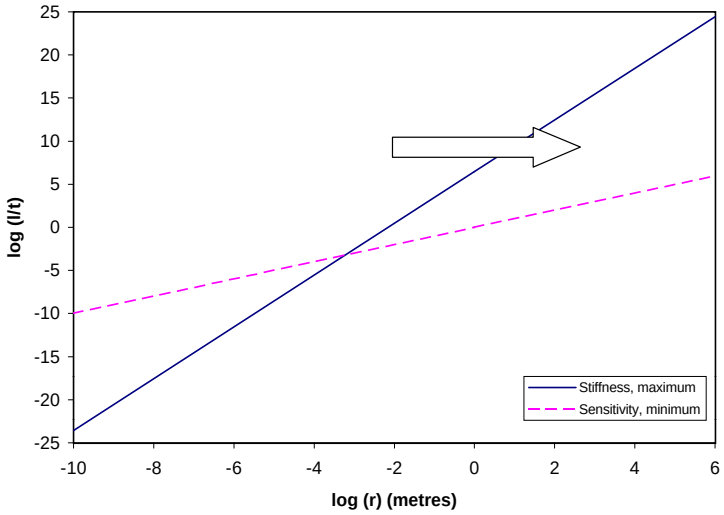

Figure B.6: Sensitivity and Stiffness functions for design with n=max sets of gauges, where the indicated area meets both requirements (dimensions in metres).

are plotted. From Equation B.29, the design can proceed by considering r and l/t equal to or greater than those values, and completing the design within the buckling and strain limits, which are discussed below.

Mechanical strength requirements for packed (n = max) design

The mechanical strength requirements are the same as derived for the n = 1 case (Equations 4.47, 4.48) and they will not alter:

$$r^2 t \geq \frac{T_{max} s}{2\pi\tau_y} \tag{B.31}$$

$$T_{\substack{crit,\ s \\ short}} \leq 8.78 \frac{\pi E t^3 r^2}{(1-\nu^2) l^2} \left(1 + 0.0257(1-\nu^2)^{\frac{3}{4}} \left(\frac{l}{r^{\frac{1}{2}} t^{\frac{1}{2}}}\right)^3\right)^{\frac{1}{2}}. \tag{B.32}$$

Packed (n = max) design: Graphical representation for the theoretical considerations

Using the same axes as for the sensitivity and stiffness Inequalities (Figure B.6) all four inequalities can be plotted on one graph (Figure B.8). The inequalities will be plotted in the form $\log(r),\ \log\left(\frac{l}{t}\right)$, the Equations 4.47, and 4.48 will be contours of $\log(l)$ in the plane of $\log(r),\ \log\left(\frac{l}{t}\right)$ as follows:

Sensitivity, from Equation B.27 is a line of minimum allowable $\log\left(\frac{l}{t}\right)$

$$\log\left(\frac{l}{t}\right) \quad \geq \quad \log(r) + \log\left(\frac{4S_0 A_{gauge}^{\frac{1}{2}} G}{kR^{\frac{1}{2}} P'^{\frac{1}{2}}_{packed}}\right), \tag{B.33}$$

omitting the thin tube assumption (Equation 4.19).

Stiffness, from Equation B.28 is a line of maximum allowable $\log\left(\frac{l}{t}\right)$

$$\log\left(\frac{l}{t}\right) \quad \leq \quad 3\log(r) + \log\left(\frac{2\pi G}{\Sigma_0}\right). \tag{B.34}$$

Maximum torque, from Equation 4.47 is a contour plot, showing minimum values of $\log(l)$ for given values of $\log(r)$ and $\log\left(\frac{l}{t}\right)$

$$\log(l) \quad \geq \quad \log\left(\frac{l}{t}\right) - 2\log(r) + \log\frac{T_{max} s}{2\pi\tau_y}. \tag{B.35}$$

Buckling, from Equation 4.48, is a contour plot, showing minimum values of $\log(l)$ for given values of $\log(r)$ and $\log\left(\frac{l}{t}\right)$. Since it is an implicit inequality, a numerical solution was found for each $\log(l)$ using chosen values of $\log(r)$ and $\log\left(\frac{l}{t}\right)$, by transforming Equation 4.48 to the following equation:

$$\left(\frac{8.78\pi E}{(1-\nu^2)T_{\substack{crit,\ s\\ short}}}\right) r^2 l \left(\frac{l}{t}\right)^{-3} \sqrt{1 + 0.0257(1-\nu^2)^{\frac{3}{4}} \left(\frac{l}{t}\right)^{\frac{3}{2}} l^{\frac{3}{2}} r^{\frac{-3}{2}}} \quad = \quad 1. \tag{B.36}$$

The numerical values of the required sensitivity and stiffness will be as for the case of the n=1 design.

The graphs of sensitivity and stiffness, buckling and mechanical limits may now be plotted. Taking the buckling and torque criterion first; the lines represent contours of $\log(l)$ with the figures on the lines indicating the values of $\log(l)$ in metric units. These are plotted separately for clarity in Figure B.7.

The buckling and mechanical failure criteria are combined into one surface of minimum $\log(l)$, and superimposed onto the stiffness and sensitivity equations (which are planes perpendicular to axes of $\log(r)$, $\log(\frac{l}{t})$) in Figure B.8. This defines the allowable designs, and the practical criteria can now be considered. The practical limits will be as before from Section 4.5.4 (Design with peripheral (practical) considerations)

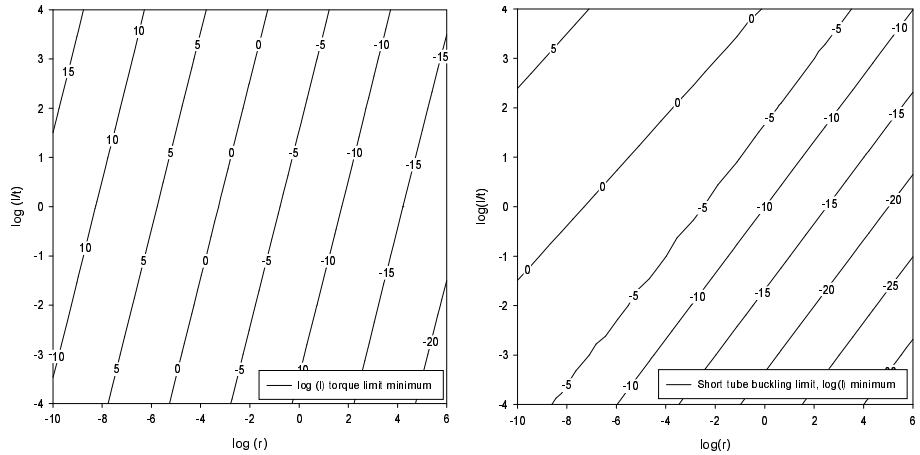

Figure B.7: Theoretical torque (left) and buckling (right) contours for design with n max, all dimensions in metres.

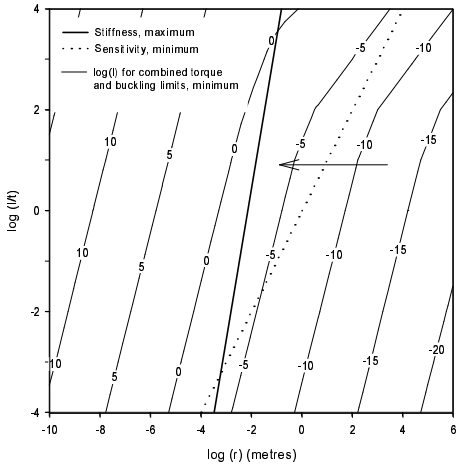

Figure B.8: Theoretical buckling and torque contours ($\log(l)$(metres)) with stiffness, sensitivity and minimum radius criteria for n max, all dimensions in metres. Arrow indicates the allowable design in the area between stiffness and sensitivity limits.

Strain gauge fatigue from Equation 4.60:

$$\log(t) \quad \geq \quad -2\log(r) + \log\left(\frac{T_{max}}{2\pi G \epsilon_f}\right). \tag{B.37}$$

Machining from Equation 4.61:

$$\log(t) \quad \geq \quad \log(t_m). \tag{B.38}$$

Gauge length is

$$\log(l) \quad = \quad \log(l_{gauge}). \tag{B.39}$$

In the case of the n max design, the cost of the design can be reduced by reducing the area so that as few strain gauges as possible are applied, while still satisfying all the prescribed ideal, mechanical and practical requirements. This would require a minimum area (assuming ideal packing) of

$$2\pi r l \quad = \quad 4n A_{gauge}. \tag{B.40}$$

The result has the same implication (cover the area) as Equation B.17, and, more importantly, since n must be an integer, this equation limits the radius and length to multiples of n and the gauge dimensions.

Summary of all equations for packed strain gauges (n = max design)

This is a summary of all equations, practical and theoretical so that all the equations may be represented on one graph. The prescribed, ideal criteria are sensitivity and stiffness:
Sensitivity is defined by Equation B.27, and is plotted in Figure B.6:

$$\log\left(\frac{l}{t}\right) \quad \geq \quad \log(r) + \log\left(\frac{4 S_0 \ {A_{gauge}}^{\frac{1}{2}} G}{k R^{\frac{1}{2}} {P'}^{\frac{1}{2}}_{packed}}\right). \tag{B.41}$$

Stiffness is calculated from Equation B.28, and is plotted in Figure B.6:

$$\log\left(\frac{l}{t}\right) \quad \leq \quad 3\log(r) + \log\left(\frac{2\pi G}{\Sigma_0}\right), \tag{B.42}$$

with Equation 4.19 to keep the design within the thin-walled criterion:

$$\log\left(\frac{l}{t}\right) \quad \leq \quad \log(r) - \log(t) + \frac{1}{2}\log\left(\frac{4 f_{approx}}{1 - f_{approx}}\right). \tag{B.43}$$

Following the ideal criteria are the mechanical stability criteria (torque, buckling), with safety factors:
Maximum torque is calculated from Equation 4.47 and is plotted in Figure B.7:

$$\log l \quad \geq \quad +\log\left(\frac{l}{t}\right) - 2\log(r) + \log\frac{T_{max}s}{2\pi\tau_y}. \tag{B.44}$$

Buckling is calculated from Equation 4.48, and is plotted in Figure B.7, which is a numerical solution for:

$$0 = \left(\frac{8.78\pi E}{(1-\nu^2)T_{\substack{crit,\\ short}}\, s}\right) r^2 l \left(\frac{l}{t}\right)^{-3} \left(1 + 0.0257(1-\nu^2)^{\frac{3}{4}} \left(\frac{l}{t}\right)^{\frac{3}{2}} l^{\frac{3}{2}} r^{\frac{-3}{2}}\right)^{\frac{1}{2}} - 1. \tag{B.45}$$

Finally the practical criteria include fatigue limits, machining limits, gauge length and cost.
Strain gauge fatigue is calculated from Equation 4.60, and is plotted in Figure B.9:

$$\log(l) \quad \geq \quad +\log\left(\frac{l}{t}\right) - 2\log(r) + \log\frac{T_{max}}{2\pi G\epsilon_f}. \tag{B.46}$$

The machining limit is given by Equation 4.61, and is plotted in Figure B.10:

$$\log(l) \quad \geq \quad \log\left(\frac{l}{t}\right) + \log(t_m). \tag{B.47}$$

The minimum gauge length is given by Equation 4.62, this is a flat plane in the log(r) and log(l/t):

$$\log(l) \quad \geq \quad \log(l_{gauge}). \tag{B.48}$$

The minimized strain gauge cost can be found in Equation B.40:

$$\log(l) = \log(\frac{2nA_{gauge}}{\pi}) - \log(r). \tag{B.49}$$

As before, the contours will be plotted separately for clarity; stiffness and sensitivity criteria may be seen in Figure B.6, the mechanical and buckling criteria in Figure B.7, strain gauge fatigue in Figure B.9 and machining limit in Figure B.10. The minimization of the cost will be discussed later.

Plotting all the surfaces, the 'shape' of the function that fulfills all the criteria may be found. Note that buckling and torque, fatigue, machining thickness and length are minima (thus only one is the minimum limit at any instance of r, l/t, l). Figure B.11 shows the greatest of these minima.

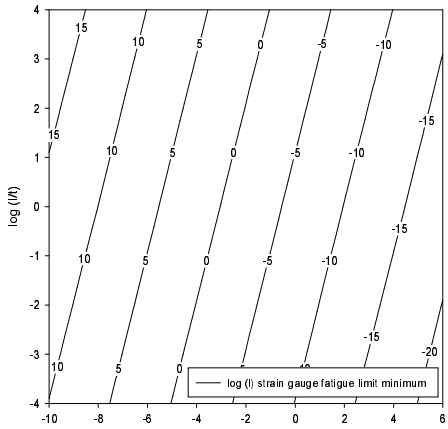

Figure B.9: Contours of fatigue life criterion for packed strain-gauge design (n max), all dimensions in log metres.

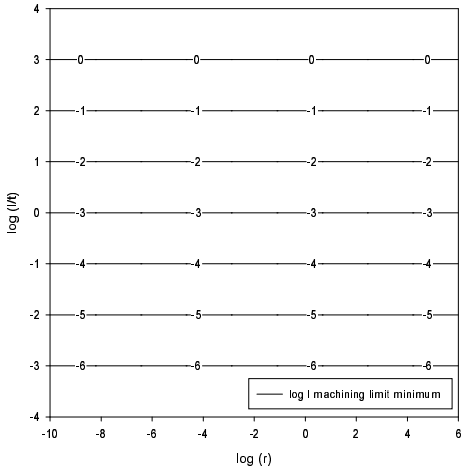

Figure B.10: Contours of practical machining limit for many-strain-gauge design (n max), all dimensions in log metres.

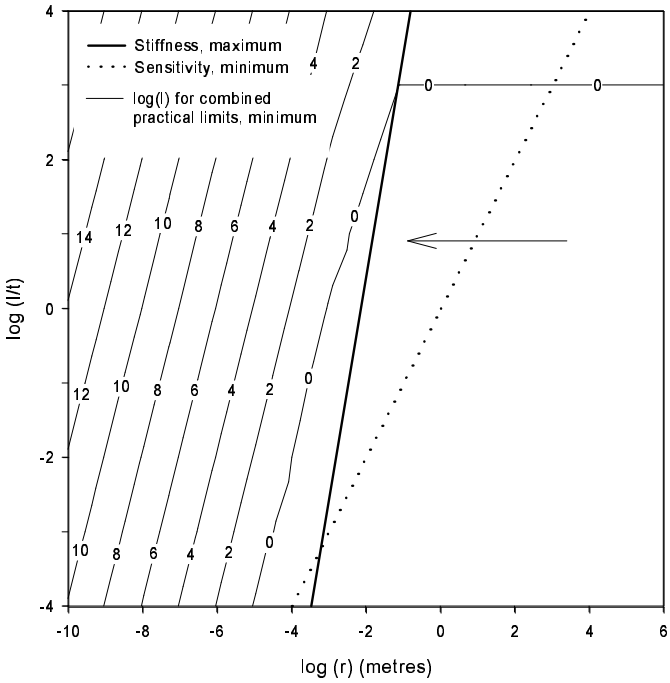

Figure B.11: Graphical representation of criteria for n=max design, dimensions in log metres. Contours of $\log(l)$. Arrow indicates allowable design in the area between the stiffness and sensitivity limits.

Any value of $\log(r)$ between the stiffness and sensitivity lines, above the minimum radius is allowed. The foregoing discussion assumes that cost can be disregarded. However, this is an engineering dissertation, so that real materials also have real cost. It is inevitable that cost be considered.

Cost considerations of n=max design

The cost implication of Equation B.40 can now be considered. Equation B.40 limits the radius and length to multiples of n and the gauge dimensions. As a result, a limited set of r and l can be considered, and then a solution for t in all the other limiting equations may be found, checking if the criteria are allowed. For example, if n=1 is considered, the length must be that of one strain gauge and the circumference is the width of four gauges (and simple geometry will give the radius). The n=1 design may not be valid for one of the other design criteria. A minimum or maximum t can be found for each equation. Then the overall minimum or maximum t can be determined and written in the Table B.2. If the minimum t, is less than the maximum t then the design is allowable. The values of n,r,l,t are shown in Table

B.2.The most economical solution where all the criteria are fulfilled is $n = 8$ where: $r = 9.84$mm, $l = 11.4$mm and $t = 4.51$mm.

Table B.2: Table of r,l,t_{min}, t_{max} for n=1...10 for n=max design.

n	r(m)	l(m)	t min (m)	t max (m)	allowable design
1	1.23E-03	1.14E-02	2.17E+00	75.64E-04	no
2	1.23E-03	2.28E-02	4.35E+00	5.64E-04	no
2	2.46E-03	1.14E-02	2.72E-01	1.13E-03	no
3	1.23E-03	3.41E-02	6.52E+00	5.64E-04	no
3	3.69E-03	1.14E-02	8.06E-02	1.69E-03	no
4	1.23E-03	4.55E-02	8.70E+00	5.64E-04	no
4	2.46E-03	2.28E-02	5.44E-01	1.13E-03	no
4	4.92E-03	1.14E-02	3.40E-02	2.26E-03	no
5	1.23E-03	5.69E-02	1.09E+01	5.64E-04	no
5	6.15E-03	1.14E-02	1.74E-02	2.82E-03	no
6	1.23E-03	6.83E-02	1.30E+01	5.64E-04	no
6	2.46E-03	3.41E-02	8.16E-01	1.13E-03	no
6	3.69E-03	2.28E-02	1.61E-01	1.69E-03	no
6	7.38E-03	1.14E-02	1.01E-02	3.39E-03	no
7	1.23E-03	7.97E-02	1.52E+01	5.64E-04	no
7	8.61E-03	1.14E-02	6.34E-03	3.95E-03	no
8	1.23E-03	9.11E-02	1.74E+01	5.64E-04	no
8	2.46E-03	4.55E-02	1.09E+00	1.13E-03	no
8	4.92E-03	2.28E-02	6.80E-02	2.26E-03	no
8	9.84E-03	1.14E-02	4.25E-03	4.51E-03	yes
9	1.23E-03	1.02E-01	1.96E+01	5.64E-04	no
9	3.69E-03	3.41E-02	2.42E-01	1.69E-03	no
9	1.11E-02	1.14E-02	3.33E-03	5.08E-03	yes

It should be noted that where the design exceeded the thin-walled short tube buckling criterion, it was found that the long tube buckling limit was a less stringent limit, and thus has no effect on the solution.

At the time, it seemed reasonable to consider only designs in which the torque bar is completely covered with gauges and to simplify the optimization problem by prescribing that n sets of four gauges will be used and seeking a optimum design of

a torque bar completely covered by 4n strain gauges. It appears that this approach is not acceptable, since for any small integer value of n the condition that the bar be covered by gauges is an unreasonable constraint. For example, if n=1 then the length or the radius must be small. A higher combination of stiffness and sensitivity can be attained by applying more than one set of four gauges to a larger bar (a design considering the conditions between n=1 and n=free). This method (covering the bar with gauges) of analysis was abandoned. The sensitivity was probably the one most important factor in the ideal design of the n=max torque tube (Section B.3.4). This in turn was affected by the power dissipation.

The mechanical design for n=max will certainly be different from that of n=1. The starting assumption with this design was that sensitivity can be increased by taking the same mechanical design and covering it completely with strain gauges. It seemed reasonable to consider only designs in which the torque bar is completely covered with gauges and to simplify the optimization problem by prescribing that n sets of four gauges will be used, and seeking a optimum design of a torque bar completely covered by 4n strain gauges. It appears that this approach is not acceptable. It was not possible to select a low cost n=max design, since the requirement that the gauges must fill the surfaces leads a minimum of 8 sets of gauges on the tube. This design was more of academic interest (useful for greatest possible sensitivity) but of no practical use, thus resulting in the choice of the n=1 design.

Experimentalists who use strain gauges, never use them in series [87, 90, 88]. Series of strain gauges would also lead to a greater risk of errors in the strain gauging, such as poor jointing, more leads increases the risk of interference from poorly shielded leads [71] (and more, as listed Section B.3.3).

The packed design (n=max) and the single gauge design (n=1) are the two extreme choices in how to deal with sensitivity (Equation B.21 for n=max and Equation 4.36 for n=1).

Appendix C

Torsional stress and strain calibrations

C.1 Strain calibration

The calibration of the accelerometer was done by using a bubble type reference inclinometer from CSIR. The X,Y abscissae are exchanged for convenience. Due to the high precision of the accelerometer (Appendix B.2.2, page 149), vibrational interference is expected. The signal from the accelerometer is known [81] to be well approximated by a third order polynomial. Thus, the strain calibration will be a combination of systematic and statistical error.

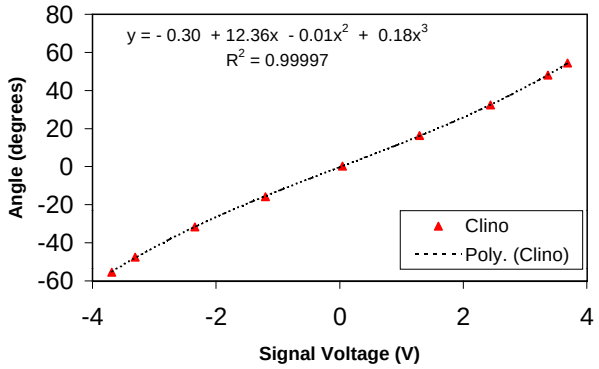

Figure C.1: First accelerometer calibration. Inclinometer angle versus voltage on accelerometer. 'Poly (Clino)' is the 4th order polynomial regression fit of the 'Clino' points. X,Y abscissae are exchanged for convenience.

C.2 Torque tube calibration

It was found that the calibration was not reproducible above a certain weight, due to the calibration bar plastically deforming at high torque (greater than 100Nm). It was anticipated that higher loads would not be seen in the system since they were brought into the design to give a mechanical safety factor. Thus, it was decided to only calibrate to 100 Nm. Additionally, a measuring equipment malfunction required a third calibration (shown in Figure 5.3). This calibration was used in all the tests.

C.3 Calibration errors

The uncertainty in the strain in the elastic region is (using Equation 4.14)

$$\begin{aligned} \gamma &= \frac{\phi R_{outer}}{L} \\ &= 0.014\%. \end{aligned} \tag{C.1}$$

Thus, the uncertainty of the strain measuring system (accelerometer) was more influenced by the calibration (0.05° at best) than the uncertainty associated with the actual measurement of the voltage (0.017°) (Figure C.2).

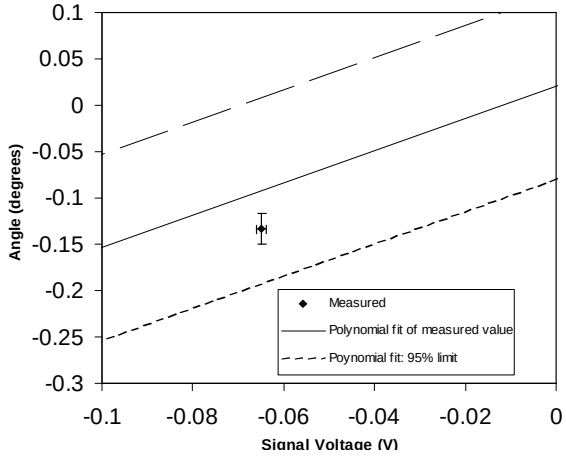

Figure C.2: Enlarged view of Inclinometer calibration number 2.

Similarly, the uncertainty of the torque measuring system was more influenced by the calibration than the uncertainty associated with the actual measurement of the voltage (Figure C.3).

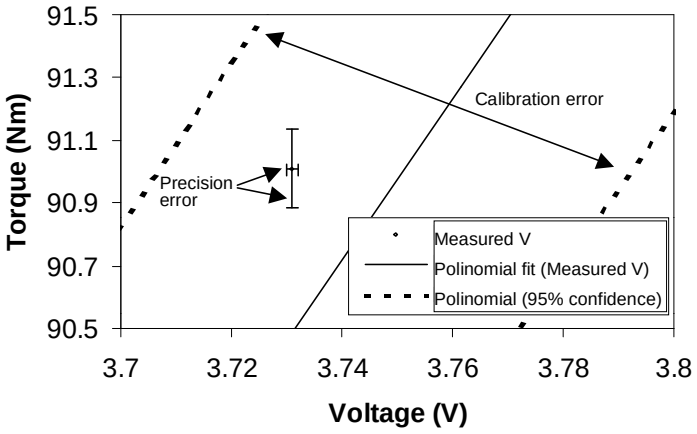

Figure C.3: Enlarged view of torque calibration number 3.

C.4 Generic uncertainty analysis

Generally when there is a function

$$F = F(x, y, z), \tag{C.2}$$

the uncertainty in F, denoted ΔF, is

$$\Delta F = \sqrt{\left(\frac{\partial F}{\partial x}\Delta x\right)^2 + \left(\frac{\partial F}{\partial y}\Delta y\right)^2 + \left(\frac{\partial F}{\partial z}\Delta z\right)^2}, \tag{C.3}$$

where Δx, Δy, Δz are uncertainties in the independent variables x, y, z respectively [82, page 42]. Both the variables and the uncertainties in each variable must independent of one another.

Appendix D

Analysis of the torsion test results

D.1 Method for determining elastic slope and 'yield'

The deviation from linearity was found by observing the residual error (the difference between the predicted and actual values) in a straight line fit for the first part of the curve (the elastic region and the yield) as in Figure D.1. The yield point was approximated by estimating the deviation of the residual, while the actual value was calculated by calculating the intersection of linear fit of the elastic part and the linear fit of 200 data points above it (equivalent to about 0.05 shear strain), as illustrated in Figure D.2.

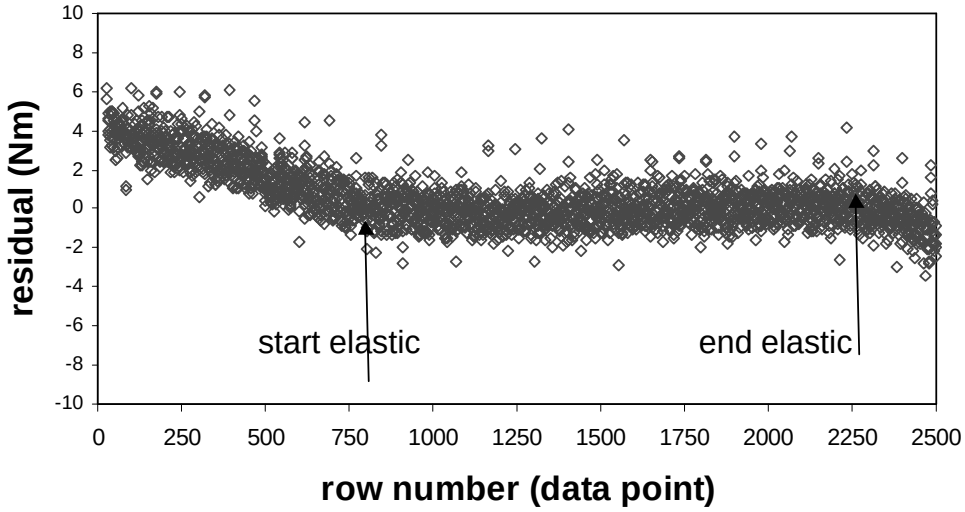

Figure D.1: Determination of elastic region from the straight line residual plot of the torsional shear-strain graph.

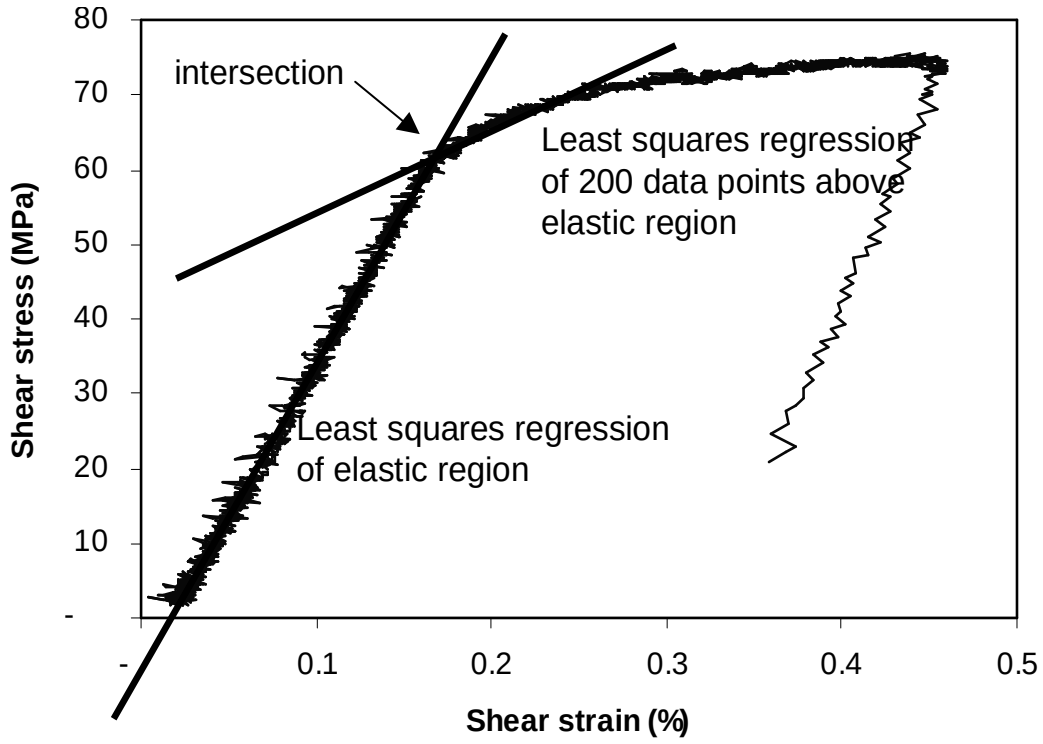

Figure D.2: Illustration of yield calculation from stress-strain curve for comparative purposes.

D.2 Uncertainty in yield

The uncertainty in the yield will be calculated from the uncertainty in the torque calibration.

Differentiating Equation 5.2, according to Equation C.3 in Appendix C.4, page 171[82], results in the following:

$$\Delta T = \sqrt{(\cos\theta_{cal} Mg\Delta L_{cal})^2 + (-L_{cal}\sin\theta_{cal} Mg\Delta\theta_{cal})^2 + (L_{cal}\cos\theta_{cal} g\Delta M)^2} \quad \text{(D.1)}$$

The uncertainties in L_{cal}, θ_{cal}, M are established to be 0.001m, 0.0003rad, 0.001kg respectively. The maximum uncertainty is 0.13Nm which far less than the uncertainty related to the curve fit. The uncertainty for the calibration curve fit is calculated in the same manner as the strain (5.1) and is 1.14Nm. This results in the uncertainty in T, $\Delta T = 1.14$Nm.

In the calibration, the errors in the linear regression and the precision in the measurement are calculated. According to Coleman and Steele [82, p173], twice the standard error of estimate may be used as the uncertainty, and from an enlarged part of the calibration graph in Figure C.3, this uncertainty in the linear regression is much larger than the resolution of the measurement system.

In the case of the calibration, very so few points were used so the uncertainty associated with the linear fit is much larger than the uncertainty in the measurement [82, p173].

In calculating the effect of sample dimensions on yield, both the groove and the I_p will have an effect.

The groove (which introduces a stress concentration) would affect the yield as follows:

$$\tau = K_{ts}\frac{Tr}{I_p}. \quad \text{(D.2)}$$

The largest I_p can be found by solving

$$\frac{dI_p}{dx} = 0, \quad \text{(D.3)}$$

where

$$\frac{dI_p}{dx} = -4R_{inner}^2(mx + c), \quad \text{(D.4)}$$

subject to the limit ($0mm < x < 50mm$). Note that I_p is smallest when inner and outer radii are concentric (as defined previously) I_p is about the centre of the outer radius).

D.3 Uncertainty in modulus

The uncertainty in shear modulus is calculated from both the uncertainty of the linear fit of the slope (twice the standard error of estimate) and the resolution of the measurement of the variables (sample length, radius).

D.3.1 Sample dimension variations

Variations in the sample must be accounted for. Using parallel axis theorem [68] for calculating the polar moment of inertia, I_p, (about the centre the outer radius), the following formula is obtained:

$$I_p = \frac{\pi}{2}\left(R_{outer}^4 - R_{inner}^4 - 2R_{inner}^2 x^2\right), \tag{D.5}$$

where R_{outer} and R_{inner} are the inner and outer radius and x is the distance of the centre of the inside diameter from the centre of the outer diameter, as illustrated in Figure D.3.

If the sample bore varies with length as indicated in Figure D.4, the equation which describes the deviation of the centre of the inner diameter with respect to the centre of the outer diameter would be the equation for a straight line y=mx+c. At any cross section, the polar moment of inertia is:

$$\begin{aligned} I_p &= \frac{\pi}{2}(R_{outer}^4 - R_{inner}^4 - 2R_{inner}^2 y^2) \\ &= \frac{\pi}{2}(R_{outer}^4 - R_{inner}^4 - 2R_{inner}^2 (mx+c)^2). \end{aligned} \tag{D.6}$$

The shear modulus of all the samples may be calculated from:

$$\phi = \int_0^L \frac{T\ dx}{GI_{px}}, \tag{D.7}$$

$\frac{T}{\phi}$, (the slope) is independent of the sample length and the I_p can be taken from

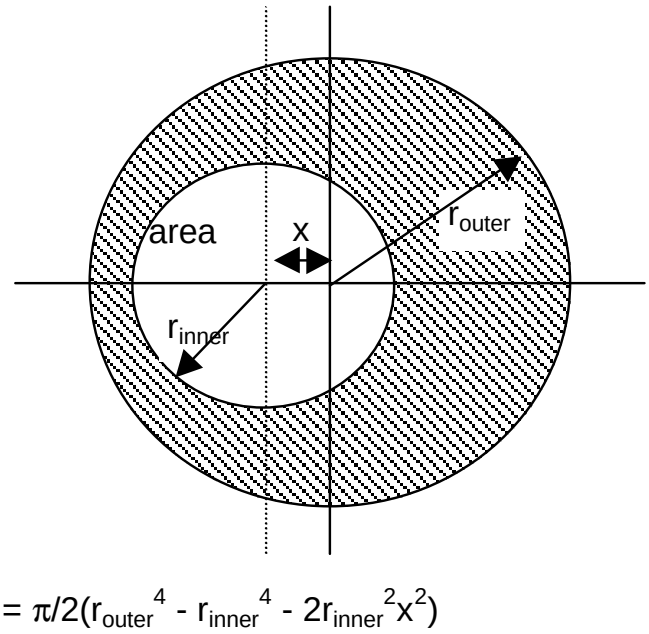

Figure D.3: Parallel axis theory.

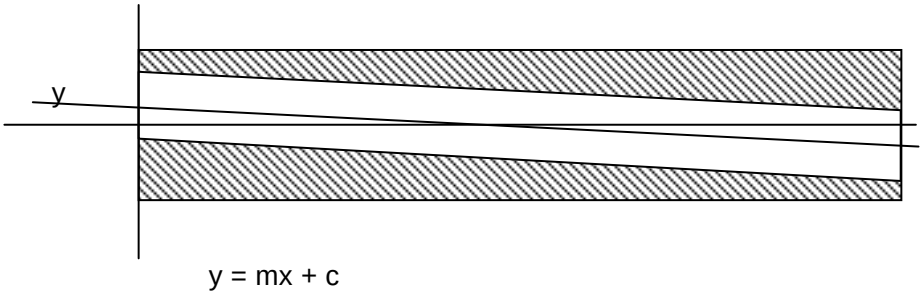

Figure D.4: Illustration of non-concentric, nonparallel bore of the sample (exaggerated).

Equation D.6 so that:

$$G = \frac{T}{\phi}\int_0^L \frac{2dx}{\pi(R_{outer}^4 - R_{inner}^4 - 2R_{inner}^2(mx+c)^2)}. \quad \text{(D.8)}$$

Integrating this equation using MATLAB,

$$\begin{aligned} G &= \frac{T\sqrt{2}}{\pi\phi m R_{inner}(R_{outer}^4 - R_{inner}^4)^{\frac{1}{2}}}\left[atanh\left(\frac{\sqrt{2}R_{inner}(mx+c)}{(R_{outer}^4 - R_{inner}^4)^{\frac{1}{2}}}\right)\right]_{x=0}^{x=L} \\ &= \frac{T}{\phi}\frac{\sqrt{2}\left[atanh\left(\frac{\sqrt{2}R_{inner}(mL+c)}{(R_{outer}^4 - R_{inner}^4)^{\frac{1}{2}}}\right) - atanh\left(\frac{\sqrt{2}R_{inner}(c)}{(R_{outer}^4 - R_{inner}^4)^{\frac{1}{2}}}\right)\right]}{\pi m R_{inner}(R_{outer}^4 - R_{inner}^4)^{\frac{1}{2}}}. \quad \text{(D.9)} \end{aligned}$$

Figure D.5 is an example of a concentricity function for sample AN1.

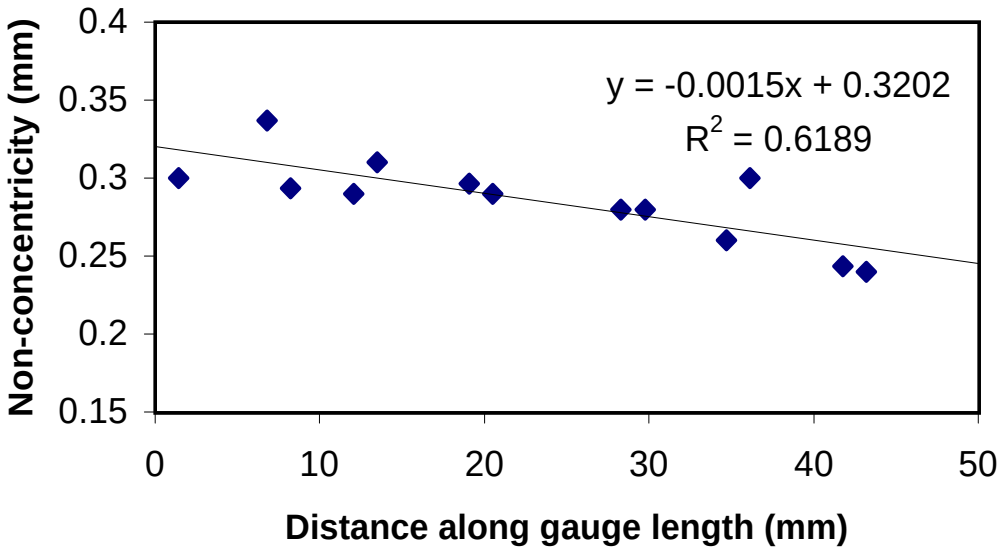

Figure D.5: Concentricity functions for sample AN1.

All the concentricity results are summarized in Table D.1.

In calculating the uncertainty of the modulus, Equation C.3 is applied to Equation D.9:

$$\begin{aligned} U_G^2 &= \left(\frac{dG}{d\frac{T}{\phi}}U_{\frac{T}{\phi}}\right)^2 + \left(\frac{dG}{dR_{inner}}U_{R_{inner}}\right)^2 + \left(\frac{dG}{dR_{outer}}U_{R_{outer}}\right)^2 + \\ &\left(\frac{dG}{dm}U_m\right)^2 + \left(\frac{dG}{dc}U_c\right)^2 + \left(\frac{dG}{dL}U_L\right)^2, \quad \text{(D.10)} \end{aligned}$$

Table D.1: A summary the concentricity functions of the samples.

Sample	m	c (mm)
AN1	-0.0016 ± 0.043	0.32 ± 0.020
C32	0.0013 ± 0.034	0.25 ± 0.020
A61	-0.0019 ± 0.070	0.26 ± 0.020
A41 (aged)	0.0021 ± 0.037	0.24 ± 0.020
A21 (aged)	-0.0014 ± 0.048	0.28 ± 0.020
C72 (aged)	-0.0019 ± 0.043	0.23 ± 0.020

where U_{var} is the uncertainty in each variable '*var*'. This was again calculated using MATLAB. The uncertainty can be determined by a set of time-consuming functions, simply:

$$\frac{dG}{d\frac{T}{\phi}} = \frac{2\text{atanh}\left(\frac{K2(Lm+c)}{(K2K1)^{\frac{1}{2}}}\right) - 2\text{atanh}\left(\frac{K2c}{(K2K1)^{\frac{1}{2}}}\right)}{\pi m(K2K1)^{\frac{1}{2}}}, \tag{D.11}$$

where

$$K1 = R_{outer}^4 - R_{inner}^4 \tag{D.12}$$

and

$$K2 = 2R_{inner}^2. \tag{D.13}$$

$$\frac{dG}{dR_{inner}} = 2\left(\frac{T}{\phi}\right)\frac{\frac{4R_{inner}K1(Lm+c)-K3(Lm+c)}{K1-K2(Lm+c)^2} - \frac{4R_{inner}cK1-cK3}{K1-K2c^2}}{\pi mK2K1^3} - 2K3\left(\frac{T}{\phi}\right)\frac{\left(\text{atanh}\left(\frac{K2(Lm+c)}{(K2K1)^{\frac{1}{2}}}\right) - \text{atanh}\left(\frac{K2c}{(K2K1)^{\frac{1}{2}}}\right)\right)}{\pi m(K2K1)^{\frac{3}{2}}}, \tag{D.14}$$

where

$$K3 = 2R_{inner}K1 - 4R_{inner}^5. \tag{D.15}$$

$$\frac{dG}{dR_{outer}} = 2\left(\frac{T}{\phi}\right)\frac{\left(-8R_{inner}^4(Lm+c)\frac{R_{outer}^3}{(K1-K2(Lm+c)^2)} + 8R_{inner}^4c\frac{R_{outer}^3}{(K1-K2c^2)}\right)}{\pi mK2^2K1^3} - 4\left(\frac{T}{\phi}\right)\frac{\text{atanh}\left(K2\frac{(Lm+c)}{(K2K1)^{\frac{1}{2}}}\right) - \text{atanh}\left(\frac{K2c}{(K2K1)^{\frac{1}{2}}}\right)}{\pi mK1^{\frac{3}{2}}K2^{\frac{5}{2}}R_{outer}^3}, \tag{D.16}$$

$$\frac{dG}{dm} = 2\left(\frac{T}{\phi}\right)\frac{L}{K1^2(1-K2(Lm+c)^2)\pi m} - 2\left(\frac{T}{\phi}\right)\frac{\operatorname{atanh}\left(\frac{K2(Lm+c)}{(K2K1)^{\frac{1}{2}}}\right)+\operatorname{atanh}\left(\frac{K2c}{(K2K1)^{\frac{1}{2}}}\right)}{\pi m^2(K2K1)^{\frac{1}{2}}}, \tag{D.17}$$

$$\frac{dG}{dc} = 2\left(\frac{T}{\phi}\right)\frac{\left(\frac{K2}{K1-K2(Lm+c)^2}-\frac{K2c^2}{c^2K1-K2}\right)}{\pi mK2} \tag{D.18}$$

and

$$\frac{dG}{dL} = \frac{2\left(\frac{T}{\phi}\right)}{(1-K2(Lm+c)^2)\pi}. \tag{D.19}$$

These are used in the calculation of the 95% uncertainties in Figure 6.5.

D.4 Analysis of modulus

Due to the low and variable results, there was a suspicion that the samples were poorly machined, and when they were sectioned, it was found that the inner bore of the samples was not concentric with the outer diameter.

The identification of outliers in tests was done by using Chauvenet's Criterion [82]. When

$$\zeta S_x \leq |X_k - \overline{X}|, \tag{D.20}$$

where S_x is the sample standard deviation, X_k is the outlier in the sample, $\overline{X}$ is the sample average and for number of samples, $n < 833333$,

$$\zeta = \sum_{i=0}^{5} A_i \left[ln(n)\right]^i \tag{D.21}$$

where $A_0 = 0.720185$, $A_1 = 0.674947$, $A_2 = -0.0771831$, $A_3 = 0.00733435$, $A_4 = -0.00040635$, and $A_5 = 0.00000916028$ then X_k meets the criterion and is considered an outlier. For the current sample set, C32 must be tested for rejection/acceptance.

Using the LHS of Equation D.20, where $\zeta = 1.73$,

$$\begin{aligned} \zeta S_x &= 1.73 \times 3.37, \\ \zeta S_x &= 5.83 \end{aligned} \tag{D.22}$$

and the RHS of Equation D.20,

$$\begin{aligned} |X_k - \overline{X}| &= |47.6 - 40.9|, \\ |X_k - \overline{X}| &= 6.7. \end{aligned} \tag{D.23}$$

Thus, since $5.83 \leq 6.7$, X_k meets the criterion and sample C32 shear modulus is considered an outlier.

D.5 Analysis of yield

The identification of outliers in tests was done by using Chauvenet's Criterion [82]. The most likely outlier is sample A61. As before, using the LHS of Equation D.20, where $\zeta = 1.73$,

$$\begin{aligned} \zeta S_x &= 1.73 \times 6.35, \\ \zeta S_x &= 11.0 \end{aligned} \tag{D.24}$$

and the RHS of Equation D.20,

$$\begin{aligned} |X_k - \overline{X}| &= |63.5 - 53.6|, \\ |X_k - \overline{X}| &= 9.9. \end{aligned} \tag{D.25}$$

Thus, since $11.0 > 9.9$, X_k does not meet the criterion and sample A61 cannot be considered an outlier.

D.6 Method for determining machine stiffness

Due to the fact only a single accelerometer could be obtained, the measured twist angle included the twist in the Avery torque measurement system. The the machine stiffness, $Stiffness_{machine}$ can be calculated from the twist,

$$\phi_{measured} = \phi_{sample} + \phi_{machine}, \tag{D.26}$$

where $\phi_{measured}$ is the measured twist, ϕ_{sample} is the sample twist and $\phi_{machine}$ is the machine twist, and since:

$$\frac{\phi_{measured}}{T} = \frac{L}{GI_p}$$

$$= \frac{1}{Stiffness}, \tag{D.27}$$

it can be said

$$\phi_{measured}/T = \frac{L}{G_{expected}I_p} + \frac{1}{Stiffness_{machine}}, \tag{D.28}$$

where $G_{expected}$ is the expected shear modulus of steel so that

$$Stiffness_{machine} = \frac{L}{I_p}\left(\frac{1}{G_{expected}} - \frac{1}{G_{measured}}\right). \tag{D.29}$$

Using the average measured modulus, $G_{measured} = 40.9$GPa, the sample dimensions and an expected modulus of 77.5GPa the machine stiffness is found to be 7610Nm/rad while the sample stiffness is 6820Nm/rad. Additionally using Equation 4.34 in terms of strain and torsional yield, the actual slope of the yield drop (Pa/strain from dT/phi) in the current setup may be obtained $42 \times 10^9 Pa$. The result is as follows:

$$\begin{aligned}
\frac{d\tau}{d\gamma} &= \frac{dT}{d\phi}\left(\frac{L}{2\pi r_o^4 t}\right) \\
&= \frac{1}{\frac{1}{K_{machine}} + \frac{l}{GI_p}}\left(\frac{l}{2\pi r_o^4 t}\right) \\
&= 42 \times 10^9 Pa.
\end{aligned}$$

This would result in a visible shear drop which would be easily measurable in the present system.